UNIVERSITY OF CALIFORNIA, SAN DIEGO

Correlated super-resolution fluorescence and electron microscopy identifies the nano-distribution of cardiac calcium channels

A Dissertation submitted in partial satisfaction of the requirements
for the degree Doctor of Philosophy

in

Bioengineering

by

Tapaswini Das

Committee in charge:

Professor Mark H. Ellisman, Chair
Professor Andrew D. McCulloch, Co-Chair
Professor Rommie Amaro
Professor Masahiko Hoshijima
Professor Geert Schmid-Schönbein

2015

The Dissertation of Tapaswini Das is approved, and it is acceptable in quality and form for publication on microfilm and electronically:

Co-Chair

Chair

University of California, San Diego

2015

DEDICATION

To my family,

Thank you for the love, support and guidance.

EPIGRAPH

Not all those who wander are lost.

– J. R.R. Tolkien

TABLE OF CONTENTS

LIST OF ABBREVIATIONS

2D	Two-dimensional
3D	Three-dimensional
Ab	Antibody
Alexa 647	Alexa Fluor 647
AMCM	Adult Mouse Cardiomyocyte
AT	Array Tomography
BSE	Back-scattered electron
Ca	Calcium
Ca	Calcium
CaM	Calmodulin
CAMKII	Calmodulin dependent Protein Kinase II
CAT	Computed Axial Tomography
Cav	Caveolin
Caveolin	Cav
CICR	Calcium Induced Calcium Release
CLEM	Correlated Light and Electron Microscopy
CRU	Calcium Release Unit
CSQ	Calsequestrin
DAB	Diaminobenzedine
DHPR	Dihydropyridine Receptor
dSTORM	Direct Stochastic Optical Reconstruction Microscopy
E-C	Excitation-Contraction
FIB-SEM	Focused Ion-Beam Scanning Electron Microscopy
FKBP	FK-506 Binding Protein
FP	Fluorescent Protein
FPALM	Fluorescence Photoactivated Localization Microscopy
FWHM	Full-width half-maximum
GFP	Green Fluorescent Protien
ITO	Indium Tin Oxide
IVEM	Intermediate high-voltage Electron Microscopy
JP	Junctophilin
jSR	Junctional Sarcoplasmic Reticulum
KO	Knockout
LTCC	L-Type Calcium Channels
MAKAP	Muscle A-Kinase Anchoring Protein
Mg	Magnesium
miniSOG	Mini Singlet Oxygen Generator
Na	Sodium
NaK	Sodium-Potassium Adenosine Triphosphatase
NCX	Sodium Calcium Exchanger
NRVM	Neonatal Rat Ventricular Myocyte
nSR	Network Sarcoplasmic Reticulum
PA-FP	Photoactivatable Fluorescent Protein
PALM	Photoactivated Localization Microscopy
PBS	Phosphate Buffered Saline
PC-FP	Photoconvertable Fluorescent Protein
PKA	Protein Kinase A

PMCA	Plasma Membrane Calcium Adenosine Triphosphatase
Po	Probability of opening
PSF	Point Spread Function
RESOLFT	Reversible Saturable Optically Linear Fluorescence Transitions
ROI	Region of Interest
RyR	Ryanodine Receptor
SBEM	Serial Block-face scanning Electron Microscopy
SEM	Scanning Electron Microscopy
SERCA	Sarco-Endoplasmic Reticulum Calcium-dependent ATPase
SIM	Structured Illumination Microscopy
SIRT	Serial Iterative Reconstruction Techniques
SR	Sarcoplasmic reticulum
SSIM	Saturated Structured Illumination Microscopy
ssTEM	Serial Section Transmission Electron Microscopy
STED	Stimulated emission depletion
STORM	Stochastic Optical Reconstruction Microscopy
T-system	Tubule system
T-tubule	Transverse tubule
tdEos	Tandem Dimer Eos
TEM	Transmission Electron Microscopy
TIRF	Total Internal Reflection Fluorescence
UV	Ultraviolet
Vs.	Versus
w/	With
WGA	Wheat Germ Agglutinin

LIST OF FIGURES

LIST OF TABLES

ACKNOWLEDGEMENTS

First and foremost, I would like to thank Dr. Masahiko Hoshijima for taking me on as an undergraduate research assistant back in 2008 with no previous laboratory background or experience. He cultivated my passion for microscopy while taking the time to personally train me, making me the scientist I am today. He always encouraged me to be independent and supported the time spent in learning new skills and understanding every inch of the microscope. He has been an amazing mentor and his work ethic continues to be an inspiration to me.

Next, I would like to express my special appreciation and thank my advisor, Dr. Mark Ellisman, for giving me the opportunity to continue my pre-doctoral studies in his laboratory. His laboratory equipped me with the tools and technical support necessary for me to see my project to completion.

Next, I would like to thank my committee members, Dr, Andrew McCulloch, Dr. Gina Sosinsky, Dr. Rommie Amaro, and Dr. Geert Schmid-Schönbein for their academic support and research guidance. A special thank you to Andrew McCulloch and Gina Sosinsky for always supporting me in my efforts to secure the American Heart Association pre-doctoral fellowship. A special thanks to Dr. Rommie Amaro as well for stepping in at the last minute to complete my committee.

Next, I would like to thank everyone at NCMIR for having my back and helping me finish my thesis. I would like to start with Tom Deerinck for always making time for my questions and helping me improve my microscopy skills. Thank you for encouraging me to celebrate monthly birthdays. It wouldn't have been possible without your donation Tom. I would like to thank Daniela Boassa

for making me part of a collaboration which ultimately became my thesis project. Her advice, both work and personal, have been invaluable to me. Next I would like to thank Eric Bushong for always looking out for me and always being available to answer my questions. I really appreciate you squeezing me in for microscopy times when I needed it. I would like to thank Hiroyuki Hakozaki for his valuable advice and the hours he spent training me on light microscopes. I would like to thank Sebastien Phan for coming in on the weekends to help me with my EM data and spending his valuable time developing software to help me with my thesis. I would like to thank Mason for his invaluable EM training and for always being available to help me when I had trouble focusing on the microscope. I would like to thank Andrea Thor for all her help in sectioning samples and always being there for me. Additionally, I would like to thank Junru Hu, Christine Kim, Ranjan Ramachandra, James Bouwer, Tristan Shone, Vicky Rowley and Edmond Negado for all their support. A big shout out to Alex, Andrew, Nate, Don, Phuong, Niko, Gabe, Cindy, Felix, Matthias, and Guilaume for making work fun.

I would like to thank my roommates Diana Quach and Joseph Sugie. Thanks for feeding me guys and making sure I am alive.

A special thanks to my family. Words cannot express how grateful I am to them for giving me the opportunity to pursue my hopes and dreams.

Lastly, I would like thank Dr. Masahiko Hoshijima, the Human Scientific Frontier Program, and the American Heart Association for supporting my graduate studies.

Chapters 1-5, in part, are a reprint of the material as it appears in Journal of Molecular and Cellular Cardiology, 2013. Das T, Hoshijima M. The dissertation author was the primary investigator and author of this paper.

Chapters 1-5, in part, are currently being prepared for submission for publication of the material. Das T, Hoshijima M. The dissertation/thesis author was the primary investigator and author of this material.

VITA

2007-2008	Deans Intern, University of California, San Diego
2007-2010	Orientation Leader, University of California, San Diego
2008-2010	Undergraduate Research Assistant, School of Medicine, University of California, San Diego
2008-2010	Undergraduate Research collaborator in UCSD Chancellor's Interdisciplinary Collaboratories program, University of California, San Diego
2010	Bachelor of Science, Department of Bioengineering, University of California, San Diego
2010-2011	Teaching Assistant, Department of Mechanical and Aerospace Engineering, University of California, San Diego
2010-2011	Teaching Assistant, Department of Physics, University of California, San Diego
2011	Master of Science, Department of Bioengineering, University of California, San Diego
2011-2012	Teaching Assistant, Department of Bioengineering, University of California, San Diego
2015	Doctor of Philosophy, Department of Bioengineering, University of California, San Diego

PUBLICATIONS

Das T, Hoshijima M. Adding a new dimension to cardiac nano-architecture using electron microscopy: Coupling membrane excitation to calcium signaling. *J Mol Cell Cardiol.* Volume 58, May 2013, Pages 5-12, ISSN 0022-2828

Shen H, Huang E, Das T, Xu H, Ellisman M, and Liu Z. TIRF microscopy with ultra-short penetration dept. Opt. Express 22, 10728-10734 (2014).

CONFERENCE ABSTRACTS

Das T, Hakozaki H, Nitu F, Bers D, Ellisman M, Cornea R, Hoshijima M. Correlative super-resolution light microscopy and electron microscopy determines spatial Ryanodine receptor type 2 distribution in mouse ventricular myocytes. FASEB J, April 2014 28:LB707

ABSTRACT OF THE DISSERTATION

Correlated super-resolution fluorescence and electron microscopy identifies the nano-distribution of cardiac calcium channels

by

Tapaswini Das

Doctor of Philosophy in Bioengineering

University of California, San Diego, 2015

Professor Mark H. Ellisman, Chair

Professor Andrew D. McCulloch, Co-Chair

The sites of cardiac excitation-contraction (E-C) coupling are composed of sarcoplasmic reticulum (SR)-localized calcium release channels, known as ryanodine receptors (RyRs), coupled to voltage-gated L-type calcium channels (LTCCs) on the sarcolemma in junctional membrane micro-domains termed “couplons”. Mounting evidence suggests that the dysregulation of calcium fluxes

within these domains is critical in the pathogenesis of heart failure. Despite their essential role in the maintenance of normal myocardial excitation and contractility, our quantitative understanding of couplons is greatly limited due to the formidable technical challenge of imaging and exploring the structure-function relationship of the E-C coupling site.

In the work presented here, I developed novel two- and three-dimensional approaches for in-resin, correlated super-resolution fluorescent light microscopy (LM) and electron microscopy (EM) to quantify the distribution of key E-C coupling molecules and reveal their association with membranous organelles in mammalian cardiomyocytes. The imaging of resin-embedded sections with stochastic optical reconstruction microscopy (STORM) was immediately followed by ultrastructural mapping using scanning or transmission EM. Three-dimensional EM data were reconstructed with both array and EM tomography. Correlated imaging using STORM and scanning EM across multiple cells revealed that while most RyRs were mapped within couplons, 21.0 ± 4.5% (n=6) of RyRs were non-junctional. LTCCs were found in couplons, and most NCXs were confined to the non-junctional subdomain of the sarcolemma. The exact localizations of junctional and non-junctional RyRs were further elucidated using correlated STORM and EM tomography, confirming that RyR signals colocalized with “feet” structures visible in couplons at the EM level. Interestingly, a significantpopulation of non-junctional RyRs was found at the inter-membrane junctions between the network SR and the outer membrane of mitochondria.

This technique was further applied to study the ultrastructural remodeling and associated RyR reorganization in genetically engineered junctophilin 2 knockout mice, a disease model which mimics abnormal E-C coupling observed

in heart failure. The approach presented in this dissertation has facilitated the expansion of our understanding of ion-channel organization in the cardiomyocyte E-C coupling pathway and will pave the way for detailed models of the molecular mechanisms that lead to reduced myocardial contractility in heart failure.

Chapter 1:

Introduction

Heart failure, a condition characterized by a decline in the ability to pump blood efficiently, represents a major public health concern and is one of the leading causes of morbidity and mortality in the United States [Go et al., 2014]. It has been attributed to multiple cellular defects such as reduced contractility, impaired calcium (Ca) signaling, and arrhythmias; however, the underlying causes of these defects are not well understood [Gomez et al., 1997; Bers , 2002; Sjaastad et al.,2003; Van oort et al., 2011]. Evidence from the literature suggests that disruption of the calcium release units (CRU) during heart failure degrades excitation-contraction (E-C) coupling, leading to the loss of contractile function [Gomez et al., 1997; Sjaastad et al., 2003]. Studies have also revealed substantial ultrastructural alterations in the sarcoplasmic reticulum (SR) and transverse tubule (T-tubule) of cardiomyocytes during times of cardiac disease, as well as in the distribution of ion channels and pumps in the CRU that are crucial to the regulation of myocardial contraction and relaxation [Wei et al., 2010; Wu et al., 2012; Louch et al., 2013; Zhang et al., 2013]. Despite their critical role in maintaining functional myocardial excitation and contractility, our quantitative understanding of CRU biology and ultrastructure remains largely limited, primarily because of the formidable technical challenge posed by exploring the structure-function relationship of the E-C coupling site.

This chapter will serve as a review of how new microscopic imaging techniques are renewing our understanding of cardiac cellular micro-domains, which control Ca signaling (Fig. 1.1). I will begin by discussing the current state of development in light microscopy (LM) and electron microscopy (EM) techniques. Next, I will touch on the history of how EM contributed to establishing the initial concept of E-C coupling, as well as the recent pioneering applications

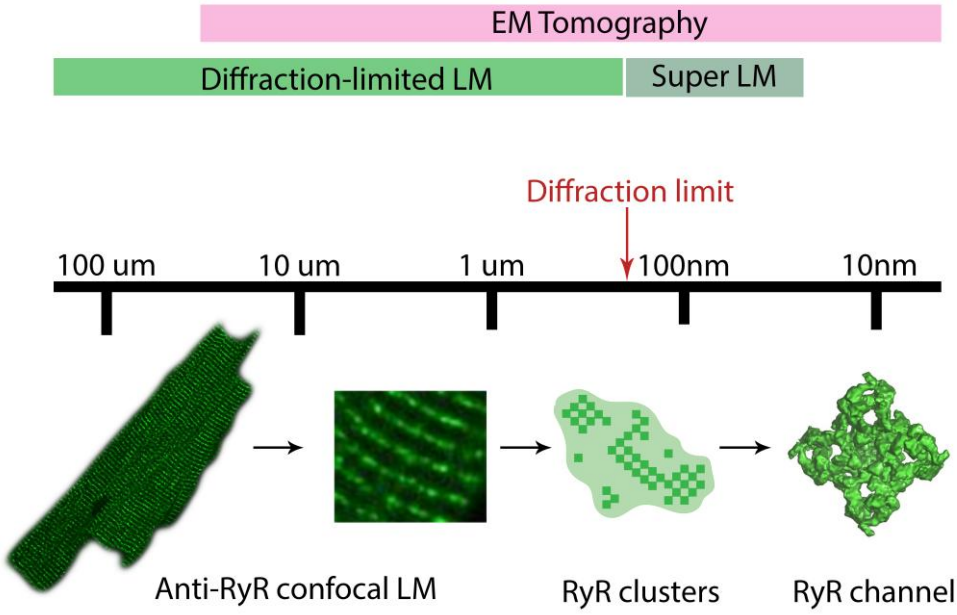

Figure 1.1. : Ryanodine receptor distribution in relation to optical resolution scales. Noble prize winning super-resolution LM (Super LM) techniques are closing the resolution gap between LM and EM. This is very useful for proteins like RyRs whose distribution spans across different scales in the ventricular myocyte. From left to right: whole ventricular myocyte, typical transverse striated pattern of RyRs in a confocal image, example of a reconstructed super-resolution LM image with fitted individual RyRs compared to the diffraction-limited image in light green, cryoEM model of RyR1 channel tetramer (cytosolic portion shown is 27x27nm). (CryoEM map of RyR1 channel (EMDB 1606) was uploaded from https://www.cgl.ucsf.edu/chimera/) [Pettersen et al., 2004].

of sub-diffraction-limited LM and EM tomography towards understanding CRU organization. The chapter will conclude with a discussion of novel correlated imaging strategies, and how they are being applied to take on the challenge of thoroughly characterizing the ultrastructure and molecular composition of the E-C coupling site.

1.1. Advances in optical microscopy

1.1.1. Diffraction-limited LM

Since the 16th century, light microscopes have been creating magnified images of biological samples, enabling scientists to directly see the fine features of these specimens. With the advent of better fabrication and manufacturing techniques, scientists evolved from using self-ground optical lenses to simple compound microscopes with colored stains to resolve cellular features in tissue samples. While perfecting the theory of transmitted light microscopy in the late 19th century, Ernst Abbe and Lord Rayleigh realized that the resolution of optical imaging instruments is fundamentally limited by the diffraction of light (Fig. 1.2) [Abbe, 1873; Rayleigh, 1896]. Diffraction prevents the resolution of two closely spaced objects if their distance apart is less than half of the full-width half-maximum (FWHM) generated by their point spread function (PSF). This resolution limit is called the Abbe limit [Abbe 1873]. Thus, even with the most advanced optics, we could at best achieve resolutions of ~200 nm in the lateral direction and ~500 nm in the axial direction using visible light. Efforts made to improve resolution by using short-wavelength ultraviolet (UV) light instead of visible light led to the establishment of fluorescence microscopy (Kohler, 1904 (ref?)]. The field was revolutionized with the development of suitable excitation

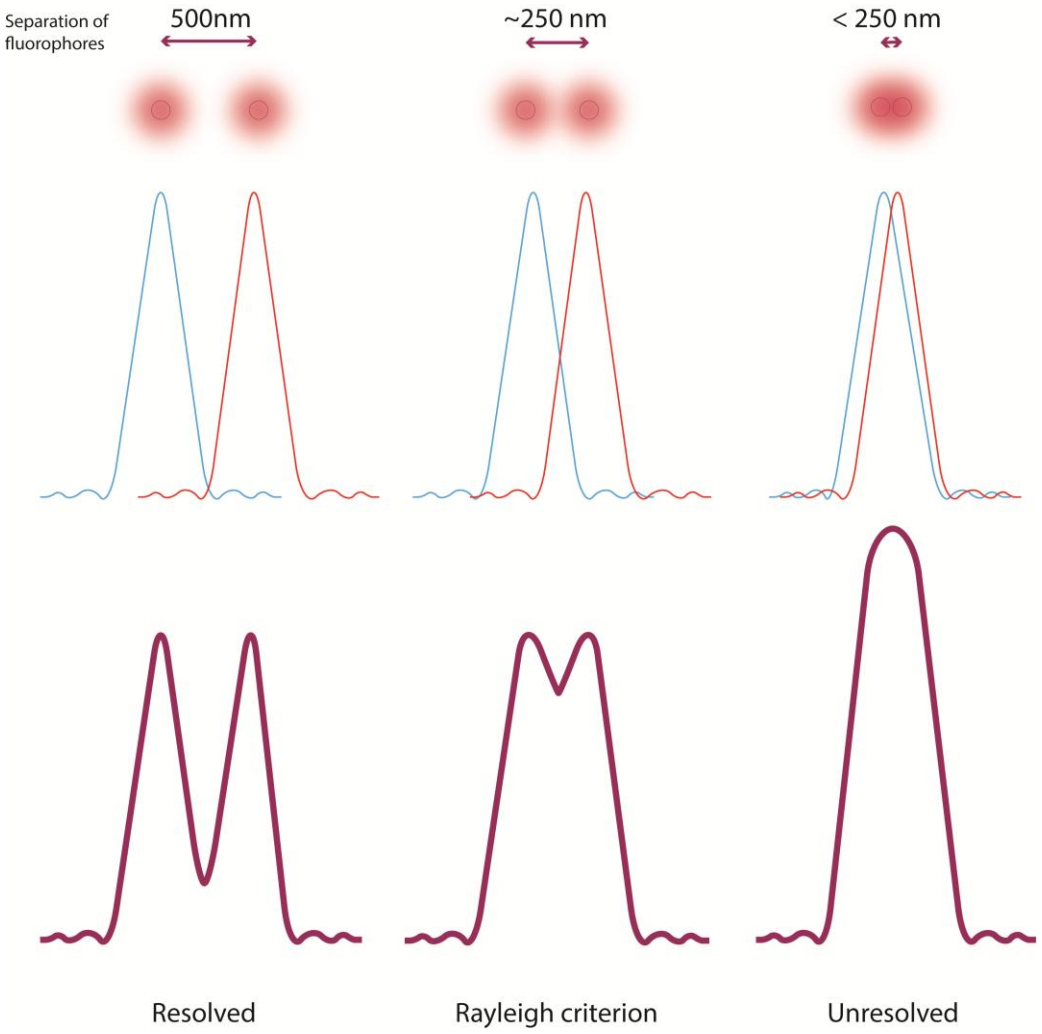

Figure 1.2. : Diffraction limit of optical resolution. Two closely spaced point-sources can be resolved by optical microscopy if they are separated by the Rayleigh criterion but will not be resolved if they are closer together than this distance.

sources and fluorescence probes, which allowed ions, proteins, signaling molecules, and structural features to be visualized. Improvements in fluorescence labeling techniques via immunolabeling and genetically encodable fluorescent proteins such as the green fluorescent protein (GFP) allowed the observation of molecular- and organelle-specific signals in fixed as well as live samples [Giepmans et al., 2006]. Although the diffraction limit doesn't affect imaging at the organ or tissue level, it does prevent scientists from successfully resolving and investigating sub-organellar features smaller than the wavelength of light. An early, but powerful, approach to circumventing this issue was to use electrons instead of photons during imaging. EM offers a roughly 400x increase in resolution, but, unlike LM, it is incompatible with live cell imaging because the samples must be imaged under vacuum conditions. This restriction drove scientists to develop methods to circumvent the Abbe limit.

1.1.2. Extended resolution in LM

For over a hundred years since the establishment of the Abbe limit, scientists worked tirelessly to defy this fundamental limit of resolution imposed upon them. Since the limit of diffraction inherently comes into play when light has traveled a distance equal to its wavelength, scientists first attempted to circumvent the diffraction limit by limiting the distance light needs to propagate by physically placing the excitation source or detection probe close to the sample [Synge, 1928]. This was called near-field scanning microscopy, and resulted in an almost two-fold improvement in lateral resolution. However, its application to live cell imaging was very limited, as it was challenging to physically place the sample within nanometers of the source/probe [Pohl et al., 1984; Lewis et al.,

1984; Betzig et al., 1986]. Thus, driven by the desire to image unstained neural networks in living brains, Marvin Minsky developed and patented the principle of confocal microscopy, which combines a focused laser with a pinhole for detection to improve spatial resolution by a factor of 1.414. Despite the revolutionary nature of this concept, it wasn't until 20 years later that there was enough technological innovation (lasers and data acquisition methods) to open the door for its widespread use [Cremer and Cremer, 1978]. Now, confocal microscopy is the gold standard for all optical bioimaging.

Following the same concept of limiting the scattering of light for improved resolution, multiphoton microscopy employs low-scattering infrared light for deep-tissue imaging [Zipfel et al., 2003]. Both confocal and multiphoton microscopy are widely popular because they reduce out-of-focus fluorescence, allowing for three-dimensional (3D) optical sectioning imaging. An alternative strategy to improve resolution focused on increasing the numerical aperture of the microscope, since the resolving power of a microscope varies inversely with its numerical aperture. Spatial resolution was improved by using two objective lenses simultaneously to increase the effective numerical aperture of the microscope. For example, 4Pi microscopy and I5M use two precisely aligned opposing objective lenses for excitation and/or detection to boost axial resolution to 100 nm [Hell and Stelzer, 1992; Gustafsson, 1999].

Meanwhile, as computer processors advanced and algorithms became available, scientists began to consider techniques of improving resolution computationally. In the 1980s, the concept of deconvolution was introduced as a post-processing step to improve wide-field imaging resolution. Deconvolution of image z-stacks increased the signal-to-noise ratio, resulting in improved

resolution [Agard and Sedat, 1983; Agard et al., 1989]. Structured illumination microscopy (SIM), introduced in the late 1990s, combined engineered optical illumination techniques with computational processing to reconstruct images with higher resolution. In SIM, the sample is illuminated using a patterned light field, creating an image that is the product of the sample and the excitation pattern [Heintzmann and Cremer, 1999; Gustafsson, 2000]. The final reconstructed image takes advantage of the spatial modulation from the excitation pattern to yield images with isotropic lateral resolutions down to 100 nm [Gustafsson, 2000].

1.1.3. Sub-diffraction-limited LM

By combining redesigned optical pathways with using specialized hardware and advanced post-processing algorithms, scientists had successfully achieved images with lateral and axial resolutions as fine as 100 nm. However, this was still insufficient to resolve molecular and protein localizations, as well as features inside organelles. Thus, the desire to achieve nanometer resolution light microscopy fueled the development of several revolutionary “sub-diffraction-limited” or “super-resolution” methods over the last two decades (Table 1.1). Eric Betzig, Stefan Hell and William E. Moerner were awarded the 2014 Nobel Prize in chemistry for their pioneering work in super-resolution fluorescence microscopy. These methods either physically or chemically modify fluorophores such that neighboring fluorophores are in alternating “on” and “off” states to overcome the resolution barrier [Hell, 2007]. There are two general approaches to super resolution microscopy, which will be discussed below.

Table 1.1. : Extended resolution and super-resolution LM methods.

	Extended resolution techniques				Super-resolution techniques			
Technique	**Confocal microscopy**	**Near field techniques**	**Wide field+ deconvolution**	**SIM**	**STED**	**SSIM**	**PALM/FPALM/ PALMIRA**	**STORM/dSTORM**
Principle	focused laser with pinhole detection	small aperture scanning/evanescent wave illumination	wide field+ deconvolution	structured illumination	PSF shrinking with saturated emission depletion	high excitation structured illumination	photoactivating molecules followed by localization	chemically induced photoswitching molecules followed by localization
Lateral resolution	180-250nm	20-300nm	180-250nm	100-130nm	20-100nm	50nm	20-50nm	20-50nm
Axial resolution	500-700nm	10-100nm	500-700nm	250-350nm	30-700nm	-	20-100nm, 10nm (iPALM)	20-30nm (3D STORM),100nm (TIRF)
Probes	all	all	all	most common dyes	special dye	special dyes	genetically encodable photoactivatable dyes	activator and reporter dyes/photoswitchable dyes
Live cell	yes	yes	yes	limited	limited	no	yes	yes
3D imaging	yes	N.A.	yes	yes	yes	N.A.	yes	yes
Multi-color imaging	3	2-3	>3	3	2	1	2	3
Advantages	reduced out of fluorescence imaging	reduced out of fluorescence imaging	post-processing removes out-of-focus light	high throughput	deep tissue imaging	isotropic lateral resolution	single particle tracking (spt PALM)	immunlabeling with Alexa 647
	3D z-stack imagng		ideal for thin samples	simple instrumentaton			genetically encodable dyes available	
							laser-dependet photoactivation	
Disadvantages	limited z resolution	restricted to region near coverslip	post-processing artifacts	reconstruction artifacts	complex instrumentation and high photobleaching	reconstruction artifacts	over/under labeling artifacts and complex data processing	over/under labeling artifacts,complex data processing and requires special imaging media

1.1.3.1. Super-resolution microscopy based on patterned-illumination

This category encompasses techniques that engineer the excitation source to manipulate the fluorescence emission of labels. A patterned field of light is used to spatially modulate fluorophore behavior such that not all fluorophores are emitting at the same time, allowing neighboring fluorophores to be distinguished from each other, leading to enhanced spatial resolution.

1.1.3.1.1. Stimulated emission depletion

Stimulated emission depletion (STED) microscopy was the first super-resolution concept proposed in the early 90s by Stefan Hell. Stimulated emission using a second laser (depletion light) suppresses the fluorescence of the fluorophore located away from the center of excitation by bringing the excited fluorophore to the ground state [Hell and Wichmann, 1994; Klar and Hell, 1999; Hell, 2007]. This process reduces the size of the excitation spot, ultimately reducing the effective width of the PSF and allowing a super-resolution image to be recorded. In practice, fluorophores are excited simultaneously by an excitation laser and a donut shaped depletion light source which is driven to saturation such that the excited state fluorophores get depleted everywhere except at the center of the ring. The size of this region is determined by the intensity of the depletion light, which ultimately defines the resolution of the microscope. Though all dyes can undergo stimulated emission, dyes that are photostable under strong depletion light with large stimulated emission cross sections such as Atto 532 and Atto 647N are preferred. Using these dyes, STED imaging has achieved resolutions down to 20 nm [Hell and Wichmann, 1994; Klar and Hell, 1999; Hell, 2007]. Wagner and colleagues successfully applied STED microscopy towards

the live cell imaging of intact T-tubules in cardiomyocytes and were able to resolve the hollow membrane structure of the T-tubule. This would not have been possible using only the earlier, diffraction-limited LM techniques [Wagner et al., 2012]. Unlike conventional LM, STED relies on two lasers for imaging, thus inherently limiting the maximum number of dyes that can be imaged simultaneously to two [Donnert et al., 2007 and Schmidt et al., 2008]. Isotropic 3D resolutions of 30 nm can be achieved by creating a z depletion pattern using two opposing objectives in isoSTED [Schmidt et al., 2008; Schmidt et al., 2009]. Recent technological advancements have replaced the traditionally-used pulsed lasers with continuous wave lasers, allowing the use of conventional fluorophores with emissions in the green range. The faster scanning rates of these continuous wave lasers facilitate time resolutions sufficient for live cell imaging [Willig et al., 2007; Moneron et al., 2010].

1.1.3.2. Reversible saturable optically linear fluorescence transitions (RESOLFT)

The general concept of using saturable optical transitions to achieve super-resolution has been termed as “RESOLFT”, an abbreviation for reversible saturable optically linear fluorescence transitions (RESOLFT) microscopy [Hofmann et al., 2005; Bretschneider et al., 2007; Hell, 2007]. Fluorescent probes that can be reversibly photoswitched are sent into an “off”, or dark, state to shrink the area of excitation in the focal spot. In contrast to STED microscopy, photoswitching requires much lower intensity depletion light, resulting in reduced photobleaching and photo-damage to samples. The RESOLFT principle has been successfully applied to SIM, also known as Saturated SIM (SSIM), creating

sharp dark regions of zero intensity resulting in lateral resolutions of 50 nm. Similar to STED, imaging with two or more colors is a challenge, and only highly stable, specialized dyes are compatible with this mode of imaging. Live cell SSIM and 3D SSIM have yet to be implemented.

1.1.3.3. Super-resolution microscopy based on single molecule localization

This category includes techniques that depend on the stochastic activation of molecules for single-molecule imaging. Molecules within a diffraction-limited region are photochemically turned on at different times such that they can be individually imaged and localized to generate images with sub-diffraction limit resolution [Rust et al., 2006; Betzig et al., 2006; Hess et al., 2006]. In layman's terms, instead of activating all the fluorophores in the field of view at once (which results in a diffraction limited image), each fluorophore is turned on one at a time, their PSF recorded, and then deactivated, resulting in a stack of images of individual PSFs collected over time. The PSF recorded in each image is then fitted to determine the centroid of the emission and plotted onto a single localization map. This concept was developed and implemented independently by three separate groups in 2006 as stochastic optical reconstruction microscopy (STORM) [Rust et al., 2006], photoactivated localization microscopy (PALM) [Betzig et al., 2006], and fluorescence photoactivated localization microscopy (FPALM) [Hess et al., 2006].

1.1.3.3.1. PALM/FPALM

This method is based on the serial photoactivation/photoconversion and subsequent bleaching of numerous sparse subsets of photoactivatable or

photoconvertible fluorescent proteins (PA-FPs or PC-FPs) attached to the target of interest [Hess et al., 2006]. Genetically encoded PA-FPs, such as PA-GFP and PA-CFP2, can activate from a dark state to a bright fluorescent state, whereas PC-FPs, such as tandem dimer Eos (tdEos) and Dendra, can be optically transformed from one fluorescent emission bandwidth to another. A sparse subset of FPs are first activated/converted with a brief UV laser pulse and then imaged at the detection wavelength until the activated molecules bleach out. Then, then a second subset is activated and imaged, and this cycle is repeated until all the molecules are imaged. The activation is controlled such that only random sparse fields of dyes are visible in each frame. Each dye in each frame is fitted to a Gaussian PSF using a nonlinear least squares algorithm, and the center coordinates are determined and then rendered as a probability density map where brightness is proportional to the localization likelihood. Whereas PALM imaging is performed in total internal reflection fluorescence (TIRF) mode for better contrast, FPALM uses conventional wide-field illumination during imaging. Additionally, PALM has successfully been applied towards 3D, multi-color and live cell imaging [Bates et al. 2007; Shroff et al. 2007;Shroff et al., 2008;Manley et al.2008, Juette et al.,2008].

1.1.3.3.2. STORM and direct STORM (dSTORM)

STORM and dSTORM exploit the same pointillism principle as PALM/FPALM, except that STORM requires photo-switchable dye pairs and dSTORM requires single photoswitchable dye in a special imaging buffer. One such example of a photoswitchable dye pair for STORM is the cyanine switch composed of Cy3-Cy5 dyes [Rust et al., 2006]. In this case, all fluorophores are

switched off into a stable dark state using a red laser pulse. Sparse subsets of Cy5 molecules are converted back into their active fluorescent state with a green laser. The recovery rate of Cy5 depends on the proximity of the Cy3, which acts as a switch ensuring only an optically resolvable set of fluorophores are active. Lastly, the active fluorophores fluoresce under red illumination and are imaged until they switch off, and the cycle is repeated until all the molecules have been imaged. The final image is a composite of the fluorophore positions determined via Gaussian fitting of PSFs from multiple imaging cycles.

On the other hand, dSTORM can be performed with most conventional fluorophores (Alexa and ATTO dyes) as they can be programmed into "photoswitches" in the presence of reducing agents [Van de linde et al., 2011] (Fig. 1.3) . Upon illumination, a fluorophore is typically excited from its ground state to an excited state. In this state, the fluorophore has two options: it can either return to its ground state, resulting in fluorescence, or it can undergo inter-system crossing into a long-lived triplet state. In a reducing buffer, a fluorophore in its triplet state can react with the reducing agent, typically thiols, to form a radical ion. This radical state represents the non-fluorescent "off" state of the fluorophore. Upon reaction with either molecular oxygen or UV light, the fluorophore returns to the ground state, thereby recovering its fluorescent "on" state. Thus, the protein of interest is labeled with a photoswitchable dye, and the sample is immersed in a reducing buffer during dSTORM imaging. Then all the dyes are first converted into a non-fluorescent "off" state until a low spot density is reached. Images are acquired as the fluorophores fluoresce back from their radical form to their ground state under suitable excitation intensity (observed as

Figure 1.3. : dSTORM demo. The protein of interest is labeled with photoswitchable fluorophores (Step 1). Then, imaged in a thiol-based imaging buffer. Imaging begins with transferring all the fluorophores into their “off” state. This is followed by repeated stochastic activation and localization of a sparse sub-set of molecules till all the fluorophores have been imaged (Steps 2 and 3). Lastly, the localizations are reconstructed into a super-resolution images.

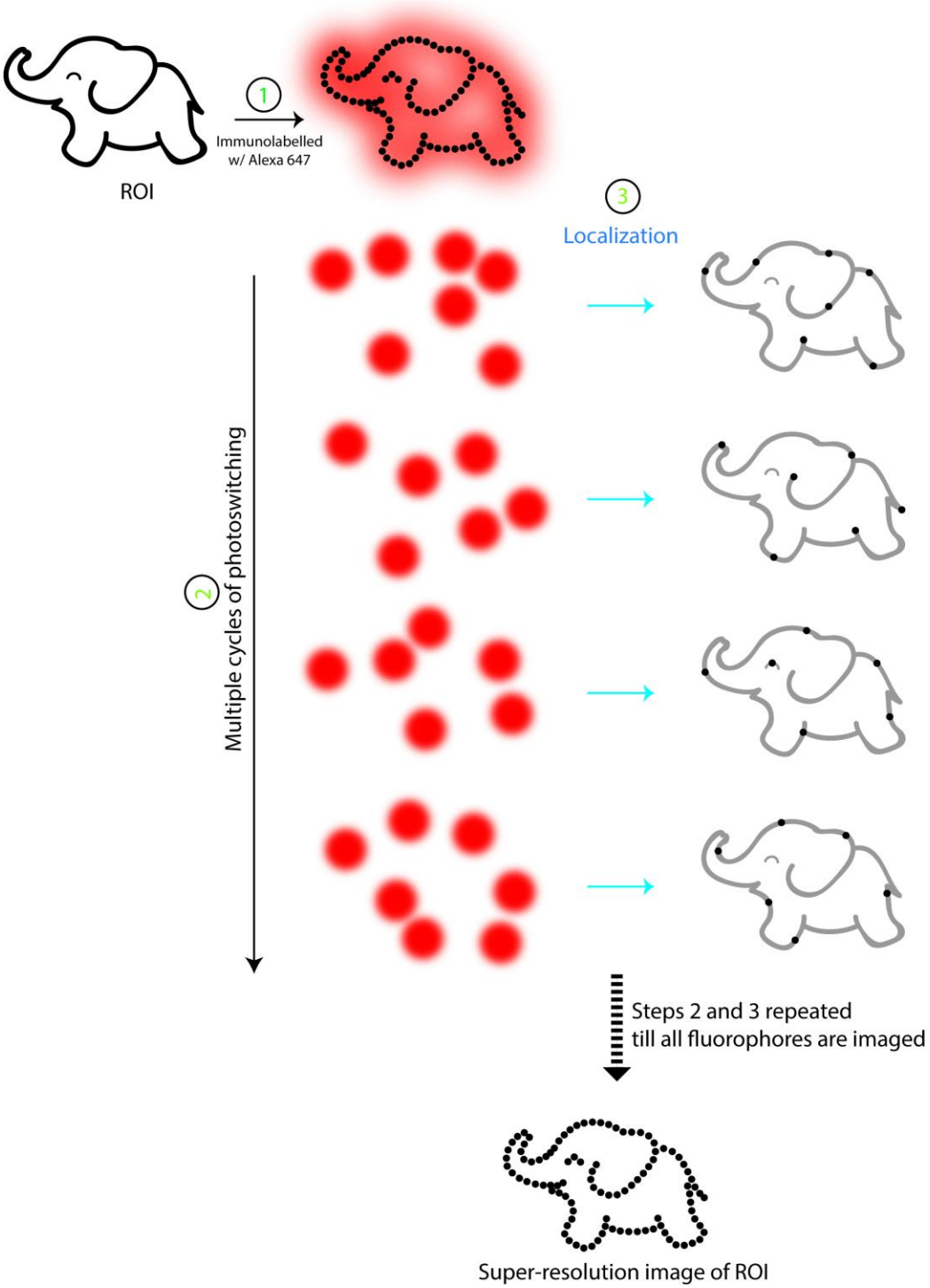
1
Immunolabelled
w/ Alexa 647
ROI
3
Localization
2
Multiple cycles of photoswitching
Steps 2 and 3 repeated
till all fluorophores are imaged
Super-resolution image of ROI

"blinking" of fluorophores). Finally, the images are processed and fitted with Gaussian PSFs to generate a super-resolution image.

As mentioned before, dSTORM enjoys the advantage of being able to use most conventional dyes for imaging. Ideally, the fluorophore must 1) have a high photon count for improved localization precision, 2) emit no photons in its "off" state for better contrast, and 3) have a low spontaneous activation rate so that only a few molecules are "on" at a time for high-resolution images. Alexa Fluor 647 is one of the most widely used dyes for dSTORM imaging because of its high photon yield and low duty cycles [Dempsey et al., 2011]. Unlike PALM, which solely relies on genetically encodable PA-FPs and PC-FPs, dSTORM dyes can be delivered to targets by using conventional immunohistochemical techniques. Although antibody labeling suffers from "linkage-errors" at high resolution, meaning that the size of the antibodies displaces the label from the epitope by ~20 nm, this can be avoided by using a new class of antibodies called nanobodies that are ~3 nm in size [Ries et al., 2012]. For targets that lack good antibodies and for live cell imaging, genetic labeling systems such as SNAP-tag, HALO-tag, CLIP-tag and TetraCys can be used to deliver the dye to the target of interest [Adams et al, 2002; Keppler et al., 2003;Gautier et al., 2008;Los et al., 2008].

The quality of dSTORM imaging depends on an appropriate ratio of the switching "on" and "off" rates, as they ensure that each fluorophore is recorded as a single molecule at a given time [Wolter et al., 2011]. A sufficiently large "off" rate is required to ensure that only a sparse subset of fluorophores is active in each image frame. Thus, for dSTORM imaging, the irradiation intensity and buffer composition are integral to determining the resolution of the final image

since they control the rate of transition from the fluorescent “on” state to the “off” state. While in the radical state, fluorophores can react with oxygen leading to irreversible photobleaching; as a result, most buffers contain oxygen-scavenging systems in addition to reducing agents [Wolter et al.,2011]. The photoswitching rates can be modified by adjusting the concentration of thiols, the buffer pH, and laser intensity to prevent photobleaching, thereby allowing for the super-resolution imaging of complex cellular structure with varying fluorophore densities in live and fixed cells [Heilemann et al.; 2009; Wombacher et al., 2010;Klein et al., 2011]. Live cell dSTORM exploits intracellular redox systems and oxygen to photoswitch dyes. Typically, a stack of 20,000 to 40,000 images is collected at frame rates ranging from 5 to 20 Hz until all the molecules have been imaged.

Post-processing of the images involves determining the centroids of individual PSFs recorded from fluorophores. As super-resolution methods gain popularity, more and more single molecule localization software packages such as rapidSTORM, quickPALM, and PYME, are becoming available to aid in the reconstruction of super-resolution images [Henriques et al., 2010; Wolter et al., 2012;Baddeley et al., 2009]. These software packages perform three basic functions: 1) spot identification, which involves identifying the PSF in each image, 2) spot fitting, which relies on robust algorithms to fit the Gaussian function to determine the centroid of the fluorophore, and 3) plotting all localizations into one super-resolution image. The uncertainty in determining the molecule’s position is governed by the laws of Guassian error propagation, which state that the localization precision scales inversely with the square root of the number of photons detected [Thompson et al., 2002]. Accordingly, single molecule approaches have achieved lateral imaging resolutions down to 20 nm [Rust et

al.,2006]. In addition to photon count, the density of fluorescent labels also affects the final resolution and accuracy of the image. To avoid undersampling, fluorescent densities up to 10^4 fluorophores/um^2 need to be considered whilst keeping the structure of the target in mind [Huang et al.,2009]. On the other hand, the over-labeling of structures should be avoided, as it is difficult to control switching contrast in densely labeled areas.

Baddeley an colleagues applied dSTORM imaging to determine the cluster size of RyRs in cardiomyocytes and showed that RyR clusters are much smaller than previously thought [Baddeley et al., 2009]. They developed a novel two-color 3D dSTORM method using a far-red excitation source called d^4STORM to study the colocalization of RyRs with Cav3 and JP [Baddeley et al., 2011]. Multiple 3D dSTORM approaches using astigmatism, two-focal-plane imaging or the phase-ramp approach have been developed, yielding localization accuracies of ~50 nm in the z direction [Huang et al., 2008; Juette et al.,2008;Baddeley et al.,2011].

1.2. Advances in EM

1.2.1 Transmission electron microscopy (TEM) and EM tomography

EM has historically fostered our understanding of E-C coupling. Cells and tissues were fixed, embedded in resin, and then sectioned thin enough for electrons to pass through them. Much of what we know about the detailed ultrastructure of cardiomyocytes and their E-C coupling domains is derived from examination of 60-100 nm thin resin sections, the mainstay of electron microscopy for almost 50 years. However, TEM is only capable of providing users with a translucent view of the sample, i.e. it works with large focus depth

and projects all objects within the entire thickness of sections onto a two-dimensional (2D) plane (a file or a CCD image sensor), causing the major loss of nano-scale details of 3D structures [Barcena and Koster, 2009]. In other words, resolution along the electron beam axis can not be lower than the thickness of sections, while lateral (x-y) resolution is less than one nanometer [Muller et al., 2008]. Intuitively, the easiest solution to this problem was to cut even thinner sections (40-50 nm) such that each section is effectively a 2D slice. This ultimately led to the development of serial section transmission electron microscopy (ssTEM) for 3D imaging [Sjöstrand 1958; Rieder 1981; Bron et al., 1990). Ribbons of consecutive sections were collected onto a grid using a microtome and the same ROI in each section was imaged. The images were then stacked, separated by section thickness to yield a 3D reconstruction of the ROI. Automated ultramicrotomes and efficient computer algorithms have made this process less labor intensive, and this technique is still used today [Kreshuk et al., 2014]. However, even if 10 nm thin serial sections were used, the z-resolution is still not comparable to the x-y resolution afforded by TEM.

With technological advancements in data acquisition, computing power, and the introduction of higher accelerating voltages, scientists became able to image thicker sections with lower chromatic aberrations for 3D analyses. However, they still faced the problem of overlapping organelles being superimposed into one blurry 2D image. Thus, the desire to sort and reconstruct the information from different z levels within the section led to the development of “electron tomography” or “EM tomography”, a computational approach to extract true 3D information from TEM. EM tomography relies on multiple 2D image projections, which are acquired while a specimen is incrementally tilted around

an axis (or axes) perpendicular to the electron beam, along with the application of the weighted back projection principle, which is used in medical computed axial tomography (CAT) scans [Frey et al., 2006; McIntosh , 2008]. The product is termed a “3D density map” or a “tomogram”, a 3D mass composed of arrayed volume elements (voxels), each of which has an assigned gray-scale value.

Intermediate high-voltage EM (IVEM) systems operating typically at 200-600 keV are often used in cell biology to ensure adequate resolution in specimens prepared as sections with sufficient thicknesses to contain major organelles and cellular micro-domains of interest. Typically, tilt angles are in the range of ±60-80 degrees with 1- or 2-degree increments. For example, a single-degree increment tile-imaging of ±60 degrees with double tilt-axes prepares 240 projection images to reconstruct a single EM tomogram. The addition of the 2nd tilt axis significantly improves the quality of tomograms by diminishing the Fourier missing wedge [Frey et al., 2006]. Recent reports from our lab have demonstrated that multiple tilt (>2) series allow averaging of data for better reconstructions [Ellisman et al.; 2014]. Fiducial gold markers added to the top and bottom of the section prior to imaging are used to align the image stack. Post-processing software packages such as SPIDER and IMOD implement the numerical approximation of the inverse Radon transformation by direct back projection to generate 3D reconstructions [Frank, 1981; Kremer et al., 1996]. Recently, iterative approaches have also been employed in tomographic reconstruction packages, such as TxBR, to further refine reconstructions [Lawrence et al., 2006; Phan et al., 2012]. It is known that 3D imaging with isotropic resolution in the 3-20 nm range is feasible in 500 nm or thinner sections with an IVEM operating at 300-400 keV.

As is the case with conventional TEM, samples used for EM tomography must undergo rigorous processing and fixation to preserve ultrastructure and withstand damage due to staining, dehydration, embedding, and sectioning, as well as imaging. Naturally, it is highly desirable to use the most optimal sample preparation techniques to minimize potential artifacts. Typical chemical fixation involves the primary aldehyde fixation of proteins followed by post fixation of lipids with osmification. Fixed samples then need to be dehydrated for resin infiltration. Each of these multi-step processes results in potential conformational changes to cellular structures. As a result, instantaneous fast freezing methods are preferable to chemical fixation for preserving tissues in their native states [McIntosh, 2001]. Sosinsky and colleagues further developed a new hybrid method that combines a low concentration (~0.1%) glutaraldehyde fixation with high pressure freezing and freeze substitution, and achieved high consistency in the structural preservation of tissue sections [Sosinsky et al., 2008]. While we have also been using this method in cardiac tissues with favorable results, it is important to realize that there is no absolute artifact-free EM sample preparation method for error-free EM imaging of cellular structures [Hayashi et al., 2009].

Tomogram interpretation is conveyed through segmentation, a process to decompose tomograms into anatomical components with different identities. A number of computational methods have been developed for automatic or semi-automatic segmentation of organelle structures in EM tomography [Volkmann, 2010; Fernandez et al., 2012]. A recent attempt applied a ridge detection method to segment membranes and myofilaments in a tomogram of mouse cardiomyocytes [Martin-Sanchez et al., 2012]. Nonetheless, the fidelity of computer-operated, or aided, segmentation is highly dependent on the resolution

and contrast of tomograms and, as a result, manual segmentation is still the most widely accepted and robust segmentation method. Unfortunately, the inter-operator variability in the results of the manual segmentation of biological objects in tomograms is not negligible, as assessed previously [Fernandez et al., 2012]. In our opinion, the most effective remedies for this problem are currently: (1) optimal noise reduction by computational image processing and (2) the common use and the declaration of simple yet rigorous definitions of anatomical features for manual segmentation. Ideally, rapid motif search algorithms can be used for bias-free identification of structures; however, the usefulness of such a method is still largely limited [Renken et al., 2009].

Individual cardiac CRUs are sufficiently small enough to fit in single EM tomograms prepared in IVEMs (Fig. XX); however, single EM tomograms are not large enough to demonstrate the cell-wide organization of E-C coupling regulatory structures. To satisfy this requirement, there are several methods available for enhancing the 3D volume of imaging, such as the use of ultra-high voltage EM, the application of energy filters, and serial-section EM tomography [Frey et al., 2006]. Furthermore, new automated or semi-automated sequential imaging methods have been developed in both TEM and scanning EM (SEM) (described briefly below), responding to the large-volume imaging demands of biologists [Briggman and Bock, 2012].

1.2.2. SEM, Array tomography and 3D-SEM

The scanning electron microscope was developed by Max Knoll in 1935 [Knoll, 1935]. In contrast to TEM, the electron beam only penetrates a few nanometers into the sample, effectively imaging just the surface of the sample.

Secondary electrons generated from beam-sample interaction are general collected to image surface topography, but if a surface is perfectly smooth, back-scattered electrons (BSE) can be used to illuminate sample contrast, resulting in TEM-like images. Thus, following the same principle of ssTEM, ribbons of serial sections can be collected on a silicon wafer, imaged and aligned to generate a 3D volume. This is called array tomography (AT), and was developed as a means to gain a better axial resolution than that afforded by confocal microscopy (Further discussed in chapter XX) [Micheva and Smith; 2010]. Despite its 3D capability, array tomography is quite labor intensive, as it requires time and specialized skill to collect, image, and align serial sections.

Alternative, automated approaches to AT including focused ion-beam SEM (FIB-SEM) and serial block-face SEM (SBEM), have enabled the visualization of the ultrastructure of whole cells and tissue samples [Young et al., 1983; Denk & Horstmann, 2004; Bushby et al., 2011). Instead of collecting serial sections and then imaging them, these methods image the surface of a plastic embedded specimen block with the progressive removal of thin sections, generating a stack of 2D images from which the 3D representation can be reconstructed. Unlike AT, the sections are destroyed/lost during removal and, as a result, the sections cannot be revisited for imaging. However, the automated nature of this technique combined with its high volume throughput has led to its widespread use in 3D EM studies [Peddie and Collinson, 2014].

In SBEM, an ultrathin section of the tissue is removed by an automatic ultra-microtome and a low voltage BSE image is obtained [Denk and Horstmann, 2004]. This process is repeated until the desired size of volume has been imaged. We recently reported the use of SBEM to visualize the T-system and

mitochondria in cardiomyocytes [Yan et al., 2012; Wong et al., 2012] .The resolution of SBEM is limited mainly by two factors. The first is the sectioning thickness, which is practically limited to 50-70nm. The other factor is how deeply the electrons from the primary electron beam penetrate the specimen's surface while they are interacting with atoms and generating BSEs. Ideally, the depth of the BSE signal origin could be reduced to ~20 nm. In contrast, FIB-SEM relies on a beam of gallium ions to ablate the sample surface, removing sections as thin as 5 nm [Peddie and Collinson, 2014]. As a result, FIB-SEM 3D volumes can achieve isotropic resolutions comparable to the lateral resolution of TEM, albeit with a limited total volume of approximately 50 um^3 [Ballerini et al., 2001]. Unlike SBEM, only the ROI is ablated, which allows other parts of the block-face to be imaged later. Accordingly, while SBEM and FIB-SEM have the advantage of obtaining a large number of serial images without the need for alignment and distortion correction, they both provide volumetric data with significantly lower resolution than EM tomography.

1.3. Membrane systems for local myofilament activation via E-C coupling

The general concept of E-C coupling in muscles was established in the middle of the 20th century, well in advance of the identification of its molecular constituents, which include ion channels involved in Ca-induced Ca release (CICR), sarcolemmal and SR ion transporters, and their upstream regulators [Dulhunty, 2006]. The membrane organelle first linked to the control of myocyte contraction and relaxation was the SR. Following the somewhat obscure first EM demonstration of SR in cardiac muscles, which resembled that of skeletal muscles presented by Bennett and Porter, a landmark paper of Porter and

Palade depicted a uniquely formulated two-component membrane structure in cardiomyocytes, which they named a “dyad” [Bennett and Porter, 1953; Weinstein, 1954; Porter and Palade, 1957]. The dyad was identified as a dilated vesicle and a thinner vesicular element enwrapping the vesicle at the I-band level of myofibrils. The dilated vesicle, which we now know as a T-tubule, or T-system, was thought to be part of the SR at the time. Similarly, “triads” were also identified in skeletal muscles [Porter and Palade, 1957].

Similarities between the middle element of triads and the T-system, as well as the continuity of the T-system to the surface sarcolemma in skeletal muscles, led Huxley and Taylor to hypothesize that these cellular components conduct membrane depolarization inward and “locally activate” the contraction of myofibrils [Robertson, 1956; Huxley and Taylor, 1958]. A direct connection between inner cellular membranes and the sarcolemma was also hypothesized in the cardiac muscle [Moore and Ruska, 1957]. However, it took several years for scientists to obtain compelling evidence of the direct communication between the T-system lumen and the extracellular space, using EM and fluorescent microscopy [Page, 1957; Nelson and Benson, 1963; Franzini-Armstrong and Porter, 1964; Huxley, 1964; Peachey, 1965]. Since the diameter of the cardiac T-system is 3-5 times thicker than that of skeletal muscles, the connection of sarcolemmal invaginations to the T-system was more easily discernible in cardiac muscles, including human ventricular cardiomyocytes [Battig and Low, 1961; Simpson and Oertelis, 1962; Fawcett and McNutt, 1969]

1.4. Cellular architectures to restrict local Ca releases

Since Ringer's signature study in frog hearts, Ca ions have been recognized as the key intracellular messenger for cardiac muscle contraction [Ringer, 1883]. In the most simplified working model, the pathway from membrane excitation to contraction is the coupling of two cellular mechanisms involving Ca fluxes. CICR from SRs through ryanodine receptors (RyRs) is an autonomic cyclic reaction due to SR refilling by the action of the sarco-endoplasmic reticulum Ca-dependent ATPase (SERCA) [Frank, 1980; Bers, 2008]. Another major Ca flux, i.e. voltage-gated influx of Ca ions from the extracellular space, primarily involves L-type Ca channels (LTCCs), which are sensitive to dihydropyridine. EM played a significant role in locating these channel molecules in different membrane components and connecting CICR with the voltage-gated trans-sarcolemmal Ca influx (For more detail please refer to Chapter 4).

First, EM identified SR as an organelle for Ca accumulation (Ebashi's relaxing factor) [Ebashi and Lipmann, 1962; Constantin et al., 1965]. CICR was first demonstrated in skinned skeletal muscles as a phenomenon in which Ca accumulated in the SR is released by externally added Ca, followed by a study by Fabiato, which demonstrated CICR in cardiac muscles [Endo et al., 1970; Ford and Podolsky, 1970; Fabiato and Fabiato, 1972]. Discovery of CICR led to the identification of RyRs as the SR Ca leak channel [Fleischer et al., 1985]. Subsequently, the seminal paper published by Inui et al. used EM to reveal that RyRs molecularly make-up SR "feet", periodic densities residing in the SR membrane, bridging the 10-15 nm membrane gaps in dyads, triads, and at junctions between surface sarcolemma and opposed SR (i.e. peripheral couplings) [Inui et al., 1987]. Back then, the identity of the "feet" was unknown, but cell biologists were aware of peculiar "periodic densities" residing within the

10-15 nm membrane gaps in these membrane junctions. They were described in multiple ways, such as processes, projections, dense materials, globular densities, bridges, and then “feet”, in reports of bat cricothyroid muscle and toadfish swimbladder muscles by Revel, in fish muscles by Franzini-Armstrong and Porter, and ultimately in cardiac muscle cells (Fig. 1.4) [Revel, 1962; Franzini-Armstrong, 1964; Johnson and Sommer, 1967; Fawcett and McNutt, 1969; Walker et al., 1971; Franzini-Armstrong; 1980].

In contrast, freeze-fracture EM was demonstrating numerous inter-membrane particles in the sarcolemma of both non-fixed and fixed cardiac myocytes [Frank et al.,1985]. Franzini-Armstrong et al. recognized that the surface membrane domains where the large-sized particles (~8.5 nm) were enriched correlated with SR foot arrays both in skeletal and cardiac muscles, and thus speculated that these large-sized particles represent LTCCs [Sun et al., 1995]. Nonetheless, there was a difference in the distribution patterns of the large-sized particles between cardiac and skeletal muscles. In cardiomyocytes, the large-sized particles did not form tetrads as shown in skeletal muscles [Sun et al., 1995]..These historical EM findings led us to our current consensus about the anatomical portrait of cardiac E-C coupling machinery, i.e. junctional and dyadic “clefts” between the sarcolemma and SR and associated membrane structure, forming “couplons” as theorized by Stern et al. [Langer and Peskoff, 1996; Stern et al., 1997] . Fig. 1.5 shows the entire 3D structure of membrane organelles involved in calcium handling (excluding mitochondria) in a 500 nm section of mouse ventricular cardiomyocytes [Hayashi et al., 2009].

Figure 1.4. : Ion channels and structures involved in E-C coupling. Ca enters the into the junctional membrane space through depolarization-activated LTCCs/DHPRs (dihydropyridine receptors) which triggers Ca release from the RyRs. During relaxation, Ca is removed cytosol via the NCX (Sodium calcium exchanger), PMCA (Plasma membrane calcium adenosine triphosphatase), SERCA mitochondrial uniporter and Ca buffers. The protein junctophilin (JP2) maintains couplon architecture. (CryoEM map of RyR1 channel (EMDB 1606) was uploaded from https://www.cgl.ucsf.edu/chimera/) [Pettersen et al., 2004].

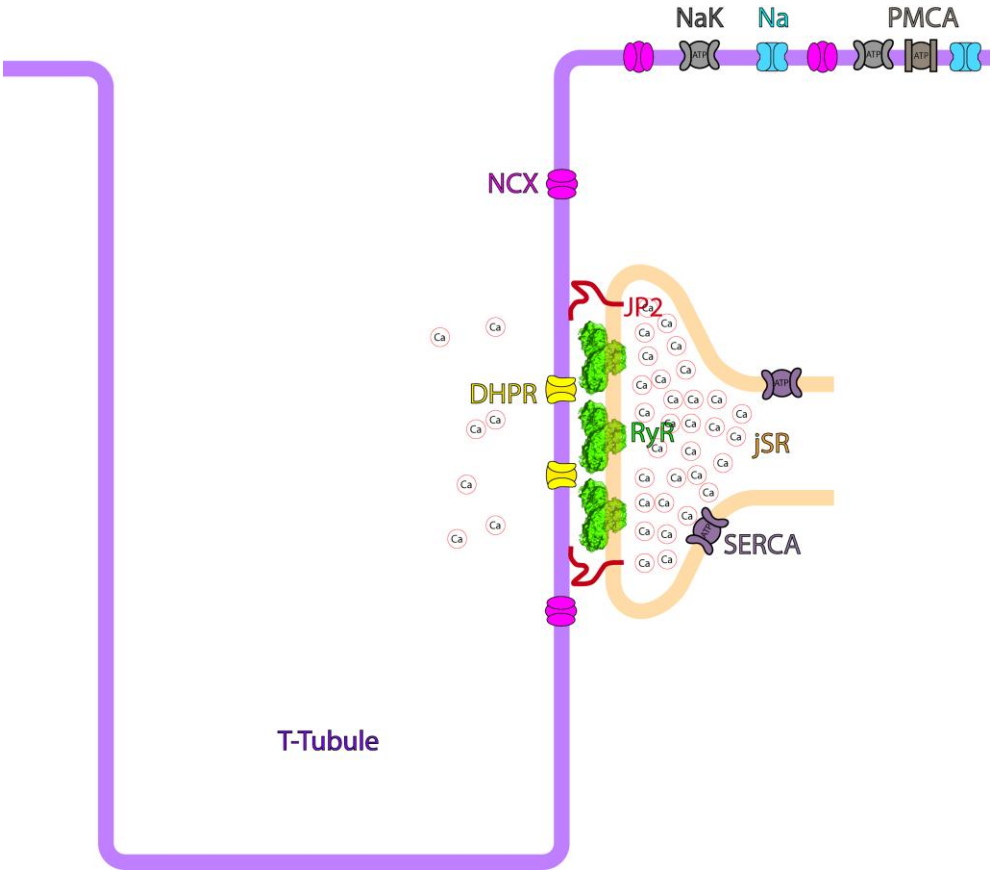
NaK
Na
PMCA
NCX
JP2
DHPR
RyR
jSR
SERCA
T-Tubule

1.5. RyR

RyRs are Ca channels localized on the SR/ER, named after the plant alkyloid ryanodine, which binds to the receptor with high affinity and specificity [Imagawa et al., 1987; Inui et al., 1987; Lai et al., 1988; Chu et al., 1990]. They exist as three mammalian isoforms; RyR 1, RyR 2, and RyR 3 (Sutko, 1985). The RyR 1 isoform is primarily expressed in skeletal muscle with minor levels in cardiac tissue [Takeshima et al., 1989, Zorzato et al., 1990]. RyR 2, known as cardiac RyR, is predominantly found in cardiac muscle, as well as in the Purkinje cells of the cerebellum and cerebral cortex [Nakai et al., 1990; Otsu et al., 1990]. RyR 3 is expressed in varying levels across the Purkinje cells, hippocampus, and thalamus [Hakamata et al., 1992; Lai et. al, 1992]. RyR 1 and RyR 2 are predominantly responsible for E-C coupling in skeletal muscle and cardiac muscle, respectively. There is evidence that RyR 3 is required for efficient contraction in neonatal skeletal muscles as well [Bertocchini et al., 1997]. The role of RyR 3 in neuronal processes is yet to be clear, but recent studies have shown that RyR 3 along with RyR 2 play critical roles in the modulation of memory processes [Galeotti et al., 2008].

RyRs are homotetrameric, with each monomer weighing ~565 kDa, making RyRs the largest known ion channel (>2 MDa). The RyR channel has two distinct domains: (1) a large cytoplasmic assembly connected to (2) a transmembrane assembly [Wagenknecht et al., 1989; Radermacher et al., 1994; Serysheva et al., 1995] (Fig. 1.6). The cytoplasmic portion forms a square prism shape (~29 × 29 × 12 nm), seen in electron micrographs as “feet” sandwiched between the T-tubules and SR as described above. The cytoplasmic side facilitates interactions with regulatory ligands, cellular processes and

Figure 1.5. : EM tomographic reconstruction of cellular structures involved in calcium signaling in mouse myocardium. (**A** and **B**) The entire sarcolemma (green) including surface sarcolemma and T-system, junctional SR (jSR, yellow), couplons (CRUs, red), and network SR (nSR, blue) are segmented in a tomogram (xyz, 3.8 μm x 5.7 μm x 0.43 μm), and their surface mesh models are shown. Both (**A**) and (**B**) give a bird's eye view of the geometric mesh models displayed with one of the 2D slices image in a 3D borderline box (yellow lines) at different angles. The shape of the T-system is highly polymorphic creating complex junctional associations with the jSR. Couplons (CRUs) are spatially clustered at the Z-lines and widely distributed along the sarcolemma. The nSR runs between the myofibrils forming a highly branched lace-like network. Scale Bars, 500 nm. Segmentation is updated from a previously published tomogram [Hayashi et al., 2009].

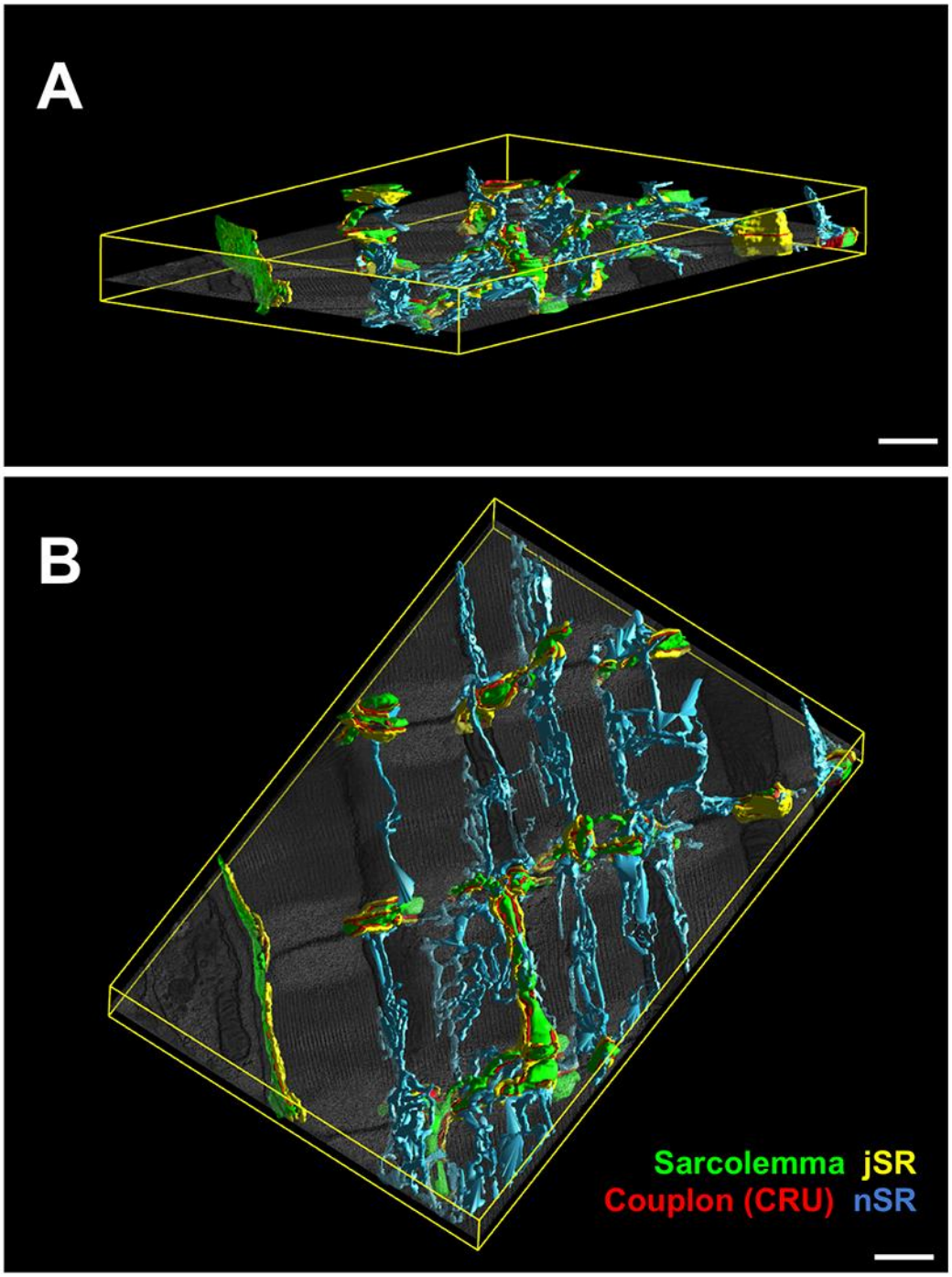
A
B
Sarcolemma jSR
Couplon (CRU) nSR

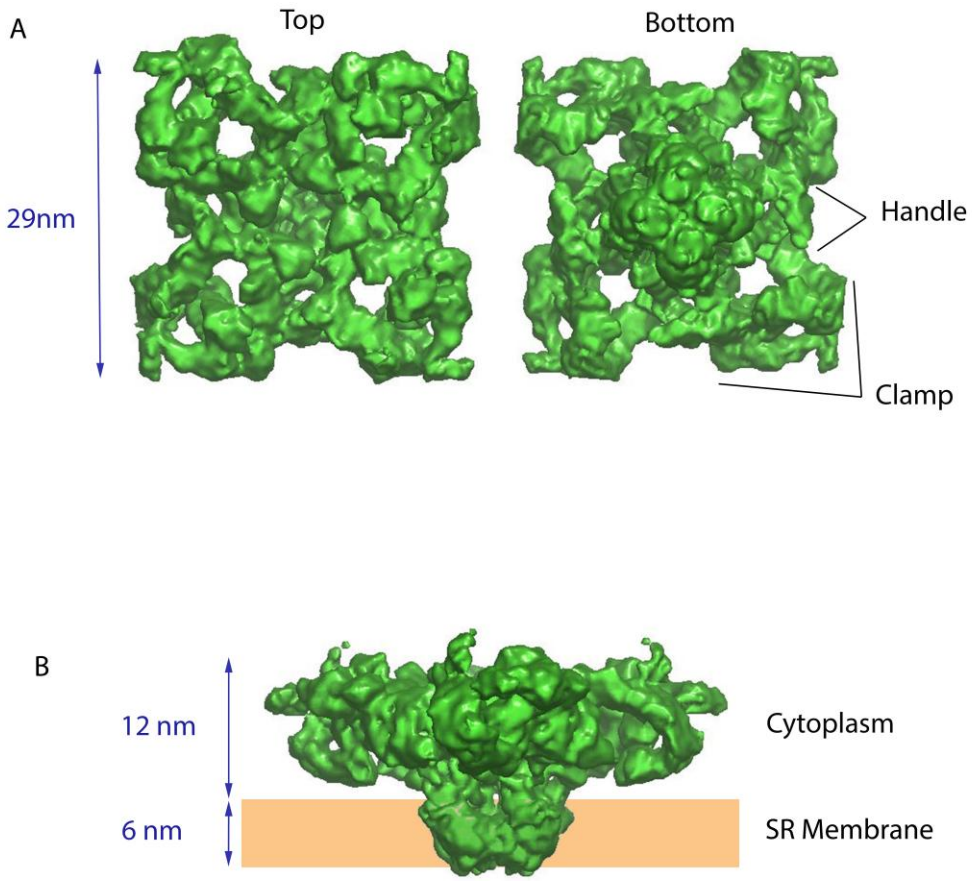

Figure 1.6. : CryoEM map of RyR1 tetramer as viewed from the cytoplasm (A), and from the side (B). The cytoplasmic portion forms a square prism (~29 × 29 x 12 nm) as viewed from the top and bottom in (A). The “clamp” and “handle” regions have been identified in (A). (CryoEM map of RyR1 channel (EMDB 1606) was uploaded from https://www.cgl.ucsf.edu/chimera/) [Pettersen et al., 2004].

pharmaceutical agents, and undergoes conformational changes during the opening and closing of the channel. The transmembrane portion (~7 nm), which is embedded in the SR/ER, is attached to the center of the cytoplasmic assembly and contains a ~3 Å wide Ca-selective pore. Single RyR channel recordings have revealed that all the isoforms demonstrate comparable permeation and gating properties. All three mammalian RyR isoforms share similar 3D structure as well as function owing to their high sequence homology (~70%) [Takeshima et al., 1993]. Isoform specific structural heterogeneities result in a diverse range of responses to some modulators. Low cytosolic Ca concentrations (1-10 μM) generally activate RyRs, whereas high concentrations (1-10 mM) inhibit RyR activity.

1.5.1. RyR ultrastructure

Most single particle cryo-EM analyses have focused on RyR 1 because these highly abundant skeletal receptors are relatively easier to isolate in sufficient quantities and are more structurally stable than RyR 2 in cryo-EM imaging conditions [Radermacher et al. 1992; Radermacher et al. 1994; Serysheva et al. 1995; Serysheva et al. 2008; Samsó et al. 2009]. To combat this issue, Sharma and colleagues developed a RyR 2 stablizing imaging protocol to prevent the distortion and aggregation of RyR 2 during cryo-EM imaging, becoming the first group to produce a 3D reconstruction of RyR 2 at the resolution of 41 Å [Sharma et al. 1998]. As expected, RyR 1 and RyR 2 reconstructions shared similar overall structures owing to their high sequence homology. The regions of variability in the primary sequence of the receptors that are most likely responsible for the unique functioning of each isoform have been

identified and termed as divergent regions 1, 2 and 3 [Sorrentino and Volpe, 1993]. As described earlier, the cytoplasmic square prism structure of the RyR is connected to the transmembrane portion (12X 12 X 6 nm), which forms the ion-conducting pore. The RyR has been structurally subdivided into 15 subdomains which form the “clamps” (subdomains 5, 6, 7, 8, 9, and 10), the “handle” (subdomains 3 and 4), the “central rim” (subdomains 1 and 2) on the cytoplasmic face, and the connecting “column” (subdomains 11 and12) [Serysheva et al. 2008; Samsó et al. 2009]. Subtraction of the RyR 1 structure from a RyR 2 reconstruction confirmed the structural variability in the isoforms at the corners of the cytoplasmic region called the “clamps”. This is consistent with the hypothesis that the clamps undergo conformational changes during gating and likely carry the interaction sites for modulators as well as neighboring RyRs. Recent efforts to optimize buffer detergents to stabilize ion channels as well as breakthroughs in single particle cryo-EM technologies have resulted in 3D reconstructions at a resolution of 4.8 Å and have successfully concluded that the ion-conducting pore belongs to the six-transmembrane ion channel superfamily [Zalk et al., 2015].

1.5.2. RyR regulation

RyR functioning is modulated by several factors, including ligand molecules such as Ca, ATP, and Magnesium (Mg), physiological processes such as phosphorylation and oxidation, pharmacological agents such as ryanodine and caffeine, and regulatory proteins such as calmodulin, calsequestrin (CSQ), and FK-506 binding proteins (FKBP). Most RyR modulators, except for junctin, triadin, and CSQ, modulate RyR behavior by binding to the cytoplasmic domain

of RyRs. Co-immunoprecipitation of peptides and difference mapping of cryo-EM structures has proven to be very useful in identifying binding locations for some of these modulators, such as calmodulin and FKBP proteins [Wagenkecht et al., 1997]. Antibodies were used in conjunction with single particle cryo-EM studies to localize the specific domain that may be involved in the Ca-dependent regulation of RyRs [Benacquista et al., 2000]. Understanding the properties of these regulators is critical because cardiac E-C coupling is completely dependent on the ligand regulation of RyR (Bers, 2002)

1.5.2.1. Regulatory ligands

Ca regulates RyR functioning directly, as well as indirectly, through calmodulin (CAM) and kinases. Micromolar Ca concentrations activate RyRs, whereas millimolar concentrations inhibit them, resulting in a bell-shaped dependence on cytosolic Ca concentration. This behavior is attributed to the presence of multiple Ca regulatory sites on the RyRs: three cytosolic sites (activation site A and two inhibitory sites, I1 and I2) and one luminal activation site with sensitivities to Ca, which vary inversely with their distance from the channel pore [Laver, 2007; Laver, 2010]. Luminal Ca dependence was confirmed via single RyR channel studies and the functional analysis of luminal domains, however the mechanism of regulation is not yet clearly defined [Sitsapesan and Williams, 1994; Ching et al., 2000]. The sensitivity of the RyR channel to cytosolic agonists was observed to increase at high luminal Ca levels [Smith et al., 1986; Sitsapesan and Williams, 1995; Györke and Györke, 1998; Xu et al., 1998; Laver et al. 2004]. Luminal Ca regulates RyR functioning either by interacting with the luminal activation site or by the interaction of Ca flowing

through the pore from the luminal side with cytoplasmic Ca regulatory sites [Laver, 2007]. Computational modeling studies have suggested that luminal and cytoplasmic Ca produce synergistic activation of RyRs [Laver and Honen, 2008].

The total ATP concentration in the cell cytosol is ~5 mM, and that of free Mg is 1 mM. Magnesium ions modulate RyR 2 activity in the cytoplasm by inhibiting RyR function at elevated concentrations by either binding to low affinity Ca sites or by reducing the RyR opening probability by competing with high affinity Ca inhibition sites [Meissner et al., 1986; Laver et al., 1997]. Using EM tomography, studies demonstrated that high concentrations of Mg also affect RyR channel organization, causing them to reorganize from their checkerboard arrangement into a denser, side-by-side arrangement [Asghari et al., 2014]. Recent studies have also indicated that luminal Mg inhibition comes into play at < 1 uM cytoplasmic Ca concentrations [Laver and Honen, 2008]. Ryanodine binding studies and single channel recordings have shown that cytosolic free ATP binds to and activates cardiac RyRs only in the presence of Ca [Meissner and Henderson, 1987]. This process also increases both the opening rates and durations of RyRs, stabilizing their open conformation.

1.5.2.2. Regulatory proteins

CaM is a 148aa cytosolic Ca binding protein (~17 kDa) that modulates RyR gating by directly interacting with RyRs. It binds to one unit per tetramer and regulates RyR functioning in its Ca free and bound form. Its effects vary with different isoforms. In cardiac tissue, CaM decreases RyR opening at all Ca concentrations and alters the Ca- dependent activation of RyRs. In rat cardiac myocytes, the cellular concentration of CaM is around 2 to 6 μM, depending on

the species (Maier et al., 2006). In normal physiological conditions, CaM binds to more than 70% of RyR2 with a high affinity and inhibits SR Ca release. This is important as decreased association between CaM and RyR2 has been observed during heart failure, which may be one of the factors involved in SR Ca leak [Yang et al., 2014]

CSQ controls the intracellular Ca concentration and regulates SR Ca release. It acts as a major intra-SR Ca buffer and has been shown to aggregate in junctional domains of the SR where the RyRs reside (Franzini-Armstrong et al., 1987]. It is believed to be physically coupled to RyRs via triadin and junctin, forming a macromolecular signaling complex. Such physical interactions suggest that Ca binding induced conformational changes in CSQ may modulate RyR channel activity. In addition, lipid bilayer studies have revealed that the CSQ inhibits the open probability of RyR at low luminal Ca concentrations and is relieved at high luminal Ca concentrations [Gyorke et al., 2004, Gyorke et al., 2009].

FKBPs are a family of immunophillin proteins that are expressed in most tissues and are involved in a host of cellular functions, including protein folding, trafficking and receptor signaling. In the heart, FKBP isoforms FKBP 12 and 12.6 bind stoichiometrically to RyR and co-purify with RyRs [Timmerman et al., 1993; Timmerman et al., 1996]. The binding affinities of these proteins vary among the RyR isoforms. Despite sharing 85% sequence homology and having similar structures, there is at least an ~8 fold difference in their binding affinities to RyR 2 [Jeyakumar et al.,2001; Deivanayagam et al., 2000; Guo et al., 2010] . Additionally, in most species, FKBP 12 is at least 10x more abundant than FKBP 12.6 in the heart and it binds with a lower affinity than FKBP 12.6 to RyRs.

CryoEM has successfully mapped the binding site of FKBP 12 to be in between subdomains 3, 5, and 9 on the 3D reconstruction of RyR [Wagenkecht et al., 1997]. The impact of FKBP binding on RyR activity still remains controversial. FKBPs are thought to bind to RyRs and stabilize the closed state of the channel under physiological conditions [Ahern et al., 1994; Brillantes et al., 1994; McCall et al., 1996; Ahern et al., 1997; Marx et al., 1998;Marx et al., 200]. There are conflicting reports on whether the removal of FKBP 12.6 by phosphorylation or immunophilin agents from the RyR channel activates it and induces a subconductance state [Timmerman et al.,1996; Kaftan et al., 1996; McCall et al., 1996; Barg et al., 1997; Xiao et al., 1997] Recent studies by Guo et al. have shown that FKBP binding to RyR is unaffected by phosphorylation and only FKBP 12.6 affects RyR basal activity [Guo et al., 2010]. FKBP 12.6 KO mice demonstrated altered Ca spark characteristics, whereas FKBP over-expression resulted in increased SR load and enhanced contraction, suggesting that FKBP binding plays a role in E-C coupling [Prestie et al., 2001; Fill and Copello , 2002; Xiao et al., 2007].

Further analysis of RyR structure has revealed multiple sites for phosphorylation on the cytoplasmic domain of RyRs. For decades, the enzymes involved in phosphorylation have been studied to elucidate the functional implications of phosphorylation on RyR functioning, however much is still up for debate. Unlike CAMKII, Protein kinase A (PKA) is physically anchored to the RyR via mAKAP protein [Marx et al.,2000; Marx et al., 2001]. Some groups report that PKA-dependent phosphorylation enhances the open state probability of RyRs, whereas other groups have observed a decrease in basal proability of opening (Po) [Valdicia et al., 1995; Marx et al., 2000; Marx et al., 2001]. Similarly, there

are mixed reports on whether CAMKII increases or decreases the Po of RyR [WItcher etal., 1991, Hain et al., 1995; Lokuta et al., 1995] . PKA phosphorylation participates in the flight-or-fight sympathetic response by changing RyR gating properties, enabling larger and faster Ca transients [Valdivia et al., 1995; Li et al., 2000; Kentish et al., 2001; Reiken et al., 2003]. The role of PKA-dependent hyper-phosphorylation in heart failure is controversial. Some groups have reported that FKBP disassociation in response to PKA-phosphorylation creates "leaky" RyRs, which reduce SR Ca content, resulting in decreased muscle force production [Marx et al. 2000; Reiken et al. 200]. However, others have reported the absence of PKA-dependent hyper-phosphorylation in failing hearts [Xiao et al., 2005]. Despite these controversial findings, we can conclude that PKA-dependent phosphorylation is functionally important for E-C coupling, and further investigations in more physiological cellular environments are required to extrapolate molecular findings to the physiological setting.

1.5.3. RyRs in E-C coupling and its relationship with cardiac nano-anatomy

Ca ion diffusion originating from RyRs has been observed as a central signaling mechanism for E-C coupling. Along with the discovery of localized short-duration cytoplasmic Ca elevations termed "Ca sparks" using highly sensitive Ca indicator dyes and high-speed confocal microscopy, the "local control" theory was introduced, asserting that E-C coupling is the stochastic summation of the activation of "couplons" [Jewett et al., 1973; Stern, 1992; Cheng et al., 1993; Cheng, 2008]. Ca sparks are shown as ~2.0 μm wide (~8 fl) local transient cytoplasmic Ca elevations lasting ~20-30 msec (10 msec to peak): their peak Ca current is estimated to be ~3-4 pA [Cheng, 2008]. In this regard, a

question that has repeatedly been raised is how RyR clusters generate Ca sparks. While a classic model of CRU assembly dominates (i.e. more than 100 RyR tetramers constitute one CRU and ~2-5 CRUs are within the volume of one Ca spark), biophysicists have tried to understand why the majority of RyRs in CRUs stay silent during the activation of Ca sparks, each of which is generated by a small fraction of RyRs (6-20 RyR tetramers). The issue is also related to several experimental findings. For example, smaller sized Ca release events provoked by the use of caged Ca compounds [90] and heterogeneity of Ca spark dynamics [46, 72] [Lipp and Niggli, 1998; Wang et al., 2004; Hayashi et al, 2009]. While fundamental questions do not change, the quantization of local Ca release events has to be linked to the new knowledge of CRU nano-architecture, which has emerged via the application of novel microscopic imaging technologies (see above).

1.6. Perspective

While microscopic technologies are advancing rapidly in both EM and LM and the gaps in resolution and volumes between these different imaging modalities are closing, the integration of molecular imaging, which is mainly carried out by LM, and the structural determination of cellular organelles by the use of EM is becoming a more significant issue. LM approaches, including diffraction-limited and sub-diffraction-limited LM, can only visualize labeled targets, not the cellular environment. As a result, it is difficult to localize proteins in their membrane sub-domains due to the lack of resolution and reference space. Fig. 1.7 illustrates the relationship between RyR clusters and the CRU anatomy. It demonstrates how different imaging techniques can interpret the

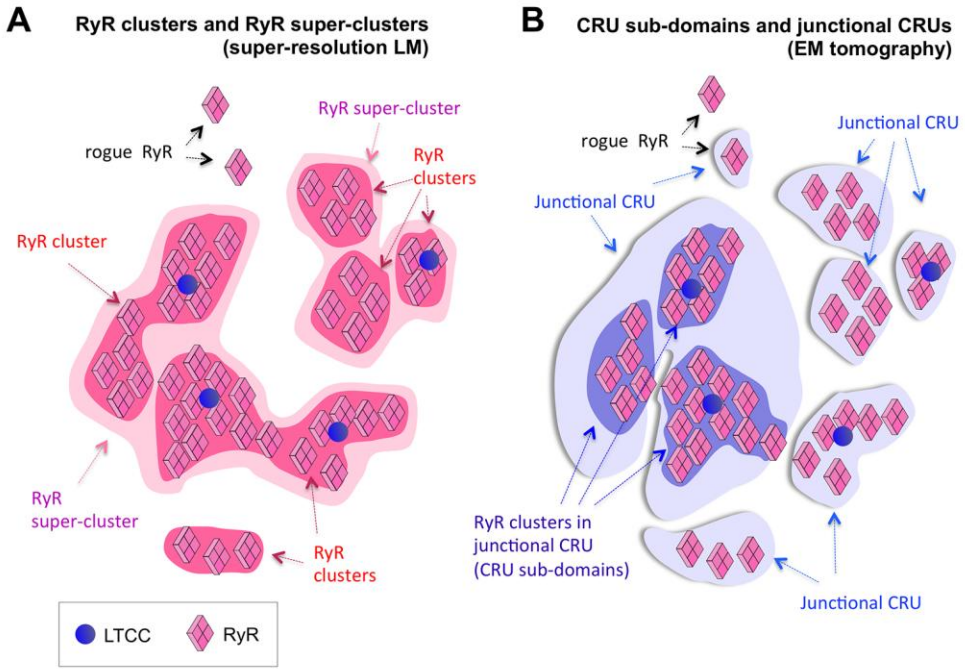

Figure 1.7. : Differences in the identification and grouping of RyR clusters between super-resolution LM (A) and EM tomography (B). (**A**) and (**B**) schematically show how two microscopy techniques differently interpret identical RyR distribution. **A** demonstrates how RyRs are visualized in super-resolution light microscopy. Immuno-stained RyRs appear as clusters (red). Baddeley et al. proposed RyR clusters in close proximity (within 100nm of each other) are probably activated together as larger units, i.e. “super clusters” (pink) [Baddeley et al., 2009]. The grouping of RyRs is defined solely by their 2D coordinate registration in images. In contrast, in EM tomography, membrane anatomy separates RyR clusters into groups. Large dyadic CRUs tend to contain some RyR clusters as CRU sub-domains (blue). CRU subdomains in the same junction are more likely to work as a single CRU (light blue) since their activation sites are in the same cleft space and they share the same jSR cistern as a calcium source as well as a termination mechanism through calcium depletion. This highlights the need to integrate EM imaging and light microscopic imaging to accurately understand CRU architecture.

same RyR distribution differently. Using immunostaining techniques, RyRs are grouped into clusters and “super clusters” based on their relative positions with respect to each other. In contrast, EM can group RyRs based on their position with respect to membrane anatomy. Clusters of RyRs, which share the same junctional space for activation, as well a common junctional SR (jSR) Ca source, are more likely to work together than RyRs, which are grouped together based on physical proximity alone. Along the same vein, determining sub-cellular RyR distributions inside and outside the cleft using LM approaches relying on co-staining with membrane markers would inherently be inaccurate. In short, RyR clustering determined in LM by the use of molecular channel probes does not fully consort with the subcellular compartmentation of this molecule confined by membrane boundaries. As in many other fields of scientific research, this affirms that any single technology is insufficient to improve our knowledge.

The extent of physiological variability is also important to understand how structural changes (i.e. cellular remodeling) affect E-C coupling in disease settings. New cellular geometry data and molecular distributions strongly support attempts of mathematical simulation models using realistic cellular geometry. This is in contrast to most current models for E-C coupling simulations, which employ simplified geometric representations and disregard the spatial relationships between organelles, such that reaction-diffusion relationships of ions and other regulatory molecules are completely dismissed. The impact of realistic geometries included in reaction-diffusion calculations is exemplified in a recent study by Hake et al. [Hake et al., 2012]. In this report, Hake and colleagues included a geometric model of membrane organelles obtained from EM tomography, which enabled them to simulate local SR Ca releases (Ca

sparks) and depletion, i.e. a Ca blink, in a variety of model conditions. We anticipate that the combination of LM and volume imaging will further refine such modeling research environments.

To this end, there has been substantial effort to combine immuno-based and/or fluorometric methods with volume EMs, which include EM tomography and SBFSEM. Cryo-immuno-EM with the use of a Nanogold probe has been carried out in EM tomography [Zeuschner et al., 2006; Ladinsky and Howell, 2007]. Sub-diffraction limited light microscopy imaging of photoactivatable fluorescent protein-tag molecules was combined with a volume EM technique by Kopek and associates [Kopek et al., 2012]. It is important to point out the recent development of various molecular probes designed specifically for correlative (in the same sample) or correlated (in the same section) light and electron microscopic (CLEM) imaging [Ellisman et al., 2012]. Although CLEM is highly technically demanding and therefore has not yet been applied to cardiac myocytes, we predict that it will become imperative to employ CLEM imaging approaches in future studies to realize how local Ca releasing machineries and their control systems are assembled in cardiomyocytes.

With this in mind, one of the major goals of the work presented in this dissertation was to establish a CLEM technique to determine the distribution of proteins with respect to high resolution maps of cellular anatomy in cardiomyocytes. The development of this technique and its implementations in 2D and 3D will be described in Chapter 2. Chapter 3 will discuss the application of this technique towards discerning the distribution of RyRs inside and outside of the dyadic domain. The distribution of diverse E-C coupling molecules other than RyRs will be examined in Chapter 4. Finally, Chapter 5 will discuss the

implementation of this novel CLEM technique to study a biologically important question, namely, the relationship between RyR compartmentalization and junctophilin.

This chapter, in part, is a reprint of the material as it appears in Journal of Molecular and Cellular Cardiology, 2013. Das T, Hoshijima M. The dissertation author was the primary investigator and author of this paper. This chapter, in part, is currently being prepared for submission for publication of the material. Das T, Hoshijima M. The dissertation/thesis author was the primary investigator and author of this material.

Chapter 2:

Development of New Correlated Super-Resolution Light Microscopy and Electron Microscopy Methods

2.1. Introduction

Super-resolution approaches are narrowing the gap between light microscopy and high resolution EM imaging. However, although fluorescently labeled molecules can now be resolved at ~20 nm resolution, investigators are still left “in the dark” regarding the cellular context of these molecules. EM imaging, on the other hand, offers high-resolution visualization of the cellular ultrastructure and organelles. Thus, combining super-resolution techniques with EM would allow us to determine the distribution of molecules of interest directly on nano-resolution geometric maps of biological structures. However, “correlated” LM-EM (CLEM), in which the same region of interest is imaged using LM and EM [Sosinsky et al., 2012], has been one of the most challenging fronts of technology development in microscopic imaging due to highly contradictory requirements for sample preparations used for LM versus EM. In the following section, we will review the current state of correlative/correlated LM-EM imaging strategies.

2.2. Advances in correlated light and electron microscopy

The fluorescence of both chemical and recombinant protein probes used in LM is difficult to preserve through the extreme pH changes, dehydration, and heavy metal staining used in conventional EM sample preparations. As a result, traditional “correlative” techniques imaged the sample with LM first and then treated the samples for EM imaging [Muller-Reichert et al., 2007; Verkade, 2008; Murphy et al., 2011; Loschberger 2014]. Such “pre-embedding” CLEM techniques have proven to be highly valuable because they allow cells to be imaged live. Fiducial makers or anatomical landmarks of specimens were used to

correlate LM to EM [Muller-Reichert et al., 2007; Verkade, 2008; Murphy et al., 2011].

Alternatively, my lab, along with others, developed a series of fluorescent tags and probe technologies for CLEM to achieve molecular-specific EM contrasts after sample processing. These technologies include quantum dots, FluoroNanogold, diaminobenzidine (DAB)-oxidation reactions using either immunolabeled eosin, genetically expressed markers such as tetracysteine-based protein tags with FlAsH and ReAsH, mini Singlet Oxygen Generator, FLIPPER, and APEX [Deerinck et al., 1994; Takizawa et al., 1998; Takizawa and Robinson, 2000; Gaietta et al., 2002; Capani et al., 2001; Shu et al., 2011; Martell et al.,2012; Kuipers et al.,2015]. Traditionally, quantum dots or fluorescent tags in combination with electron-dense colloidal gold or nanogold® have been used to localize proteins in conventional CLEM [Takizawa et al., 1998; Takizawa and Robinson, 2000; Nisman et al., 2004; Giepmans et al., 2005]. Applied as secondary antibodies, these tags can either be used before or after embedding the sample in resin. Unfortunately, epitope accessibility in these conventional methods is hindered by the large sizes of colloidal gold and quantum dots. Their smaller counterpart, FluoroNanogold™, has better penetration but requires gold enhancement to be identified in EM micrographs. Thus, the classical diaminobenzidine (DAB) -oxidation reaction using either immunolabeled eosin or recently developed, genetically expressed markers such as mini Singlet Oxygen Generator (miniSOG), FLIPPER and APEX, has proven to be a groundbreaking alternative [Deerinck et al., 1994; Capani et al., 2001; Shu et al., 2011; Martell et al.,2012; Kuipers et al.,2015]. The fluorescence of the label itself or its associated fusion protein is used to localize the target at the LM

level. The enzyme- or light-driven oxidation of DAB by the label creates an insoluble precipitate on the target, which generates molecular-specific EM contrast upon reaction with osmium

Post-embedment CLEM techniques offer two strategies for fluorescent labeling: *en bloc* labeling followed by resin embedment, or immunolabeling of ultrathin sections after resin embedding. Nanguneri and colleagues were the first to combine super resolution LM with array tomography [Nanguneri et al., 2012]. A series of ultra-thin resin sections were immunolabeled and imaged first by STORM and then by SEM. All individual 2D images were then correlated, aligned, and appended to a 3D volumetric stack to yield 3D CLEM data. Although this technique allows for the collection of 3D CLEM data from deep within tissue samples, it is limited by the availability of antibody epitopes on the surface of the section. En bloc labeling methods, which have been extensively pursued in part because of the cumulative interest in developing super-resolution CLEM, required the refinement of EM resin-embedment techniques to ensure the survival of selective genetically encoded fluorescent proteins, as well as chemical fluorophores [Watanabe et al., 2011; Watanabe et al., 2014; Perkovic et al., 2014; Kim et al., Johnson et al., 2015]. Since stochastic super-resolution techniques rely on the photoactivation or photoswitching abilities of dyes, protocols had to be adapted so that dyes were still capable of switching post-EM processing and embedment. Embedment techniques with very low concentrations of heavy metals were developed to ensure the survival of genetically encoded fluorescent proteins, such as GFP, as well as some synthetic fluorophores [Watanabe et al., 2011; Watanabe et al., 2014; Perkovic et al., 2014; Kim et al., 2015; Johnson et al., 2015]. The successful preservation of

photoactivatable tdEos fluorescence post-EM processing drove the development of multiple strategies to correlate PALM data with various EM modalities [Watanabe et al., 2011; Watanabe et al., 2014]. Coleman and coworkers were the first to demonstrate that Alexa Fluor® dyes retained their fluorescence and antigenicity following osmium treatment [Coleman et al., 2006]. Alexa Fluor® 647 (Alexa 647) has been proven to tolerate high concentrations of uranyl acetate at low temperatures as well as low concentrations of osmium tetroxide [Perkovic et al., 2014; Kim et al., 2015]. An extensive study by Kim and colleagues further demonstrated that Alexa 647 could tolerate low concentrations of a diversity of heavy metal EM cocktails as well as embedment in a variety of resins, making it an ideal candidate for post-embedment correlated STORM-EM approaches [Kim et al., 2015]. In this chapter, I exclusively describe my extended applications of correlated STORM-EM using the Alexa 647 dye and several 2D and 3D EM technologies, driven by the goal of determining the distribution of ion channels and transporters governing cardiac E-C coupling in mammalian ventricular myocytes.

2.3. Methods

2.3.1. Preparation of cells and tissue

The animal procedures followed in this study were approved by the University of California San Diego Institutional Animal Care and Use Committee. For isolated cell CLEM processing, ventricular cardiomyocytes were isolated from adult (6-8 month old) mice and neonatal (1-3 days) rats by collagenase perfusion-digestion as described previously [Zhou et al., 2000]. Cells were plated on laminin-coated glass bottom culture dishes (P35G-0-14-C, MatTek

Corp.) for 2 hours to allow the cells to settle and attach to the glass. Once attached, the cells were fixed in 4% (wt/v) paraformaldehyde in PBS for 30 min on ice. For tissue CLEM processing, adult (6-8 month old) mice were euthanized and perfusion-fixed with 4% paraformaldehyde in 0.15M cacodylate buffer (pH 7.4). 40-50 um sections were obtained from the free wall of the left ventricles using a vibrating blade microtome (VT 1000S, Leica, Germany). Sections were post-fixed overnight (ON) in 4% paraformaldehyde in 0.15M cacodylate buffer (pH 7.4) on ice.

2.3.2. Immunohistochemistry

Fixed, isolated cells were rinsed in PBS (5x3 min) and blocked in blocking buffer (PBS containing 3% bovine serum albumin, 50 mM glycine and 0.1% Triton X100 (Sigma, St. Louis, MO)) for 20 min on ice. The adult mouse cardiomyocytes (AMCM) were incubated in mouse monoclonal anti-RyR primary antibody (MA3-925,Thermo Scientific, 1:200) for 1 hr at RT, and the neonatal rat ventricular myocytes (NRVM) were incubated in mouse monoclonal alpha-actinin primary antibody (ab9465,Abcam, 1:200) and washed with PBS 5x3mins, followed by incubation with highly cross-adsorbed Alexa 647-labeled goat anti-mouse IgG antibody (A-21236, Invitrogen, 1:200) for 1 hr at RT and finally washed again with PBS (5x3 min). Similarly, tissue sections were rinsed in PBS (8x5 min), blocked in blocking buffer (PBS containing 3% normal goat serum, 1% bovine serum albumin, 1% cold water fish gelatin and 0.1% Triton X-100) for 30 mins on ice on a rocker and incubated in rabbit polyclonal anti-RyR2 antibody (HPA016697, Sigma-Aldrich, 1:50) for 1 hr RT. The tissue sections were washed with working buffer (10x diluted blocking buffer, 8x5 min) followed by incubation

in highly cross-adsorbed Alexa 647-labeled goat anti-rabbit IgG antibody (A-21245, Invitrogen, 1:200) for 1 hr RT and finally washed with working buffer (8x5 min). All antibody dilutions were performed in 10x diluted blocking buffer.

2.3.3. Electron microscopy specimen preparation

The following steps were all performed in the dark to avoid fluorescence loss. Cells and tissue sections were post-fixed in 0.1% glutaraldehyde in PBS (pH 6.8) for 5 min RT on ice and then rinsed in PBS (5x3 min). The fixed cells and tissues were further incubated in 0.5% osmium tetroxide in distilled water for 10 mins on ice. For improved membrane contrast, a reduced osmium cocktail was used for the tissue sections (0.5% osmium tetroxide and 1.5% potassium ferricyanide in water). The samples were then rinsed with distilled water (5x3 min), followed by dehydration in a cold graded ethanol series (20%, 50%, 70% - 3 min each for cells and 7 min each for tissue sections) and then stained *en bloc* with 2% uranyl acetate (Ted Pella Inc.) in 70% ethanol for 20 min on ice. The samples were rinsed with chilled 70% ethanol (5x1 min) until no uranyl acetate residue was left, and the cold graded ethanol washes were continued (90%, 100%, 100%). This was followed by a single rinse in room temperature anhydrous ethanol and infiltration with Durcupan ACM resin (Electron Microscopy Sciences,PA) as described for cells in (Shu et al., 2011) and tissue in (Perkins et al., 1997).

2.3.4. Sectioning

For STORM followed by SEM imaging, 80 nm thick sections were collected and transferred onto glow discharged, indium tin oxide coated

coverslips (ITO) (06468-AB, Structure Probe Inc supplies). The coverslips were placed on a hot plate (40-50C) to allow the sections to dry and stretch. For array tomography, four serial 80 nm sections were collected per coverslip. For STORM followed by TEM, 250 nm sections were collected on grids.

2.3.5. Tetraspeck™ beads for correlation

To allow for correlation between the STORM and SEM images, 0.1-μm diameter TetraSpeck™ fluorescent microspheres (T-7279, Invitrogen, 1:100 in PBS) were applied directly to the sections on the coverslips for 30 s. The solution was blown off and a fresh drop of 1:100 dilution microspheres were then applied again for 30 s. For STORM followed by TEM, the grid was first dipped into the microsphere solution until the grid was coated with the solution and then allowed to dry. To properly act as fiducial markers for correlation, a minimum of three beads surrounding the ROI are required.

2.3.6. STORM imaging

The STORM imaging platform used consisted of a Nikon TE2000-U with a modified single objective lens holder for a TIRF objective lens (Nikon Apo TIRF 60x 1.49 or Nikon Plan Apo TIRF 60x 1.45), with a custom 500 mm tube lens to achieve 107 nm/pixel. A 637 nm laser (Coherent OBIS 637nm LX 140mW) is focused at the back focal plane of the objective lens to achieve collimated illumination. A linear stage (Thorlabs) moves the lens and routing mirror to move the focused laser spot at the conjugated plane of the back focal of the objective lens to control the illumination incident angle through a computer. A modified version of the ASI CRIFF system with a piezo Z stage was used to compensate

for focus drift by monitoring the TIRF illumination return beam. A Chroma TRF49913 filter set without excitation filter was used for splitting the excitation laser and fluorescence. A back-illuminated EMCCD (Andor iXon 897) and Andor Solios were used to capture the images.

All STORM imaging was performed in an imaging buffer optimized for the Alexa 647 dye as described in (Dempsey et al., 2011). It contains 50 mM Tris (pH 8.0), 10 mM NaCl, 10% (w/v) glucose, 143 mM 2-Mercaptoethanol (β -ME) and an oxygen scavenging system (0.5mg/ml glucose oxidase (G2133-10KU, Sigma-Aldrich) and 40ug/ml catalase (C100-50MG, Sigma-Aldrich). Reusable CultureWell gaskets (103210, Grace Bio-Labs) were used to create a well around the section for the imaging buffer and were sealed with a glass slide on the other side. To allow for imaging, the grids were sandwiched between a glass coverslip and slide in the imaging media using Reusable CultureWell gaskets. A series of ~15,000 raw frames (50 ms/frame) was captured for each ROI. Multiple ROIs could be imaged from the same section. Once STORM imaging was complete, sections on the ITO and grid were washed with PBS once followed by multiple washes with double distilled water (5x3 min) to remove any imaging media residue. The solution from the last wash was blown off the section to prevent any precipitates from drying onto the section.

2.3.7. Electron microscopy

2.3.7.1. Scanning electron microscopy

Sections on the ITO coverslips were post-stained for 5 mins with Sato lead followed by multiple rinses with double distilled water (5x3 mins). As described earlier, the solution from the last wash was blown off the section to

prevent any precipitates from drying onto the section. The coverslip was further cleaned to ensure no oil residue was left behind from STORM imaging. The section was then imaged using the MERLIN Variable Pressure (VP) Compact and MERLIN field emission SEM (Carl Zeiss Microscopy, Jena, Germany) fitted with a 3View unit (Gatan Inc, Pleasanton, CA, USA). Using a 3View back-scatter detector, SEM images of the ROIs were collected at an accelerating voltage of 2 kV, with a raster size of 20k x 20k and pixel dwell time of 1.0 µs at a working distance of 4.5-5mm (Fig. 2.1). Both low and high magnification images of the ROI were collected for correlation using Tetraspeck™ beads.

2.3.7.2. EM tomography

The grid was glow discharged, and colloidal gold particles (5 and 10 nm in diameter) were deposited on each side to serve as fiducial markers for reconstruction. The section was imaged using an FEI Titan microscope operating at 300 kV using a 4k x 4k Gatan CCD camera. First, a zero-tilt mosaic of the section was collected for correlation purposes and to identify the ROI previously imaged using STORM. For tomographic reconstruction, quadruple tilt series of images were recorded from -60 to +60 at 0.5 degree increments for contrast enhancement as described in [Ellisman et al., 2014]. Datasets were reconstructed using transform based tracking, and automated alignment procedures as well as iterative (weighted SIRT) Methods [Ellisman et al., 2014; Phan et al., 2012]. Reconstructed volumes were viewed, and objects of interest were manually traced and reconstructed into surface meshes using the IMOD suite (Boulder Laboratory for 3D Electron Microscopy of Cells, University of Colorado, Boulder, CO) (Kremer et al., 1996).

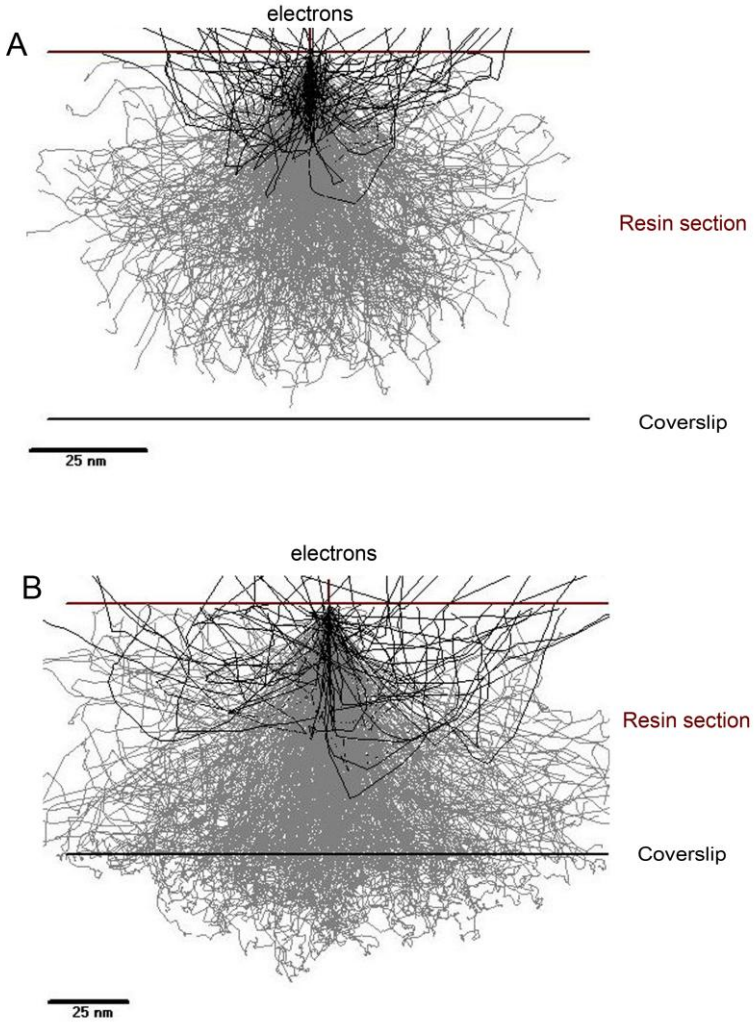

Figure 2.1. : SEM simulation of imaging 80nm thin sections at 2kV (A) and 3kV (B). Higher voltages cannot be used for improved contrast during imaging since the electrons pass right through the sample instead of generating BSE's at the surface of the section.

2.3.8. LM-EM correlation and alignment

To correlate the STORM images with SEM images, fluorescent Tetraspeck™ beads were identified and their centroids determined in the STORM images and corresponding SEM images. Using an automated Python script, affine transformations were applied to the STORM data and then scaled and correlatively overlaid onto the SEM using ImageJ [Schneider et al., 2012].

To correlate the STORM images with the tomographic volumes, the STORM image was first aligned to a low magnification zero-tilt mosaic of the ROI using Tetraspeck™ beads. Next, using the 5 and 10 nm gold as fiducial markers, the zero-tilt mosaic was aligned to the tomographic reconstruction. Lastly the correlative transformation from the Tetraspeck™ bead alignment and the gold alignment were combined and applied to the original STORM image to correlate it to the tomogram.

For array tomography, STORM data was aligned to SEM images using Tetraspeck™ beads as described above. Consecutive SEM sections were aligned to each other using patch cross-correlation methods. The same transformations were applied to consecutive STORM data as well.

2.4. Results

2.4.1. Sample preparation for correlated imaging

To determine the localization of E-C coupling molecules such as RyRs in native ventricular cells and tissues collected from mice, we adapted a sample preparation strategy used in cultured cells by Kim and colleagues for correlated STORM and scanning SEM (Fig. 2.2). Since cardiomyocytes are known to exhibit high levels of autofluorescence in response to 488 nm and 568 nm

excitation, Alexa 647 is an ideal choice for labeling their protein targets [Chorvat et al., 2004]. Traditional immunolabeling methods using a primary antibody followed by a secondary Alexa Fluor 647 antibody are optimal for the pre-embedment labeling of proteins.

However, detergents that are used to perforate the cell membrane for antibody delivery damage cellular ultrastructure. Thus, to achieve EM-grade ultrastructure with efficient antibody penetration, different detergents and immunolabeling conditions were tested. An immunolabeling protocol using very low concentrations of Triton X-100 on ice was determined to yield the best structural integrity. Antibody incubations were performed overnight at 4C or in 1 hr at room temperature, with the latter being preferable due to the reversible nature of paraformaldehyde fixation. We observed significant, non-specific mouse IgG staining in in the plasma membrane of tissue vs. in isolated cells (Fig. 2.3). As a result, the isolated cells were treated with a monoclonal anti-RyR antibody whereas the tissue samples were incubated in a rabbit polyclonal anti-RyR antibody for RyR labeling. Following immunolabeling, the sample was further post-fixed with 0.1% glutaraldehyde for 5 mins on ice to aid in ultrastructural preservation. Although fixation with glutaraldehyde prior to immunolabeling would achieve better ultrastructure, it is known that this step interferes with antibody labeling; thus, glutaraldehyde was used exclusively as a post-fix [Priestley, 1984]. Membranes were further post-fixed using low concentrations of 0.5% osmium tetroxide for 10 mins on ice to enhance the stabilization of membrane structures. However, as seen in Fig. 2.4 the resulting EM contrast following this step was still low. Thus, potassium ferricyanide-reduced osmium tetroxide was used to improve contrast for membranous

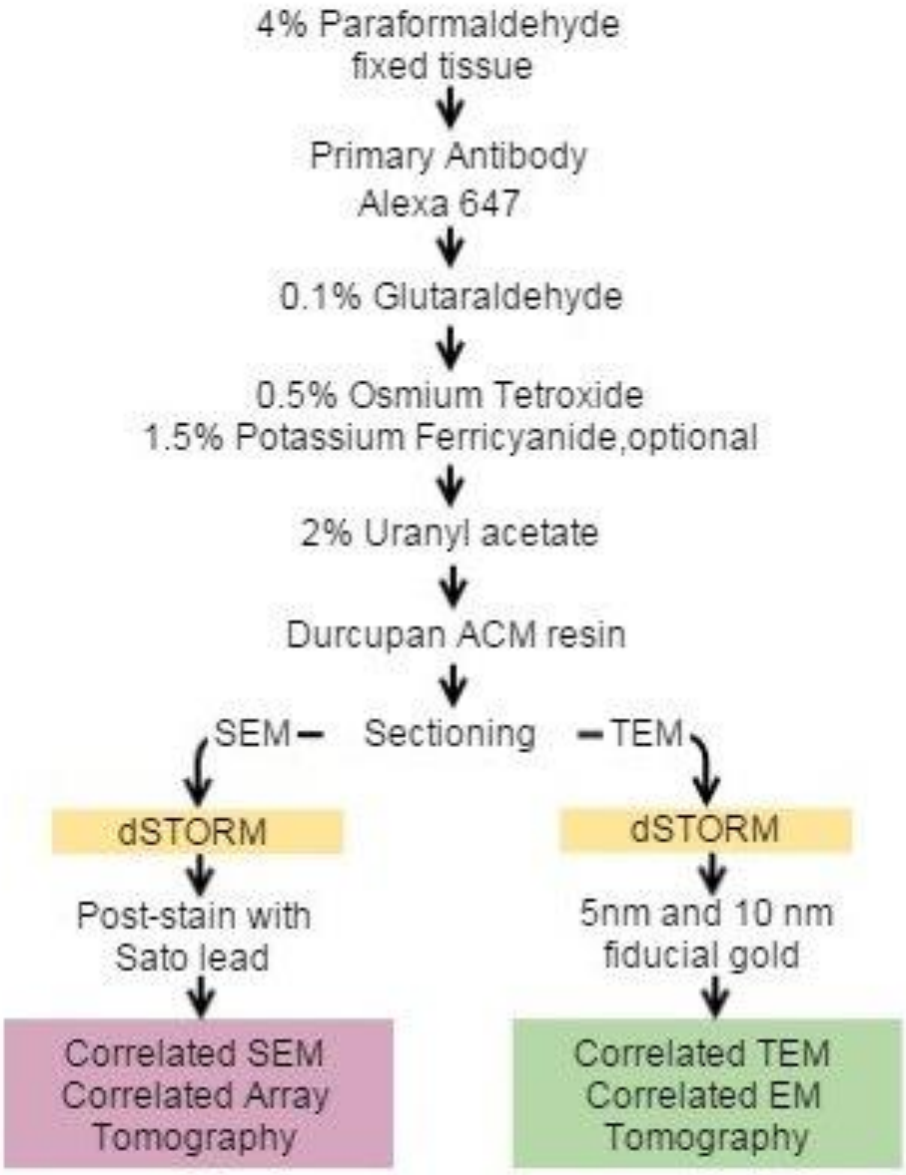

Figure 2.2. : Correlated in-resin STORM and EM. Schematic overview of the sample preparation and imaging for in-resin correlated STORM -EM. The same specimen preparation is used for both correlated SEM and TEM.

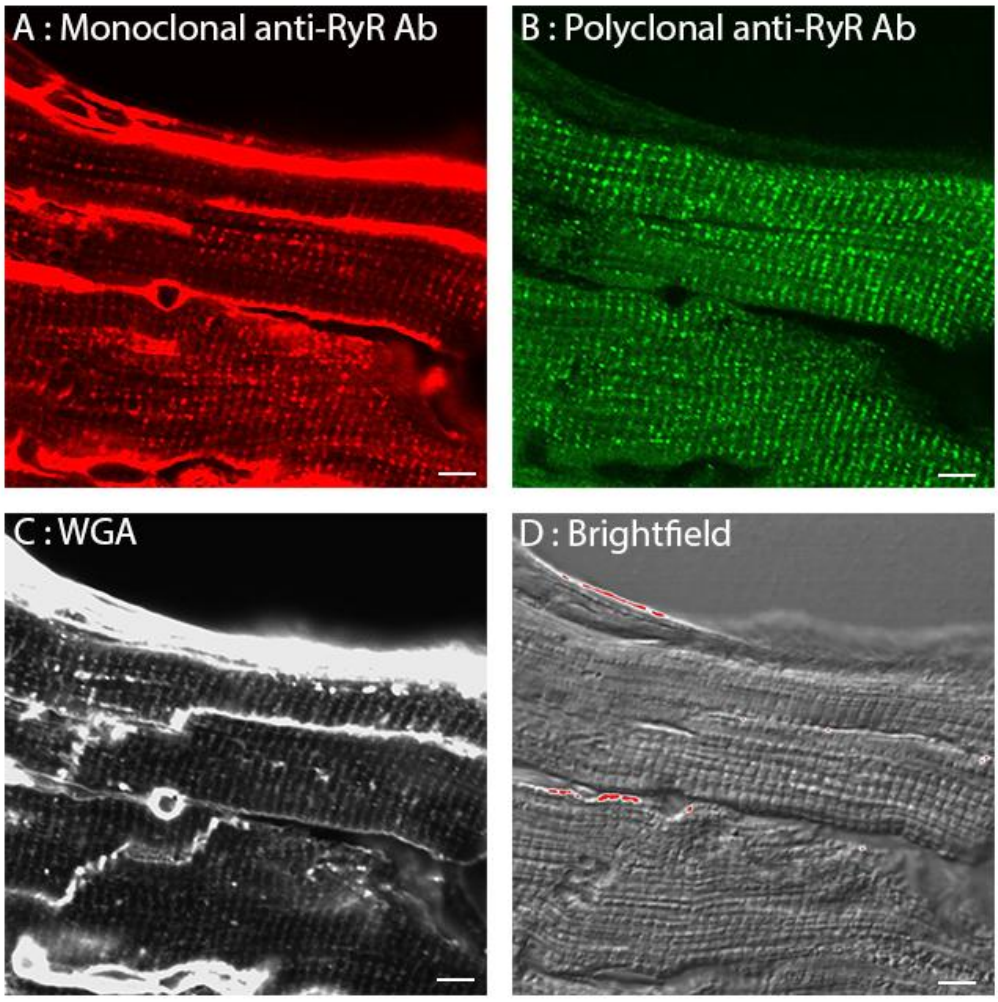

Figure 2.3. : Comparison of anti-RyR antibodies for RyR labeling in mouse tissue. Monoclonal mouse anti-RyR in mouse tissue (A) demonstrated high level of non-specific fluorescence in the extra-cellular space and sarcolemma when compared to polyclonal rabbit anti-RyR antibody labeling (B). Wheat germ agglutinin (WGA) (C) labeling of sarcolemma and brightfield image (D) of the tissue have been included for reference. Scale bars 5um.

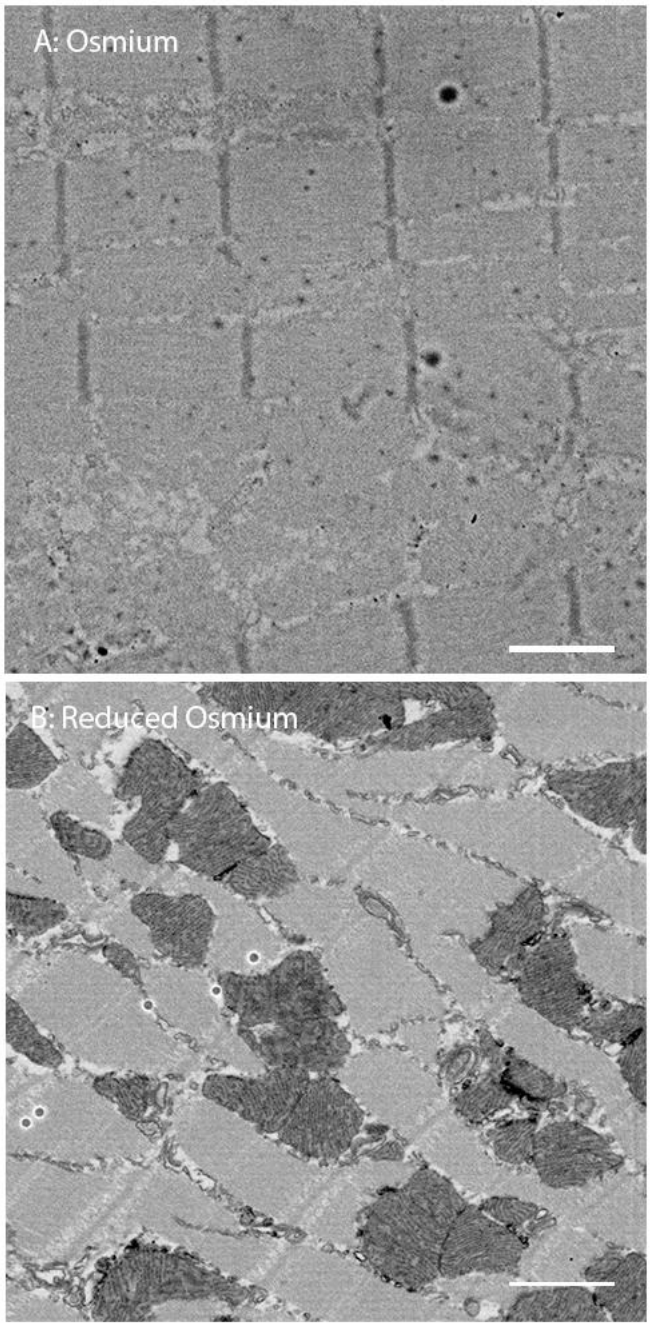

Figure 2.4. : Comparison of using osmium only (A) vs. reduced osmium (B) for EM staining. The reduced osmium (B) samples have significantly improved membrane contrast than the osmium only (A) treated samples.

organelles such as the SR [Karnovsky, 1971]. The use of this reagent, however, resulted in the loss of ~6% of the total fluorescence, corroborating what was previously described [Kim et al., 2015]. Uranyl acetate was introduced in ethanol during the dehydration steps to serve as a metallic stain. Though both LR white and Durcupan ACM demonstrated good fluorophore preservation, we chose to continue working with Durcupan due to the ease of embedding with this resin. Depending upon the EM modality chosen, the embedded samples were sectioned into either 80 nm thin or 250 nm thick sections, and were then ready for dSTORM followed by EM imaging. Fig. 2.5 confirms that dSTORM imaging of the labeled protein was reproducible before and after embedment. As expected, the photon counts were lower after embedment, resulting in localization accuracies of ~25 nm (Fig. 2.6).

2.4.2. Computational LM-EM image correlation

The precision with which LM images are correlated with EM images determines the accuracy with which labeled proteins can be localized on EM maps of cellular ultrastructure. TetraSpeck™ fluorescent microspheres were applied to resin sections and were subsequently used as fiducial markers for the landmark-based registration of LM and EM images. Since the sample may become distorted while in solution during dSTORM imaging and electron beam irradiation may induce shrinkage, image registration was achieved using affine transformations that include shearing, scaling, and rotational transforms. Sebastien Phan (NCMIR) implemented an automated Python script for correlation into the “NAVminator”, a software package developed with my data as a user case (Fig. 2.7.). The accuracy of correlation was verified by excluding one

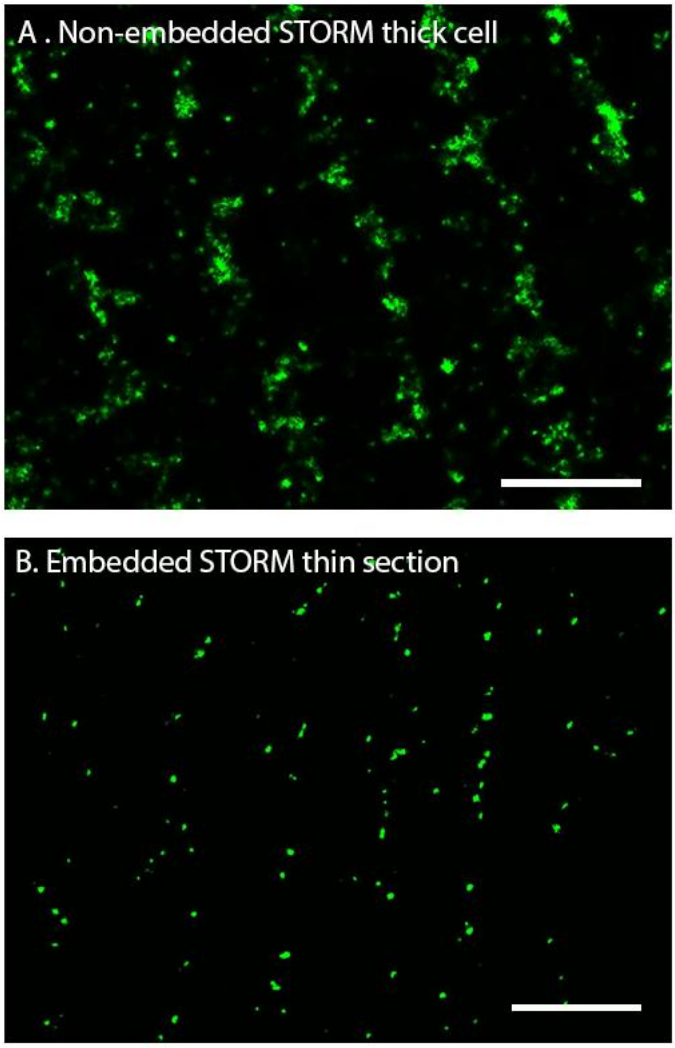

Figure 2.5. : STORM imaging of immunolabeled RyR in a non-embedded sample (A) vs. embedded sample (B). Both images (A, B) demonstrate striated-pattern labeling typical to immunofluorescent RyR diffraction-limited images. Since an 80nm thin section of the cell was imaged in [B] the striations have sparser clusters than the thick cell imaged in [A].

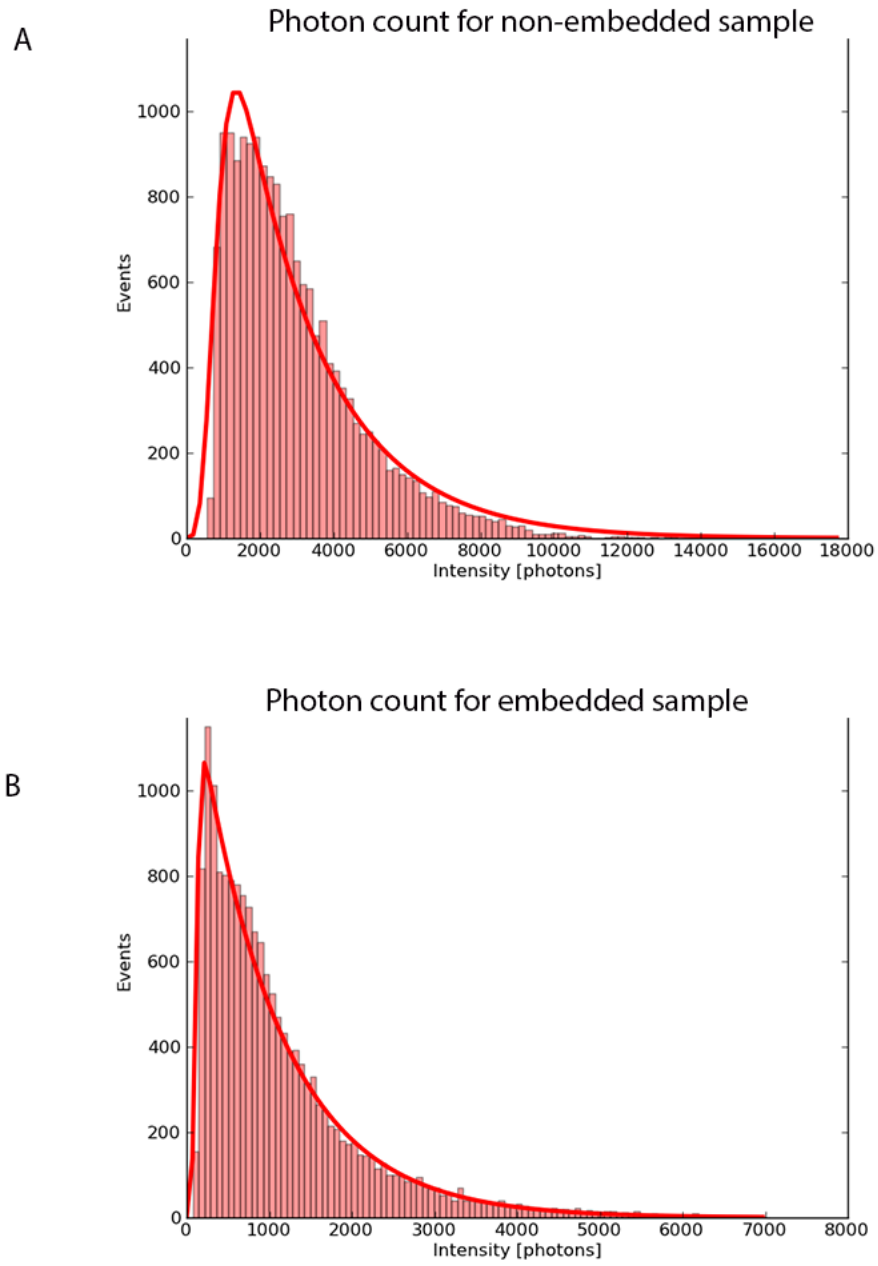

Figure 2.6. : A comparison of photon counts of STORM data collected from non-embedded samples (A) vs. embedded samples (B). As expected fluorescence photon yield is reduced in embedded samples (B) when compared to non-resin-embedded samples (A). However, the photon yield is high enough to achieve localization accuracies of ~25nm in the embedded samples.

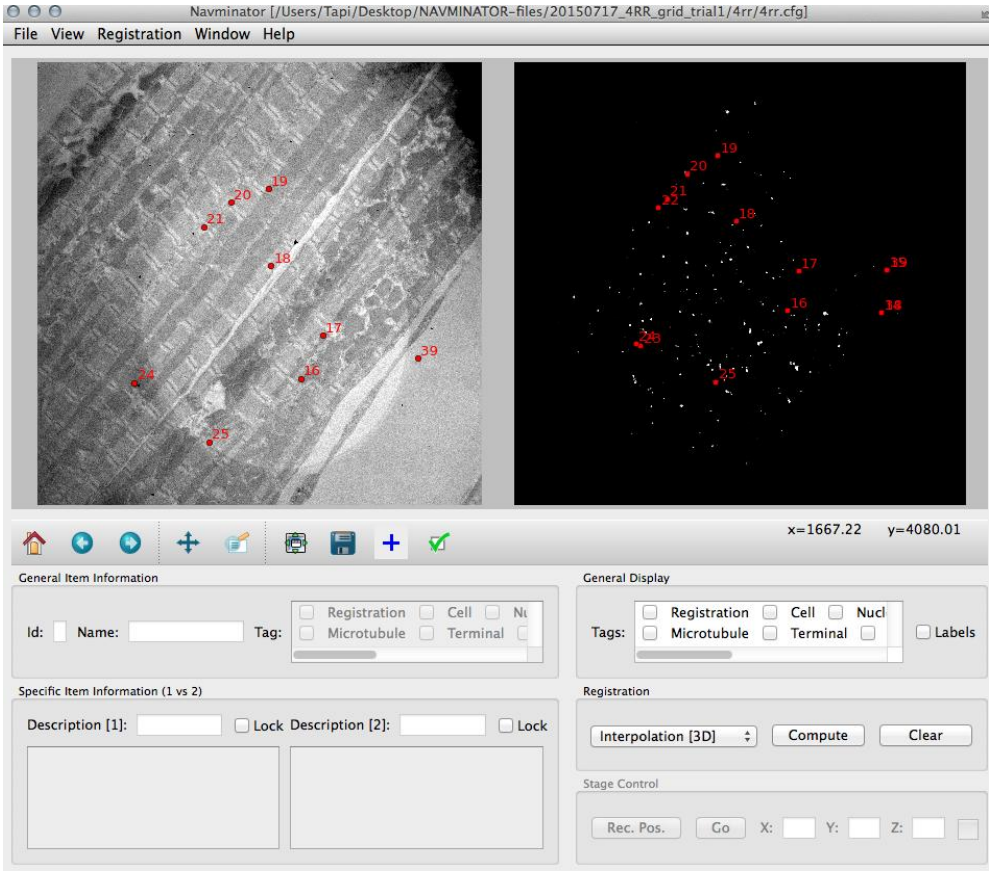

Figure 2.7. : Screenshot of NAVMINATOR. Software used for correlation of LM and EM images. The fluorescent fiducial makers are identified with numbered red markers in the EM and LM image and processed for correlation using affine transformations.

bead from the calculation of the transform. The predicted position of this bead was then compared with the actual bead in the EM images to determine the error of the correlation.

2.4.3. 2D Correlated in-resin STORM and EM

To image the distribution of proteins throughout the cell, we chose to correlate dSTORM data with SEM and TEM images because of the larger field of view afforded by these instruments. Thin, 80 nm sections of embedded cardiomyocytes/tissue were collected onto ITO coverslips for SEM and onto grids for TEM. Following dSTORM imaging, the sections were post-stained with lead and imaged in a MERLIN field emission SEM with a Gatan 3View backscatter detector. Fig 2.8 and 2.9 show correlated STORM and SEM data of samples processed using osmium only. The alpha-actinin striations coincide with the Z-lines in the NRVM as expected (Fig. 2.8). Correlated images in Fig. 2.9 show clear localization of RyRs at Z-lines in AMCM, as expected. Despite low contrast, t-tubules were identified at the Z-lines and were adjacent to correlated RyR signal. However, membranes such as the SR and mitochondrial cristae still could not be clearly discerned in these images. As a result, despite the loss of fluorescence, osmium was replaced with potassium ferricyanide-reduced osmium to improve the preservation and contrast of membranes.

As seen in Fig. 2.10, STORM imaging of immunolabeled RyRs in-resin sections demonstrated punctate labeling of RyR clusters consistent with previous studies [Baddeley et al., 2009;Hou et al., 2015]. The frequency of RyR clusters was lower since they were collected in only 80-250 nm thick resin sections.

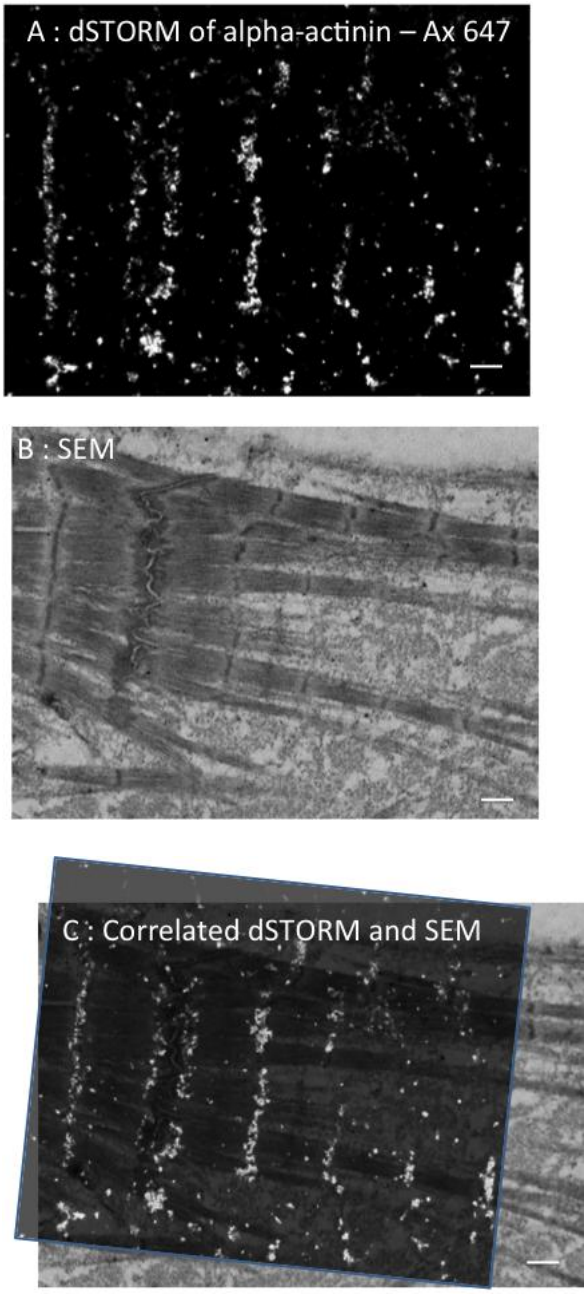

Figure 2.8. : Correlated in-resin STORM and SEM of immunolabeled alpha-actinin in NRVM with osmium: 80nm thin durcupan sections were first imaged using STORM (A) followed by post staining and imaged using SEM (B). (C) is the correlated image of alpha-actinin STORM data with SEM data. As expected, alpha-actinin is localized at the Z-lines. Scale Bars 1um.

Figure 2.9. : Correlated in-resin STORM and SEM of immunolabeled RyR receptor with in AMCMs processed with osmium. The ROI is located using diffraction limited microscopy (A) followed by subsequent dSTORM imaging (B). The section is post stained and the same ROI is imaged using SEM at low magnification (C) and high magnification (E). 100nm Tetraspeck™ beads identified with white circles in (A, B, C) are used to correlate the dSTORM image with SEM at low (D) and high magnification (E). RyR clusters (green) can be identified adjacent to the contoured T-tubule membrane (yellow) at Z-lines (E). Scale Bars 2um (A, B, C, D), 0.5um (E).

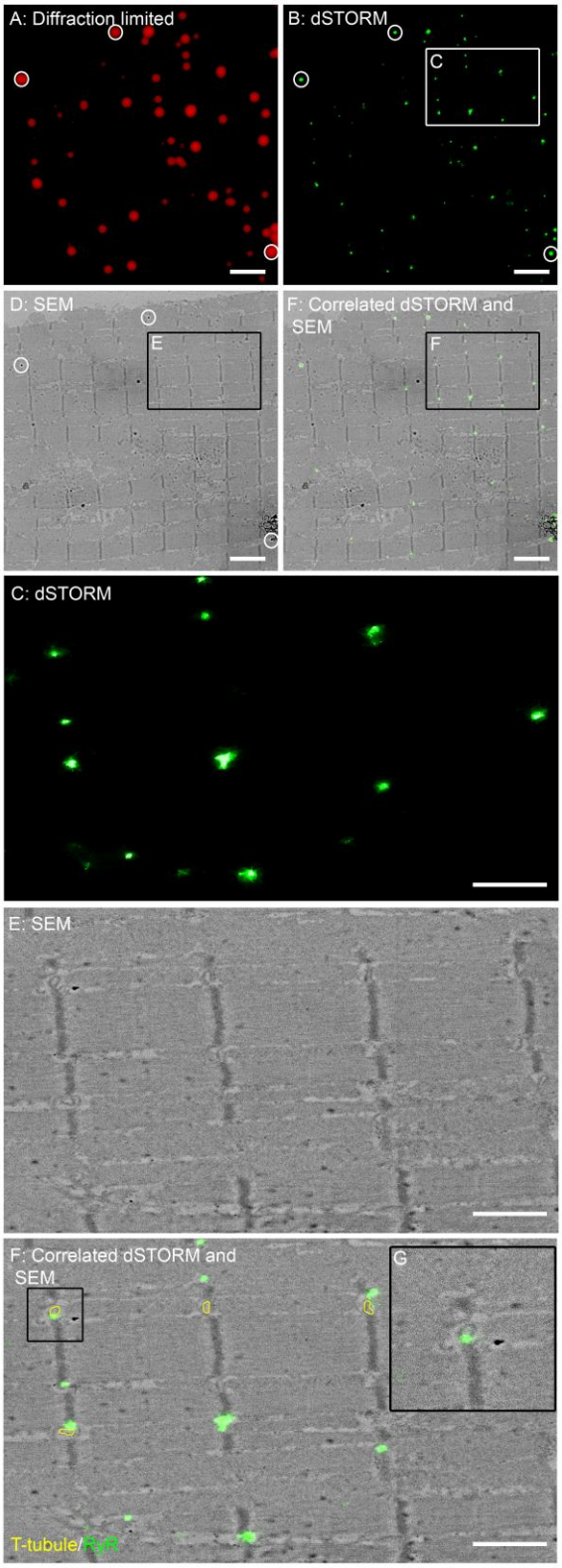
A: Diffraction limited
B: dSTORM
C
D: SEM
E
F: Correlated dSTORM and SEM
F
C: dSTORM
E: SEM
F: Correlated dSTORM and SEM
G
T-tubule/RyR

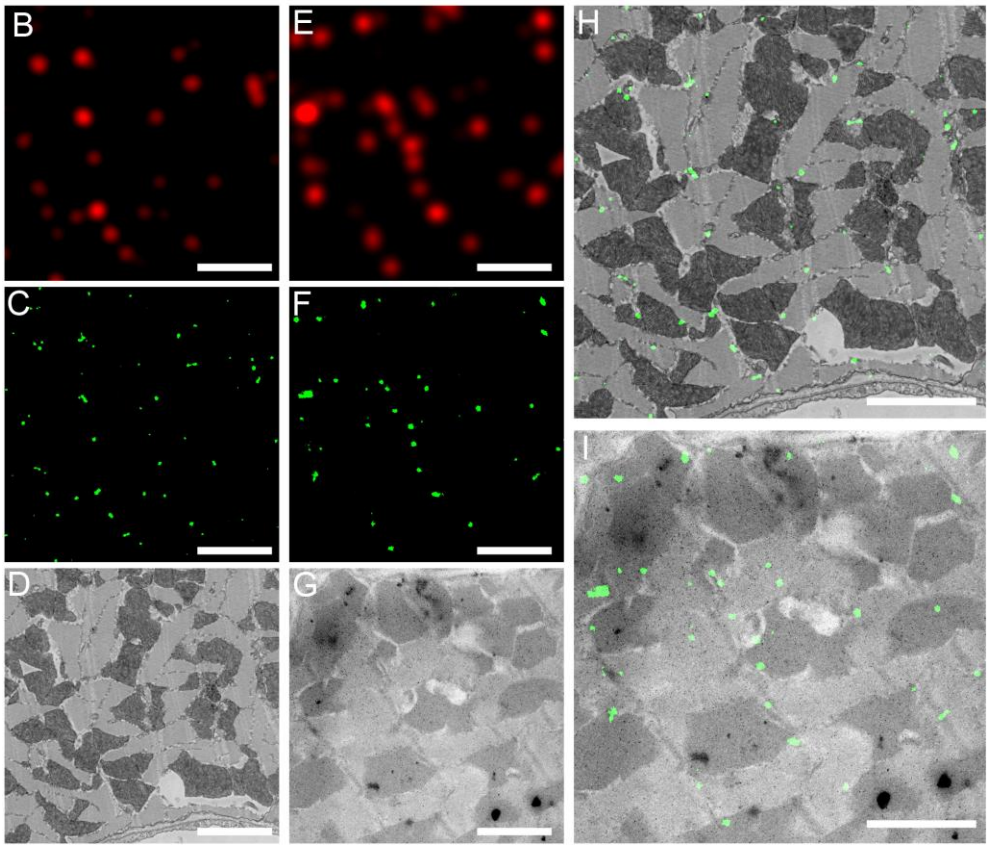

Figure 2.10. : Correlated in-resin STORM and EM of RyR –Ax 647 in mouse tissue with reduced osmium. The same specimen preparation is used for both correlated SEM (B, C, D, H) and TEM (E, F, G, I). The ROI is located using diffraction limited microscopy (B, E) followed by subsequent STORM imaging (C, F). Next, the same area is imaged using either SEM (D) or TEM (G) and correlated with the STORM data using 100nm Tetraspeck™ beads in (H) and (I) respectively. Correlated RyR clusters are identified on the SR.In the interior of the cell they are localized at the Z-lines. Scale Bars 2um (B, C, D, E, F, G, H, I).

Correlating STORM images with an SEM image (Fig. 2.10H) acquired from a 80 nm thin resin section as well as a TEM image (Fig. 2.10I) acquired from a 250 nm thick section showed the clear localization of RyRs on the SR membrane throughout the cardiomyocytes in the tissue. RyR clusters were observed in close association with the surface sarcolemma along the edge of the cell and at the Z-lines in the interior of the cell. Note that the TEM image in Fig. 2.10 is the projection of a 250 nm section onto a 2D plane, which resulted in poorer axial resolution than the 80 nm SEM image. The EM image resolutions are comparable when 80 nm thin sections are imaged by both modalities.

2.4.4. 3D Correlated in-resin STORM and EM

2.4.4.1. Correlated array tomography

Although the 2D methods described above have furthered our understanding of the molecular composition of the E-C coupling sites, cells and tissues are 3D objects. There is a limit to the 3D information that can be extracted from 2D views. Thus, there is a need for 3D CLEM techniques to study protein localization within sub-cellular membrane volumes at nanometer-scale resolution**.** One such 3D CLEM strategy is array tomography. Serial 80 nm sections were imaged using STORM followed by SEM. After LM-EM correlation, consecutive sections were aligned by patch cross-correlation to generate 3D CLEM volumes. Representative slices of one such volume are shown in Fig. 2.11.

2.4.4.2. Correlated STORM and EM tomography

The large field of view offered by STORM-SEM images facilitates the cell-wide identification and location of RyRs. However, the axial resolution of SEM

images is restricted to the thickness of the resin sections and the depth of primary excitations. Thus, we applied EM tomography following STORM imaging to correlate RyR localizations with 3D sub-cellular structures at nanometer scale resolutions. For correlated STORM and EM tomography, resin samples were sectioned into 250 nm thick sections and mounted onto a clamp grid, which was then sandwiched between a cover glass and coverslip in imaging media for dSTORM imaging. The grid was then washed and dried, and gold fiducials were added for EM tomography. To compensate for the weak resin section staining used in the current study to preserve Alexa 647 fluorescence, quadruple tilt series were recorded, and tomograms were reconstructed using transform-based tracking and automated alignment procedures as well as iterative (weighted SIRT) methods as described previously [Ellisman et al., 2014; Phan et al., 2012]. By sampling the region of interest through multiple orientations, an averaging-like strategy can be introduced, reducing sampling artifacts and producing higher quality tomograms.

In the correlated images of fluorescently labeled RyR STORM data overlaid onto zero-tilt EM mosaic micrographs, we observed that RyR labeling is localized primarily at the Z-lines in ventricular myocytes and tissue (Fig. 2.12 and Fig. 2.13). Fig 2.12E shows the fluorescence data superimposed onto an EM tomogram slice of an AMCM. The T-tubule membrane was segmented in the tomogram to generate a 3D surface mesh model of the T-tubule (yellow) onto which the rendered dSTORM data were superimposed to show that fluorescently labeled RyR (green) are found to be localized adjacent to T-tubules at the Z-lines

Figure 2.11. : Correlated in-resin STORM and array tomography of immunolabeled RyR receptor in mouse tissue with reduced osmium. 4 consecutive 80nm thin sections are imaged using STORM followed by SEM and correlated (A, B, C, D). Using patch cross-correlation, the consecutive correlated sections are aligned into a 3D volume creating a 3D CLEM volume. Correlated RyR (green) fluorescence can be identified in consecutive sections on the SR. This data is further analyzed in chapter 3. Scale Bars 2um (A, B, C, D).

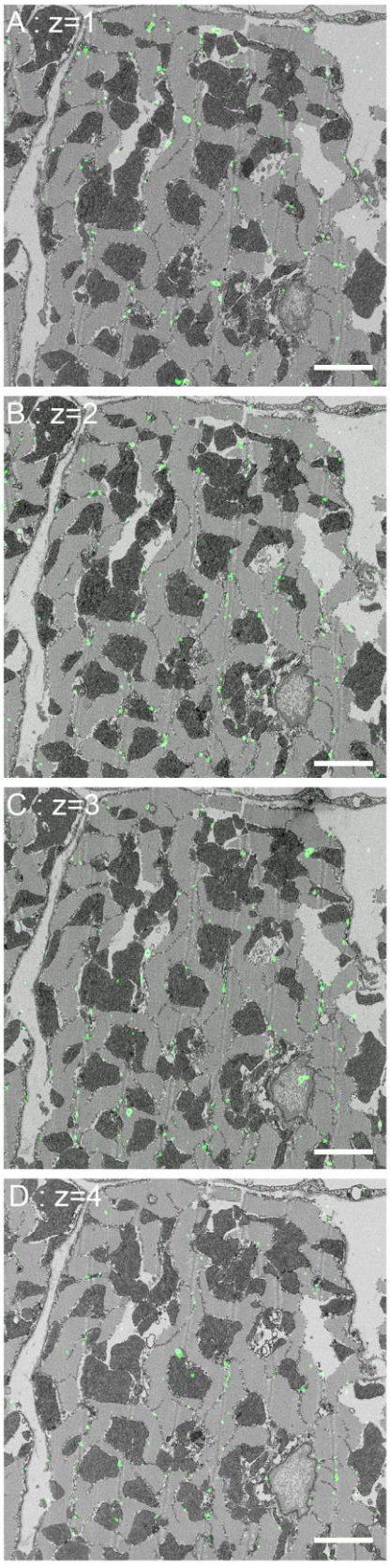
A : z=1
B : z=2
C : z=3
D : z=4

Figure 2.12. : Correlated in-resin STORM and EM tomography of immunolabeled RyR receptor in AMCMs with osmium. The ROI is located using diffraction limited microscopy (A) followed by subsequent STORM imaging (B). The same section is imaged at 0 tilt using a TEM at low magnification (C). The cell nucleus and plasma membrane have been roughly identified in pink (C, D). 100nm Tetraspeck™ beads identified with white circles in (A, B, C) are used to correlate the STORM image with the low magnification TEM micrograph (D). Regions containing RyR fluorescence are imaged for EM tomography. RyR clusters (green) can be identified adjacent to the T-tubule membrane at Z-lines identified in individual sections from the electron tomogram (E). The boxed T-tubule in (E) is segmented in the tomogram and a surface mesh model (yellow) for the T-tubule is generated (F). The T-tubule model is shown in correlation with RyR fluorescence data (G) as well as the tomogram (H).Scale Bars 4um (A, B, C, D), 1um (E), 100 nm (F, G, H).

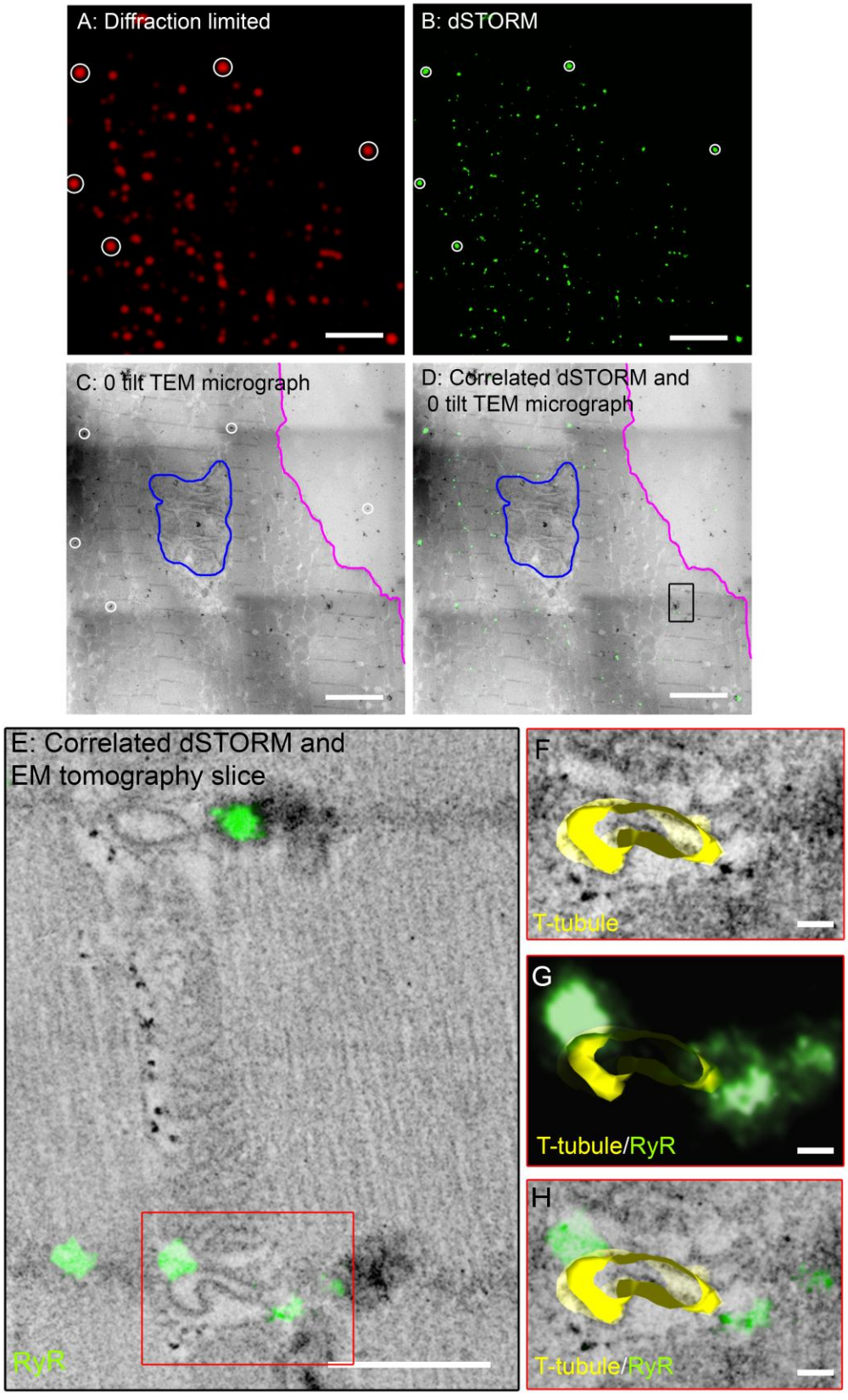
A: Diffraction limited
B: dSTORM
C: 0 tilt TEM micrograph
D: Correlated dSTORM and
0 tilt TEM micrograph
E: Correlated dSTORM and
EM tomography slice
RyR
F
T-tubule
G
T-tubule/RyR
H
T-tubule/RyR

Figure 2.13. : Correlated in-resin STORM and EM tomography of immunolabeled RyR receptor in mouse tissue with reduced osmium. The ROI is located using diffraction limited microscopy (A) followed by subsequent STORM imaging (B). The same section is imaged at 0 tilt using a TEM at low magnification (C). Tetraspeck™ beads are used to correlate the STORM image with the low magnification TEM micrograph (D). Regions containing RyR fluorescence are imaged for EM tomography (black boxed region). RyR clusters (green) can be identified on the SR membrane adjacent to the T-tubule membrane at Z-lines identified in individual sections from the electron tomogram (E). The boxed (red) dyadic space in (E) is segmented in the tomogram and a surface mesh model for the T-tubule (yellow) and jSR (blue) is generated (F). The model is shown in correlation with RyR fluorescence data (G) as well as a slice of the tomogram (H). The RyR fluorescence is observed to be localized within the dyadic cleft as well as outside the cleft. Scale Bars 4um (A, B, C, D), 2 um (E), 100 nm (F, G, H).

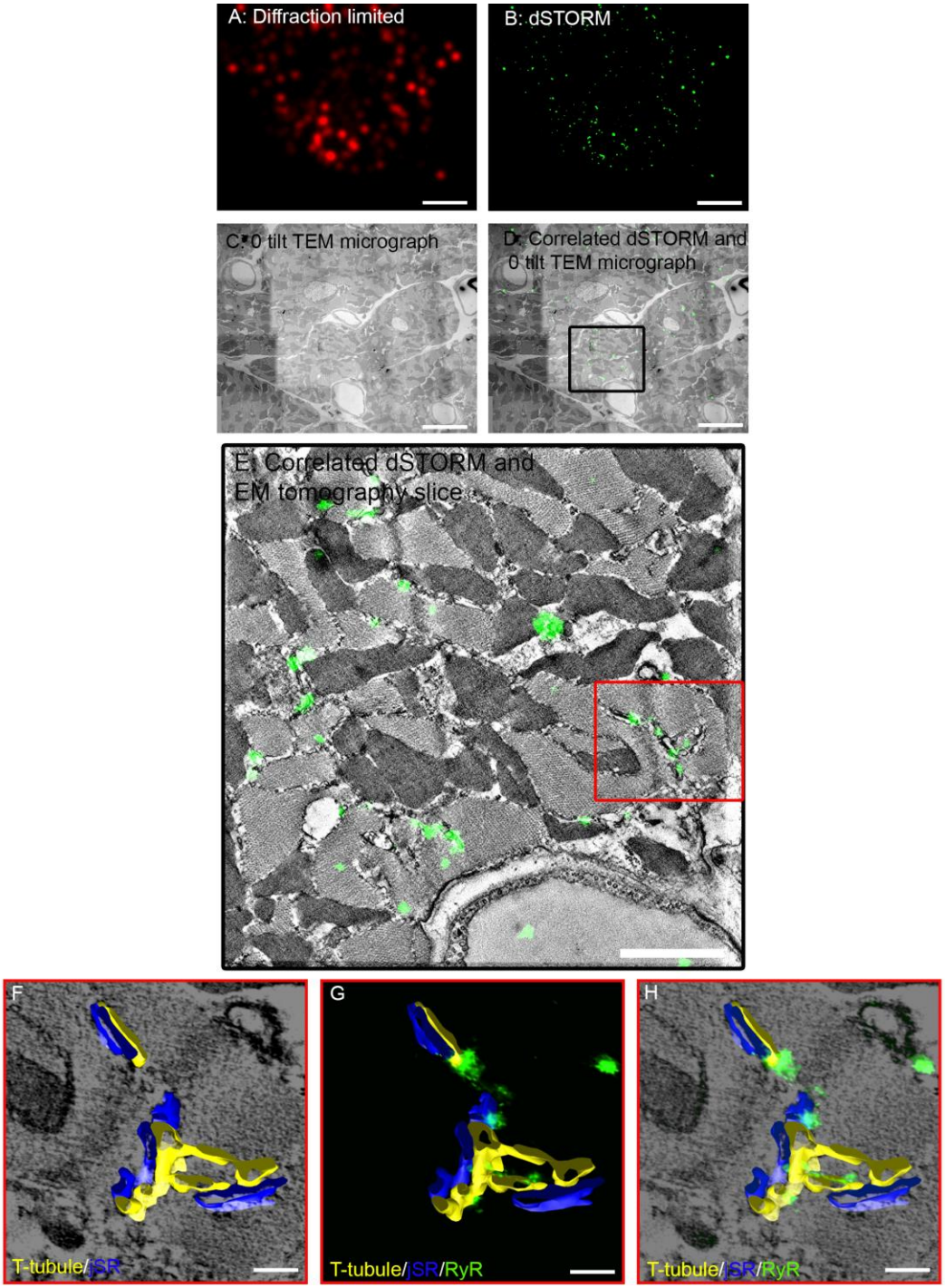
A: Diffraction limited
B: dSTORM
C: 0 tilt TEM micrograph
D: Correlated dSTORM and 0 tilt TEM micrograph
E: Correlated dSTORM and EM tomography slice
F
T-tubule/jSR
G
T-tubule/jSR/RyR
H
T-tubule/jSR/RyR

(Fig. 2.12F-H). Some fluorescence signal is observed close to, but not in association with, visible T tubule structures. Membranous organelles such as the SR and mitochondria could not be discerned with just osmium staining using either SEM imaging or EM tomography. As a result, the protocol was modified to use ferricyanide-reduced osmium for *en bloc* staining, which improved the fixation and enhanced the contrast of membranous organelles (Fig. 2.4). The increased contrast achieved by this imaging strategy allowed the SR to be visualized (Fig. 2.13E) in EM tomograms, and dyadic domains coincided with the correlated localization of RyR clusters determined in STORM imaging (Fig. 2.13F-H). The correlation process is described in Fig 2.14.

2.5. Discussion

The in-resin CLEM method presented in this paper offers several unique advantages. First, our protocol utilizes conventional immunolabeling approaches for protein targeting, allowing it to be easily adapted to a wide range of biological targets using existing antibodies. Non-specific labeling can be minimized by using primary antibodies covalently conjugated to Alexa 647. This strategy also helps minimize secondary antibody loss during EM processing. Optimized imaging conditions allowed us to achieve a localization accuracy of ~25 nm in cells and tissue. The attainable resolution of our method can be further improved by using nanobodies instead of conventional antibodies to minimize the “linkage error” that occurs due to the size of conventional antibodies [Ries et al., 2012]. Alternatively, genetic expression systems such as SNAP-tag and Halo-tag could be used to deliver the dye directly to the target [Keppler et al., 2003; Los et al., 2008; Perkovic et al., 2014]. The degree of heavy metal staining used allows the

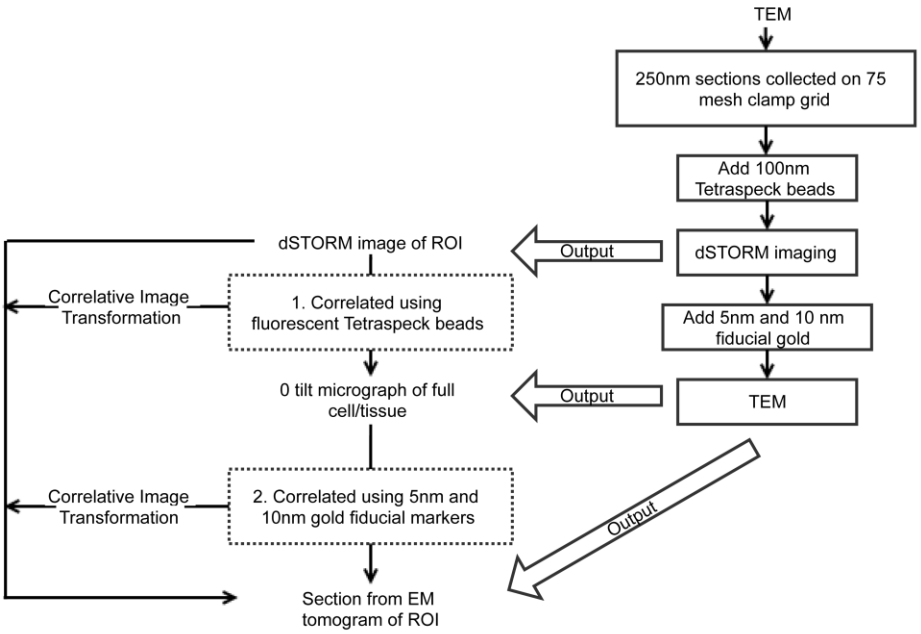

Figure 2.14. : Schematic overview of correlation schema for STORM and EM tomography. The flowchart details the steps involved in using Tetraspeck™ beads and gold fiducials as fiducial markers for landmark-based registration of STORM and EM tomography data

sample to be analyzed using multiple EM imaging modalities, including SEM, TEM and EM tomography, with just one dedicated staining protocol. Furthermore, the method presented here is compatible with multi-color super-resolution imaging, which would be an extremely attractive option for colocalization analyses of different proteins as well as for correlating multiple proteins with underlying cellular structures only visible at the EM level.

Resin embedding also offers the advantage of stabilizing cellular membranes for months. Imaging after sectioning the sample allows for the further investigation of molecular localization deep within the tissue instead of just at its surface. The thickness of the section also limits the amount of out-of-focus autofluorescence generated, particularly in tissue samples, thus improving fluorophore localization. In the case of correlated STORM and EM tomography imaging, the STORM data are only capable of providing 2D information regarding the distribution of the protein. To achieve 3D CLEM with better z-localization, we expanded our method to correlated STORM and array tomography. This application allows multiple serial sections to be imaged and aligned until the desired volume thickness has been achieved. Since the axial resolution of the volume is also limited by section thickness, further improvements in axial resolution can be attained by using 50 nm serial thin sections.

We also note that some fluorescent labeling did not perfectly correlate with cellular membranes. It is possible that since we are limited to a thin tissue slice for imaging, the structural membrane it is associated with is out of view of this section. The signal might also be mislocalized due to excessive section warping during STORM imaging that is not compensated for by simple affine correlation transformation and requires more rigorous, patch-based correlation

with higher order polynomial functions. Lastly, non-specific labeling and noise can also give rise to spurious signal. This is most likely because the fluorescent signal was out of the plane of focus due to the differing axial locations of RyRs and, on account of poor localization, was discarded during STORM data rendering. Additionally, as mentioned before, some antibody labeling may have been lost during EM sample preparation.

In summary, the method presented here combines the molecular specificity of LM with the high resolving power of EM to characterize the ultrastructure and molecular composition of the E-C coupling site in cardiomyocytes. These results will provide the groundwork for developing an understanding of cardiomyocyte ultrastructural architecture and the molecular mechanisms that lead to the reduced myocardial contractility seen in heart failure.

This chapter, in part, is a reprint of the material as it appears in Journal of Molecular and Cellular Cardiology, 2013. Das T, Hoshijima M. The dissertation author was the primary investigator and author of this paper. This chapter, in part, is currently being prepared for submission for publication of the material. Das T, Hoshijima M. The dissertation/thesis author was the primary investigator and author of this material.

Chapter 3:

E-C Coupling Molecule Compartmentation I:

Ryanodine Receptor

3.1. RyR population sub-types and organization

Based on their location and their contribution to E-C coupling, RyRs can be classified into two sub-populations: “junctional RyRs” and “non-junctional/extra- junctional RyRs” (Fig. 3.1) [Moore, 1957; Bers, 2002; Jayasinghe et al., 2009]. Junctional RyRs are the sub-population of RyRs localized on the jSR and are functionally coupled to LTCCs on the sarcolemma ~15 nm apart forming couplons. An action potential triggers Ca entry through the LTCCs into the dyadic cleft and triggers Ca release from the SR, resulting in a cytoplasmic Ca rise that triggers myofilament contraction [Bers, 2002; Sjaastad et al., 2003]. Thus, junctional RyRs serve as the elementary CRU for E-C coupling [Moore, 1957; Bers, 2002; Sjaastad et al., 2003; Jayasinghe et al., 2009]. ”Non-Junctional RyRs”, or “extra-junctional RyRs”, on the other hand, are localized on the SR, are not found within clefts, and do not directly couple to the LTCCs on the T-tubule [Chen et al., 2006; Sobie et al., 2006; Jayasinghe et al., 2009;Scriven et al., 2010; Torres et al., 2014].

3.2. Junctional RyR organization

3.2.1 Shape and size

The irregularity of the shape and size of dyads has been noted since their initial identification, as opposed to the relatively uniform geometry of triads in skeletal muscle [Porter and Palade, 1957; Fawcett and McNutt, 1969; Forbes and Sperelakis, 1982]. Two approaches have been consistently used to estimate the size of CRUs. One type of estimation is based on the length of dyad and peripheral junction profiles in 2D EM images, and the other measures the size of

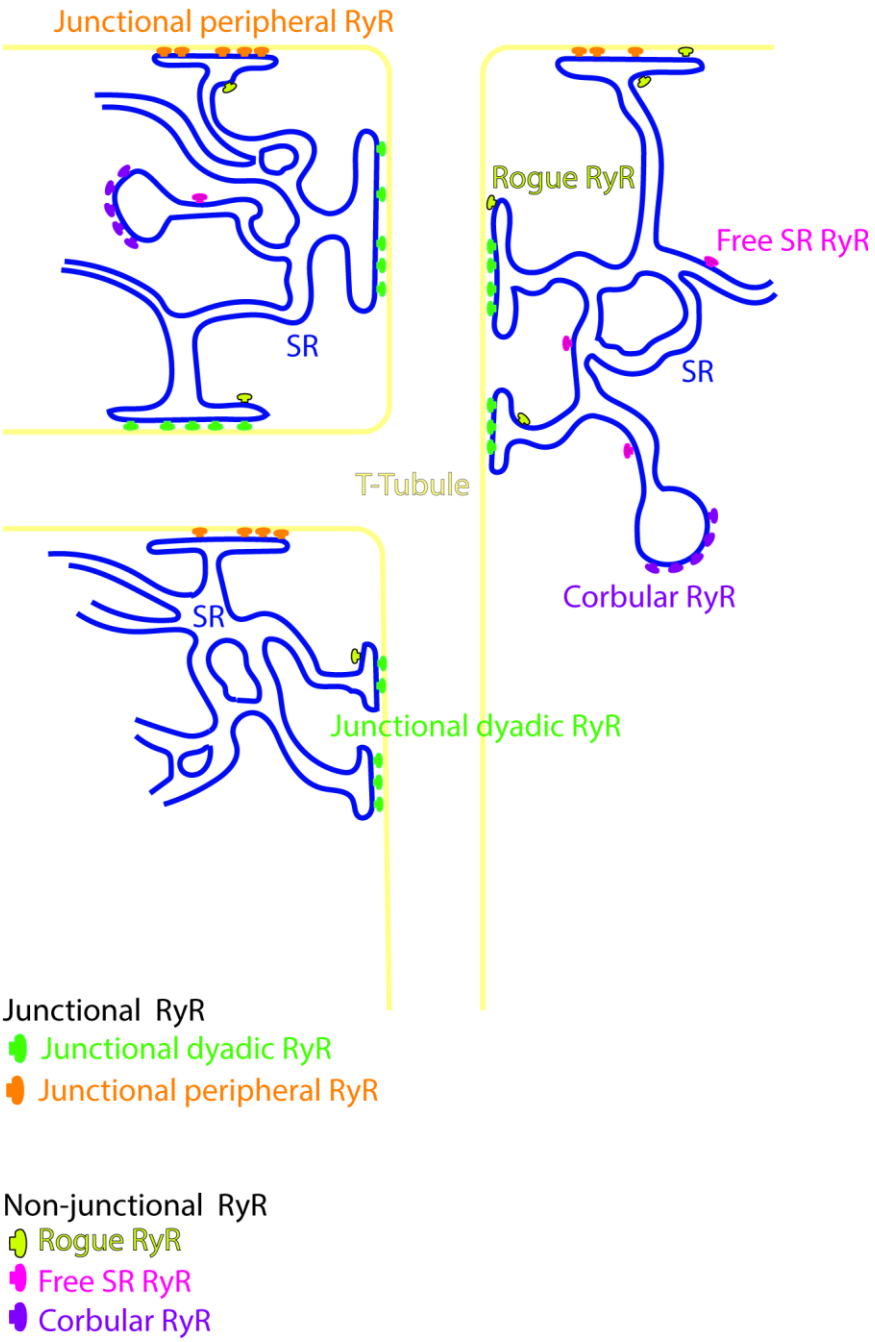

Figure 3.1. : Illustration of junctional and hypothesized non-junctional RyR distribution in cardiomyocytes.

RyR immunostaining observed in light microscopy. Resulting size estimates have been used in mathematical model studies.For example, Langer and Peskoff examined 2D EM images and estimated that the cleft is ~200 nm in radius (100 RyR feet; volume, 1.5×10^6 nm^3) [Langer and Peskoff, 1996]. Soeller and Cannell used the dyadic junction diameter of 100-400 nm for their model simulations [Soeller and Cannell, 1997].

Obtained by using EM, more realistic CRU size estimates appear in a later report by Franzini-Armstrong and colleagues, who meticulously measured the size and distribution of CRUs in various mammalian species [Franzini-Armstrong et al., 1999]. The CRU size was presented as the number of RyR feet, translated from the measurement of their random chords in electron micrographs. A simplified circular geometric model of the CRU and a surface area estimate of 29x29 nm^2 / RyR were used. The size of the dyads (cytoplasmic CRUs) ranged from 29-32 feet per dyad in a chicken ventricle to 267 feet per dyad in a rat ventricle. In mice, dyads were estimated to hold an average of 128 feet. A later study by Brochet and coworkers in rabbit hearts estimated ~66 feet in a CRU [Brochet et al., 2005].

The conversion of CRU area sizes to RyR foot density has been based on an assumption that dyads and peripheral junctions are filled with RyRs. Fawcett and McNutt observed ~15 nm diameter and ~20 nm regularly spaced apart globular densities within the dyadic cleft [Fawcett and McNutt, 1969]. Johnson and Summer reported processes ~20 nm in width which were spaced ~40 nm apart, center-to-center [Johnson and Sommer, 1967]. Protasi et al. observed that RyR feet aggregated in ordered arrays, which increased in size during development until they filled the entire junctional gap in avian myocardium

[Protasi et al., 1996]. The property of RyRs to spontaneously form regular array structures in solution and in lipid bilayer membranes supported these findings [Yin and Lai, 2000]. Nonetheless, the idea that the CRU junctions are filled with RyRs has been challenged recently (see below).

Instead of using area estimates to approximate the shape and size of CRUs, EM tomography was employed to directly demonstrate the 3D shape and size distribution of cytoplasmic CRUs that constitute a dyad (i.e. dyadic CRUs) in mouse ventricular myocytes [Hayashi et al., 2009]. The study revealed that dyadic CRUs are polymorphic and nearly an order of magnitude smaller than previously reported; their size distribution was non-Gaussian and significantly positively skewed (Fig. 3.2A). Accordingly, while the mean value of the dyadic cleft volume was 4.39×10^5 nm^3 (maximum RyR packing capacity = 43), it was estimated that more than one third of dyads are smaller than 1.52×10^5 nm^3 (maximum RyR packing capacity = 15). Based on the highly polymorphic geometry of CRUs revealed by EM tomography, we speculate that the difference between our estimate and previous reports is mainly due to the simplified circular geometry model of CRUs used in other studies [Hayashi et al., 2009; Yu et al., 2008].

Light microscopic imaging has also estimated CRU sizes based on the assumption that RyR clusters visualized by immuno-staining represent CRUs. Estimates made using conventional light microscopy were diffraction limited, resulting in relatively large CRU sizes. Chen-Izu et al. observed RyR clusters in transverse sections of rat ventricular cells and indicated that their size is close to the diffraction limit (~250 nm) while some larger clusters measured ~960 nm, translating to approximately 74 or fewer RyRs in most clusters [Chen et al., 2006].

Soeller et al. also calculated that the average number of RyRs is 78, which they further speculated to be between 120-260 if a 3D cluster shape is taken into consideration [Soeller et al., 2007].

Recent use of sub-diffraction-limit super-resolution optical imaging has revised these diffraction-limited observations and provided evidence supporting smaller sized CRUs, at least in peripheral junctions [Baddeley et al., 2009; Jayasinghe et al., 2012]. Using dSTORM, Baddeley et al. visualized the immuno-stained signal of RyRs in rat peripheral junctions at roughly 30 nm resolution and estimated that RyR cluster sizes follow a negative exponential distribution with an average of ~14 RyRs/cluster [Baddeley et al., 2009; Jayasinghe et al., 2012]. RyR clusters visualized in STORM had complex geometry with poor circularity. Cannell and Kong recently discussed this finding in peripheral junctions and stated that it is consistent with the previous estimate of the number of RyR channels needed to generate calcium sparks (up to 8) obtained by Wang et al. using in-focus imaging of calcium release events combined with a loose-seal patch-clamp [Wang et al., 2001; Wang et al., 2004; Cannell and Kong, 2012]. Despite the suggestion by Cannell and Kong, in our view it is not clear whether the number of RyRs forming each peripheral junction is lower than that of dyadic CRUs in the cytosol, as the application of these advanced fluorometric imaging technologies has so far been limited to near cell surface analyses [Cannell and Kong, 2012].

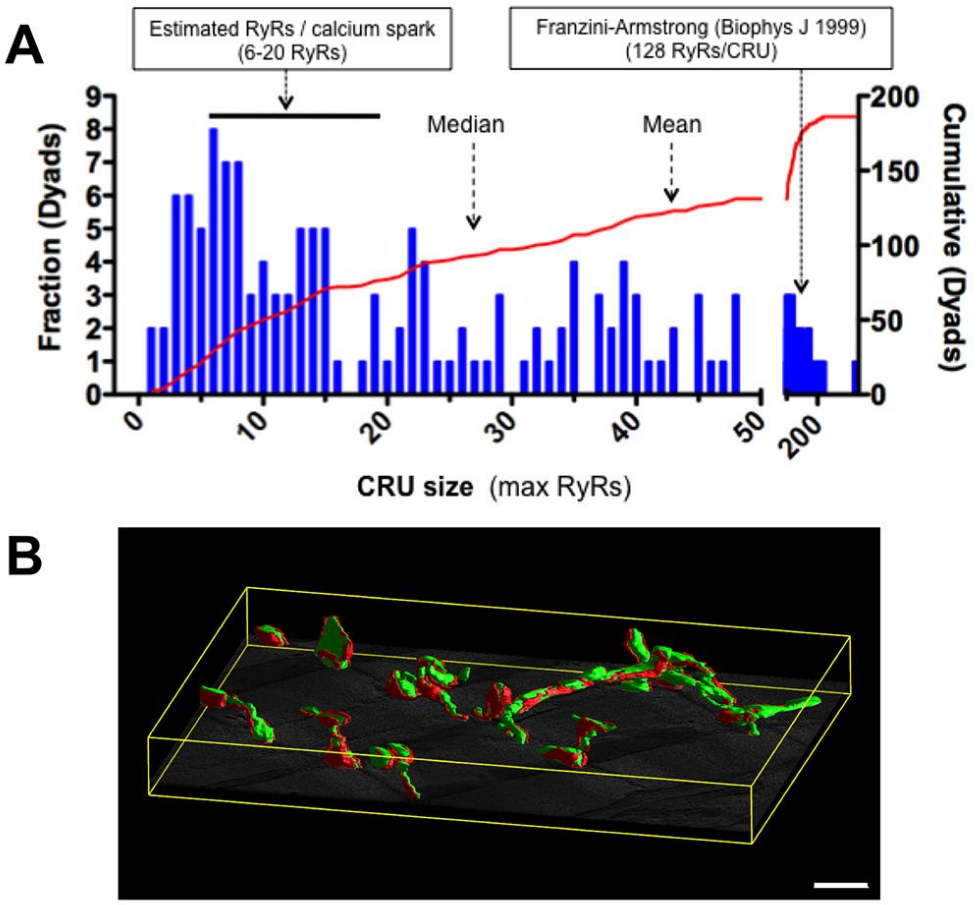

Figure 3.2. : The size distribution of dyadic CRUs in the mouse myocardium using 3D reconstructed volumes from EM tomography. (**A**) is a histogram of the maximum numbers of RyRs, which can be packed in each CRU in mouse ventricular cardiomyocytes. The distribution is positively skewed emphasizing that cluster sizes are much smaller than previously thought [56]. Arrows point to the mean and median values. The black horizontal bar indicates the size range, which corresponds to the RyR counts proposed to generate individual calcium sparks [55]. (**B**) 3D mesh models of T-system (green) are visualized with dyadic CRUs (red). The CRUs are highly polymorphic, varying in size and widely distributed along both longitudinal and axial tubules. Scale Bar 500nm. Data are reinterpreted from [Hayashi et al., 2009]

3.2.2. Membrane junctions and RyR clusters: filled vs. not filled

Franzini-Armstrong had previously suggested that single, large CRUs could be divided into smaller sub-units in cardiac myocytes, and this idea was confirmed in a study using EM tomography [Franzini-Armstrong et al., 1998; Hayashi et al., 2009] (Fig. 3.3). In mouse ventricular myocytes, a few feet clusters (i.e. small RyR clusters or CRU sub-domains) were observed in relatively large dyadic clefts. Such small RyR clusters are likely generated by the combination of some level of lateral free mobility of RyRs in junctional clefts and the self-assembly of RyRs, a molecular property that was demonstrated in lipid bilayer experiments using purified RyRs and in CHO cells in which RyR1 was overexpressed [Takekura et al. 1995; Yin and Lai, 2000]. A simulation study testing the Monte-Carlo stochastic self-assembly of RyRs showed random generation of small clusters [Baddeley et al., 2009].

A recent study by Asghari et al. has provided further evidence of smaller clusters, or archipelagos, of RyRs distributed within the dyadic cleft using EM tomography [Asghari et al, 2012; Asghari et al., 2014]. Based on the best match between an EM tomogram of a dyadic cleft and array of RyRs, Asghari et al. claimed that RyRs likely reside in the cleft as a mixture of “checkerboard” configuration and side-by-side packing [Yin et al., 2008; Asghari et al, 2012; Asghari et al., 2014]. Our attempt to map single RyRs in a dyadic CRU is shown in Figure 3, which is consistent with the observation of Asghari et al. Though the missing RyRs could be a result of poor contrast in EM in the noisy environment, the idea of incomplete filling of junctional clefts with RyRs is supported by the biochemical estimation of RyR density in junctions. In a mouse study, high affinity ryanodine binding density estimated ~7.7 RyRs in an average-sized

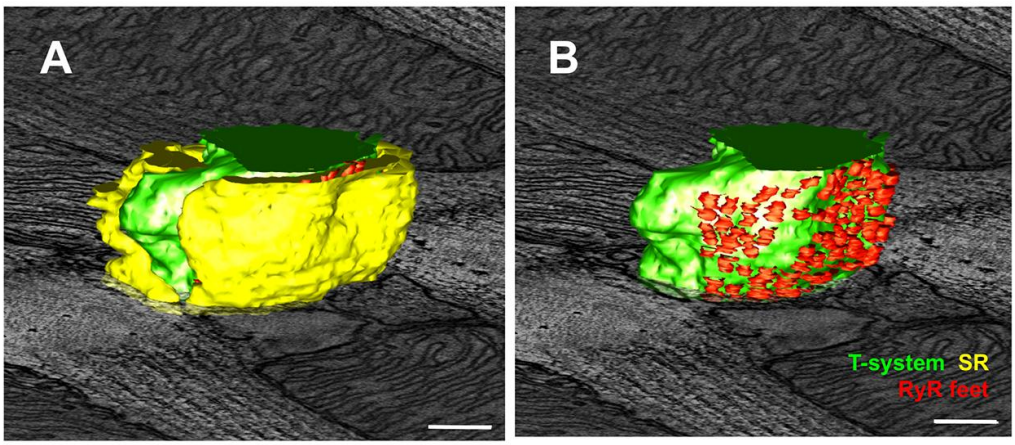

Figure 3.3. : 3D EM tomography reveals the nano-scale 3-D structure of individual CRUs. (**A-B**) are high-resolution surface mesh models of RyRs (red), T-tubules (green) and jSR (yellow) shown with a 2D slice image reconstructed from mouse cardiomyocyte EM tomography. **B** is after the removal of jSR from **A**. EM tomography enables the 3D mapping of individual RyR feet in the junction between the opposing jSR and T-tubule membranes. Scale Bars 100 nm. RyR segmentation is added to a tomogram shown in a previous publication [Hayashi et al., 2009].

dyadic CRU, which has a volume capable to hold 43 RyRs maximally [Hayashi et al., 2009].

3.2.3. Cytoplasmic distribution of RyR clusters and association with the sarcolemma

The T-system is formed in the late embryonic through early neonatal stages of mammalian ventricular cardiomyoycte development [Brette and Orchard, 2003]. While it remains unclear whether the T-system elongates from the outside or new membranes are added at its tip, this is a process where dyadic membrane couplings are generated between new branches of the T-system and proliferating SR [Di Maio et al.,2007] . Asghari et al. examined RyR feet in EM and reported that cytoplasmic CRUs are almost exclusively associated with the T-system in rat ventricular myocytes [Asghari et al., 2009]. Subsequently, Page and Surdyk-Droske used a stereological approach in various mammalian species and calculated the proportion of T-system membrane contribution to junctions [Page and Surdyk-Droske, 1979]. Estimates ranged from ~20% in rabbit to ~47% in rats and ~40% in mice [percentages translated from Table 2 of [Page and Surdyk-Droske, 1979]]. These data, combined with CRU edge-to-edge distances of 313 ± 21 nm measured in mice and 414 ± 24 nm measured in rats, provided enough evidence to conclude that RyR clusters densely occupy the T-system membrane surface [Franzini-Armstrong et al., 1999].

EM tomography took advantage of the geometric accuracy in 3D, refined measurements, and found that typical CRU edge-to-edge distances are an order of magnitude smaller than previous estimates, more precisely an average of 19.9

nm in mouse ventricular cardiomyocytes [Hayashi et al. 2009]. Furthermore, the distribution of cytoplasmic CRUs throughout the T-system, including axial branches (Fig. 3.2B), is consistent with the independent observations by Asghari et al. [Asghari et al , 2009]. Of interest, the immune-staining of RyRs and LTCCs in the study of Asghari et al. found a higher level of colocalization of these two proteins in the axial junctions compared to transverse junctions, suggesting the active involvement of axial junctions in E-C coupling.

Light microscopy has also been used to measure distances between neighboring RyR clusters. This measurement was especially challenging in diffraction-limited microscopy due to the fact that the distance is near or under the limit of resolution. Scriven et al. showed that RyR clusters were an average of 0.98 μm apart in isolated rat ventricular cardiomyocytes, corresponding to myofibril width [Scriven et al., 2009]. The measurements carried out by Chen-Izu et al. were similar, as they calculated the average center-to-center distance between neighboring RyR clusters in transverse sections (1.05 μm) and in longitudinal sections (0.83 μm) in isolated rat ventricular cardiomyocytes, which was then confirmed by Soeller et al. [Izu et al., 2006; Baddeley et al., 2009a]. While these studies measured RyR cluster distances primarily in the cytosol, Baddeley et al. used the STORM technology to reveal the high-resolution RyR cluster distribution in peripheral junctions [Baddeley et al., 2009b]. While the average center-to-center distance of peripheral RyR clusters was estimated to be 308 nm, Baddeley et al. concluded that about one third of RyR clusters, which are located close to the surface membrane, have their edges within a 50 nm distance of their closest neighbors [Baddeley et al., 2009b].

3.3 Non-junctional RyR organization

As evident from the previous section, junctional RyR distribution has been well characterized by both LM and EM independently; however, the same cannot be said for non-junctional RyRs. Non-junctional RyRs are a sub-population of RyRs that localize on the SR outside of the junctional domain [Chen et al., 2006; Sobie et al., 2006; Jayasinghe et al., 2009;Scriven et al., 2010; Torres et al., 2014]. By definition, these include clusters of RyRs, identified as spherical vesicles of the nSR in the region of the Z-line, especially in mature mammalian atrial cardiomyocytes. These non-junctional channel clusters have been termed “coated vesicles”, owing to their similarity to clathrin-coated pits of the Golgi system, as well as “extended junctional SR” and “corbular SR” [Fawcett, 1969; Jewett, 1973; Sommer and Waugh, 1976]. In atrial myocytes, the corbular SR form a 3D network lattice of CRUs, but, since they are uncoupled from LTCCs, they cannot directly participate in E-C coupling. Jorgensen and colleagues suggested that these structures act as secondary amplification systems, triggered by Ca release from neighboring junctional RyRs activated during E-C coupling [Jorgensen et al., 1993]. It is of importance in atrial and ventricular cells of species with sparse T-tubules, where it has been suggested that they propagate Ca to the interior of the cell for contraction [Sommer and Waugh, 1976; Jorgensen et l., 1993; Franzini-Armstrong et al., 1999]. As such, rabbit ventricular myocytes with limited T-tubule invaginations have a higher density of non-junctional RyRs than their rodent counterparts. Torres and colleagues have recently demonstrated that these non-junctional RyR clusters are capable of producing spontaneous sparks, further cementing their roles as potential contributors to E-C coupling [Torres et al., 2014].

Non-junctional RyRs have also been proposed to be associated with structures other than the T-tubule, such as the mitochondria and nucleus. Immunhistochemistry and diffraction-limited LM have shown that a sub-set of cardiac RyRs are bound to the muscle A-kinase anchoring protein (mAKAP) localized on the nuclear envelope [Kapiloff et al., 2001, Pare et al., 2004]. It has been proposed that this Ca ion-sensitive signaling complex participates in second messenger-mediated signal transduction processes Kapiloff et al., 2001, Pare et al., 2004]. Similarly, another subset of RyRs has been implicated in aiding mitochondrial Ca intake. Recent EM experiments have confirmed tether-like structures coupling the SR to the mitochondria, suggesting a form of local control between SR-mediated Ca release and mitochondrial uptake [Perkins et al., 2001; Csordas et al., 2006; Franzini-Armstrong, 2007; Hayashi et al., 2009]. It has been hypothesized that junctional RyRs activate neighboring non-junctional RyRs in close apposition to mitochondria to couple cardiac muscle excitation with oxidative energy production [Csordas et al., 2006]. These non-junctional RyRs have yet to be visualized, and their density and organization relative to mitochondria are still undetermined. This is not to be confused with mitochondrial RyRs, which have been proven to localize on the inner mitochondrial membrane in cardiomyocytes through a series of biochemical and electrophysiological experiments [Beutner et al., 2001; Beutner et al, 2004]. It has been suggested that these RyRs are the skeletal-muscle type-isoform RyR, and are responsible for sequestering Ca into mitochondria quickly and transiently during E-C coupling Ca oscillations for ATP production.

Diffraction-limited LM studies of immunolabeled RyRs report that ~16% of RyR clusters are disassociated from T-tubules in rat ventricular myocytes [Chen-

Izu et al., 2006]. However, LM imaging using membrane markers alone cannot accurately discern whether these clusters are actually non-junctional or just RyR tetramers being trafficked through the cell. Characterizing the distribution of non-junctional RyRs has become even more challenging with the proposal of the existence of isolated single non-junctional RyRs called “rogue” RyRs [Sobie et al., 2006]. Although these rogue RyRs are yet to be directly visualized, it has been suggested they give rise to “quarky” Ca releases and participate in invisible Ca leak from the SR [Brochet et al., 2006; Sobie et al., 2006]. Understanding their distribution is especially important to understand the pathology of heart failure, where non-junctional RyRs are produced by T-tubule loss or reorganization, creating ‘orphaned’ RyRs [Louch et al., 2004; Song et al., 2006; Landstrom et al., 2011; Wu et al., 2012]. This results in reduced coupling efficiency, leading to an increased propensity for arrhythmia and reduced Ca transient. Although EM tomography allows for the identification of typical structures of the extended-junctional SR or corbular SR, high background noise levels in the cytoplasm significantly limit the fidelity of identifying non-junctional RyRs in EM tomograms. Electrophysiological recordings have provided insight into the role of non-junctional RyRs in E-C coupling, but the distribution of non-junctional RyRs is yet to be ascertained using conventional LM or EM [Chen-Izu et al., 2006; Soeller et al., 2007; Jayasinghe et al.; 2009; Torres et al., 2014].

Thus, in this chapter, a broad range of subcellular features will be explored in a correlated fashion by taking advantage of the complementary information available from EM and LM. CLEM was used to bridge the different resolutions and image contrast features to contribute novel insights into the localization of junctional and non-junctional RyRs.

3.4. Methods

Please refer to Section 2.3 in Chapter 2. The reduced osmium protocol was followed to impart contrast to organelles for differentiating between junctional and non-junctional RyR.

3.5. Results

3.5.1. Correlated STORM and SEM of RyRs in junctions and non-junctional cytoplasm

Correlated STORM-SEM imaging allows the identification of RyR cluster distributions with respect to all the membrane organelles they associate with across the whole (Fig. 3.4). Thus, by taking advantage of the geometric cellular map provided by SEM imaging, we were able to strictly classify RyR clusters as junctional or non-junctional. RyR clusters located at the interface between the sarcolemma (including the T-system) and the relatively flat junctional cistern of SR were classified as junctional (Fig. 3.5A). All remaining RyR clusters associated with the SR membrane were classified as non-junctional (Fig 3.5B and 3.5C).

Closer examination of RyR clusters along the cell edge and Z-lines showed that the vast majority of the RyRs were junctional. At the cell edge, RyR clusters in close association with the sarcolemma formed peripheral couplings with SR. Most caveolae were not associated with any RyR signals. In the interior of the cell, junctional RyRs were correlated with dyadic structures along the T-tubules at the Z-lines. Non-junctional RyR were clearly identified along the nSR. Some were closely associated with the nucleus as seen in Fig. 3.4 and a significant number were in close apposition with the mitochondria. Non-junctional

Figure 3.4. : Correlated in-resin STORM data and SEM of junctional and non-junctional RyR with RyR –Ax 647 in cardiac mouse tissue processed with reduced osmium. The region of interest is located using diffraction limited microscopy (A) followed by subsequent dSTORM imaging (B). The section is post stained and the same area is imaged using SEM at low magnification (C). 100nm Tetraspeck™ are used to correlate the dSTORM image with SEM at low (D) and high magnification (E). Using reduced osmium lends better contrast to cellular and organelle membranes (E). Non-junctional RyR clusters (green) are identified on the nSR and junctional RyR clusters are identified on the jSR at the Z-lines adjacent to T-tubules. Scale Bars 4um (A, B, C, D), 1um (E).

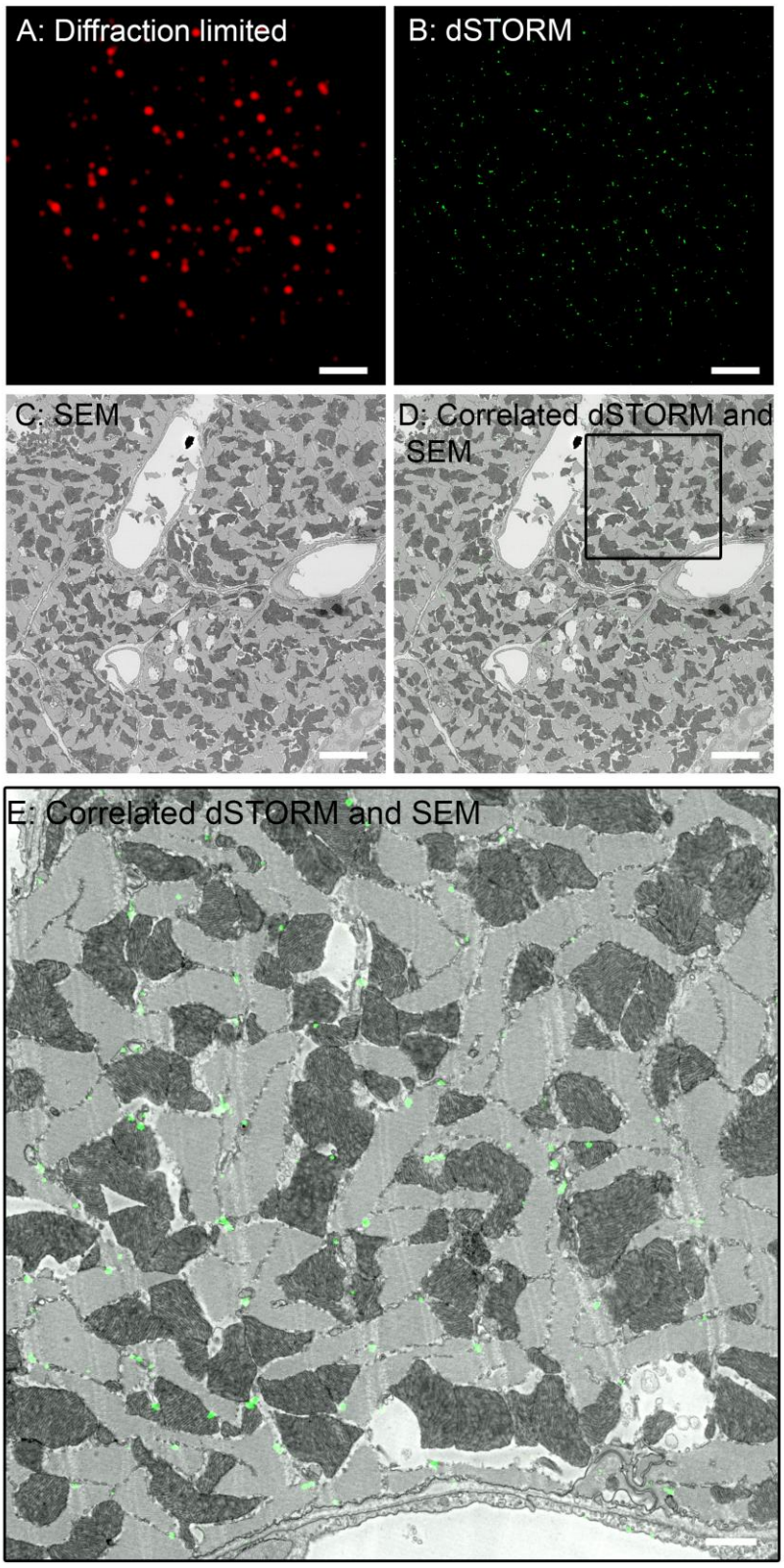
A: Diffraction limited
B: dSTORM
C: SEM
D: Correlated dSTORM and SEM
E: Correlated dSTORM and SEM

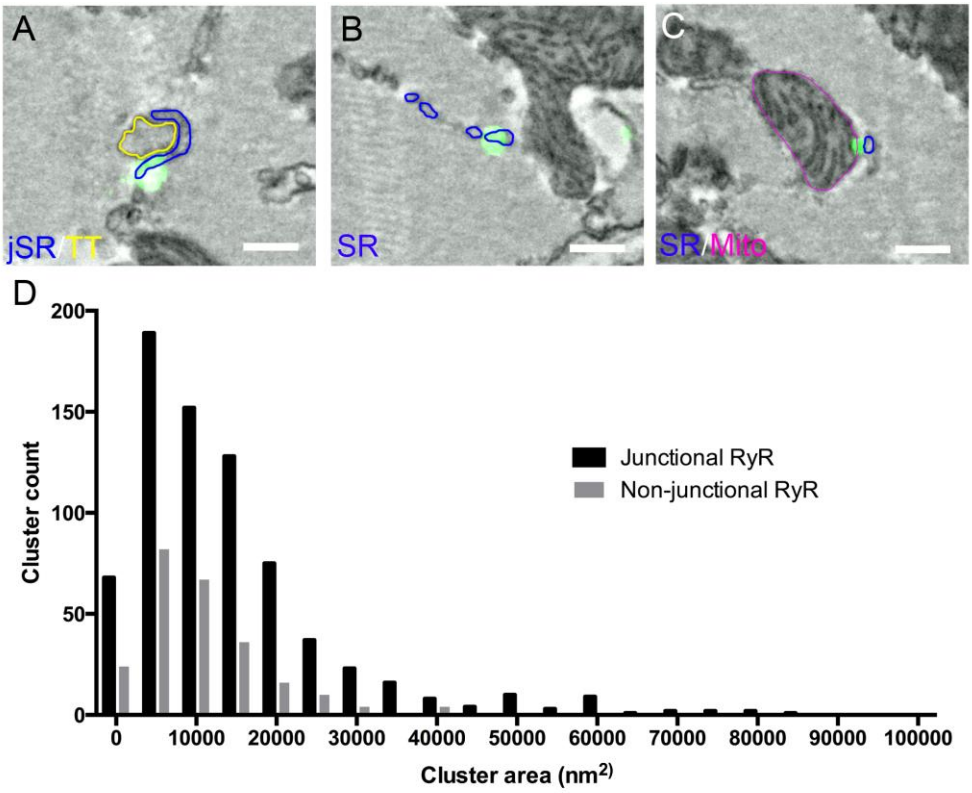

Figure 3.5. : Junctional and non-junctional RyR distribution in correlated STORM and SEM. Junctional RyR clusters (green) were identified on the jSR (blue) at the Z-lines adjacent to T-tubules (TT, yellow) in (A).Non-junctional RyR clusters (green) were identified on the nSR (blue) (B,C) with a significant population closely associated with the mitochondria (C). A histogram of the RyR cluster sizes shows that the distribution is exponential (D) with non-junctional RyRs accounting for 21% ± 4.5% (mean ± SD, cells (n) =6, animals (n) =2) of the total RyR clusters in mouse ventricular tissue. Scale Bars 100nm (A, B, C).

cluster sizes were observed to be smaller than junctional cluster sizes. The RyR cluster quantification strategy developed by Baddeley et al. was applied to the in-resin STORM imaging results to determine that non-junctional RyRs accounted for 21% ± 4.5% (mean ± SD, cells (n) =6, animals (n)=2) of the total recorded RyR localization signals in mouse ventricular tissue. The frequency histogram of RyR cluster size distributions was found to be exponential with mean cluster sizes of 14,317 ± 526 nm^2 (Mean ± SEM) for junctional and 10,286 ± 526 nm^2 (Mean ± SEM) for non-junctional RyRs, respectively (Fig. 3.5D).

3.5.2. Correlated array tomography

The 3D distribution of RyRs was examined using array tomography. The T-tubule and jSR in each section were segmented and meshed to generate a 3D model, which is shown overlaid with STORM data to demonstrate how RyRs localize within couplons (Fig. 3.6 Bi-iv). The 3D distribution confirms recent reports stating that RyRs are not densely packed in the dyadic cleft.

3.5.3. Correlated STORM and EM tomography of RyRs in junctions and non-junctional cytoplasm.

SEM images acquired using a backscattered electron detector for correlated imaging with STORM lack the contrast and resolution to identify individual RyR tetramers. Thus, we applied EM tomography following STORM imaging to correlate RyR localizations with 3D sub-cellular structures at nanometer scale resolutions.

Multiple tilt series combined with iterative reconstruction methods at high magnification (as described in chapter 2) allowed electron dense “foot” structures

Figure 3.6. : Correlated junctional RyR array tomography. 4 consecutive 80nm thin sections were imaged using STORM followed by SEM imaging (Ai, AiI, Aiii, Aiv) and then correlated (insets of Ai, Aii, Aiii, Aiv). Using patch cross-correlation, the consecutive sections are aligned into a 3D volume. The jSR (blue) and T-tubules (yellow) is segmented in each section and a surface mesh model is shown in correlation with RyR fluorescence data at corresponding z positions (Bi, Bii, Biii, Biv). Scale Bars 150nm (Ai, AiI, Aiii, Aiv), 75nm (Bi, Bii, Biii, Biv).

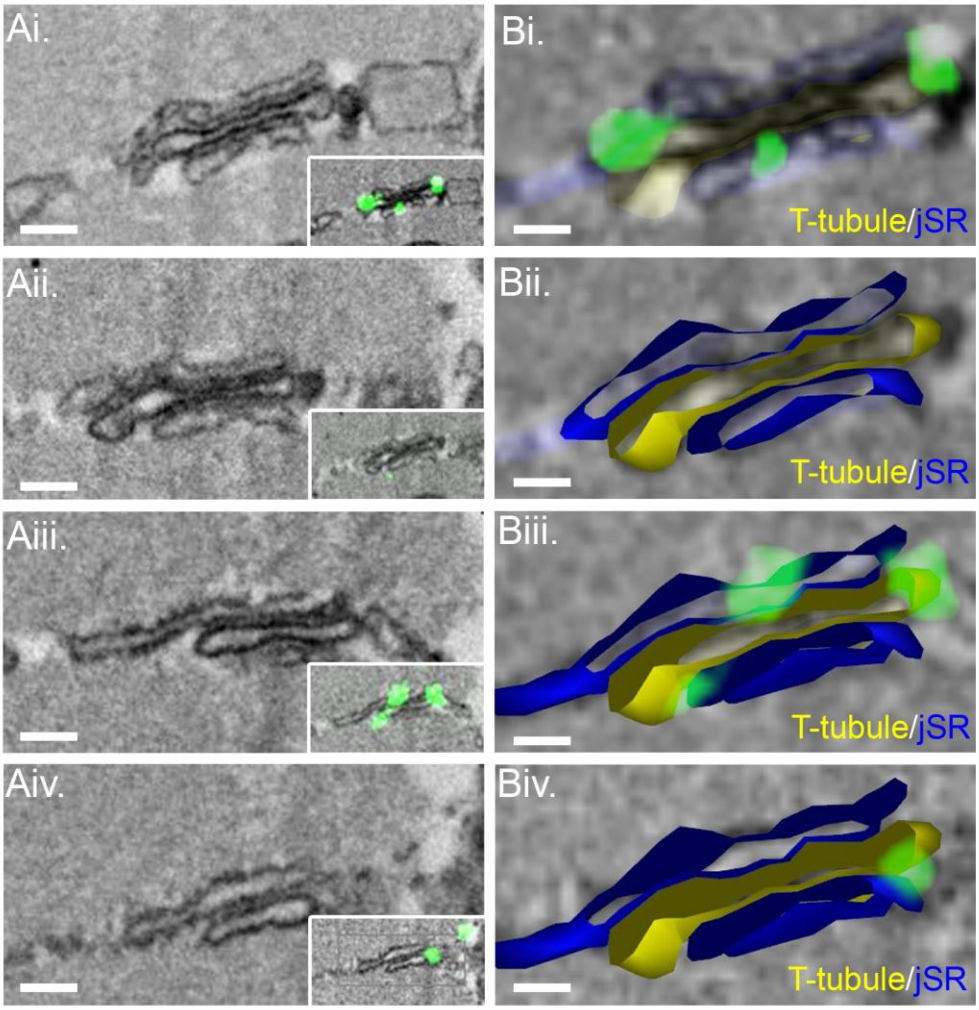
Ai.
Bi.
T-tubule/jSR
Aii.
Bii.
T-tubule/jSR
Aiii.
Biii.
T-tubule/jSR
Aiv.
Biv.
T-tubule/jSR

to be visualized within the dyadic cleft. The mitochondria (magenta), T-tubule (green), jSR (yellow) and RyR (red) were manually segmented in the tomogram (Fig. 3.7.3b) and correlated with green fluorescent STORM (Fig. 3.7.3a) data in an individual tomogram slice (Fig. 3.7.3c). The contours were meshed to generate surface mesh models of the T-tubule (green), SR (yellow) and RyR (red) (3.7.4b), and were correlated with green fluorescent STORM (3.7.4a) data and shown in reference to a 2D image slice reconstructed from the tomogram. Correlation confirmed junctional “foot” structures coincided with the correlated localization of RyR clusters determined in STORM imaging (Fig. 3.8).

Examination of the correlated STORM RyR localizations in tomographic volumes also revealed that non-junctional RyRs located on the nSR (Fig. 3.9). While some non-junctional RyRs were observed to be in close proximity to the dyadic cleft (Fig. 3.9), the current imaging found that the localization of the other majority was associated with junctions between nSR and mitochondrial outer membranes (Fig. 3.10). The RyR localization signals determined in STORM were labeled adjacent to the mitochondrial-SR tethers, which we and others previously reported. The mitochondria (magenta), jSR (yellow), and tethers (red) were manually segmented from the tomogram (Fig. 3.10F) and correlated with green fluorescent STORM data in an individual tomogram slice. The contours were meshed to generate surface mesh models of the T-tubule (green), SR (yellow) and tether (red) (Fig. 3.10G) and correlated with green fluorescent STORM data and shown in reference to a 2D slice image reconstructed from the tomogram.

Figure 3.7. : Correlated STORM and electron tomography of immunolabeled RyR: The region of interest is first dSTORM imaged (1a). The same section is imaged at 0 tilt using a TEM at low magnification (1b). 100nm Tetraspeck™ beads are used to correlate the STORM image with the low magnification TEM micrograph (1c). A region is identified with RyR fluorescence labeling (boxed region in 1a, 1b, 1c) and is imaged for EM tomography. RyR (green) fluorescence (2a) can be identified on the SR, and within the dyadic cleft at z-lines (2c) in individual sections of the tomogram (2b). The mitochondria (magenta), T-tubule (green), jSR (yellow) and RyR (red) are manually segmented in the tomogram (3b) and correlated with green fluorescent STORM (3a) data in an individual tomogram slice (3c) . The contours are meshed to generate surface mesh models of the T-tubule (green), SR (yellow) and RyR (red) (4b) and correlated with green fluorescent STORM (4a) data and shown in reference to a 2D slice image reconstructed from tomography (4c). Within the dyadic cleft (black box, 4c) , fluorescent RyR data (green) coincides with manually segmented EM RyR (red). Non-junctional fluorescent RyR are also localized on the SR with no association with T-tubules (red boxes,4c). Scale bars 500nm (1a, 1b, 1c), 100nm (2a, 2b, 2c, 3a, 3b, 3c, 4a, 4b, 4c).

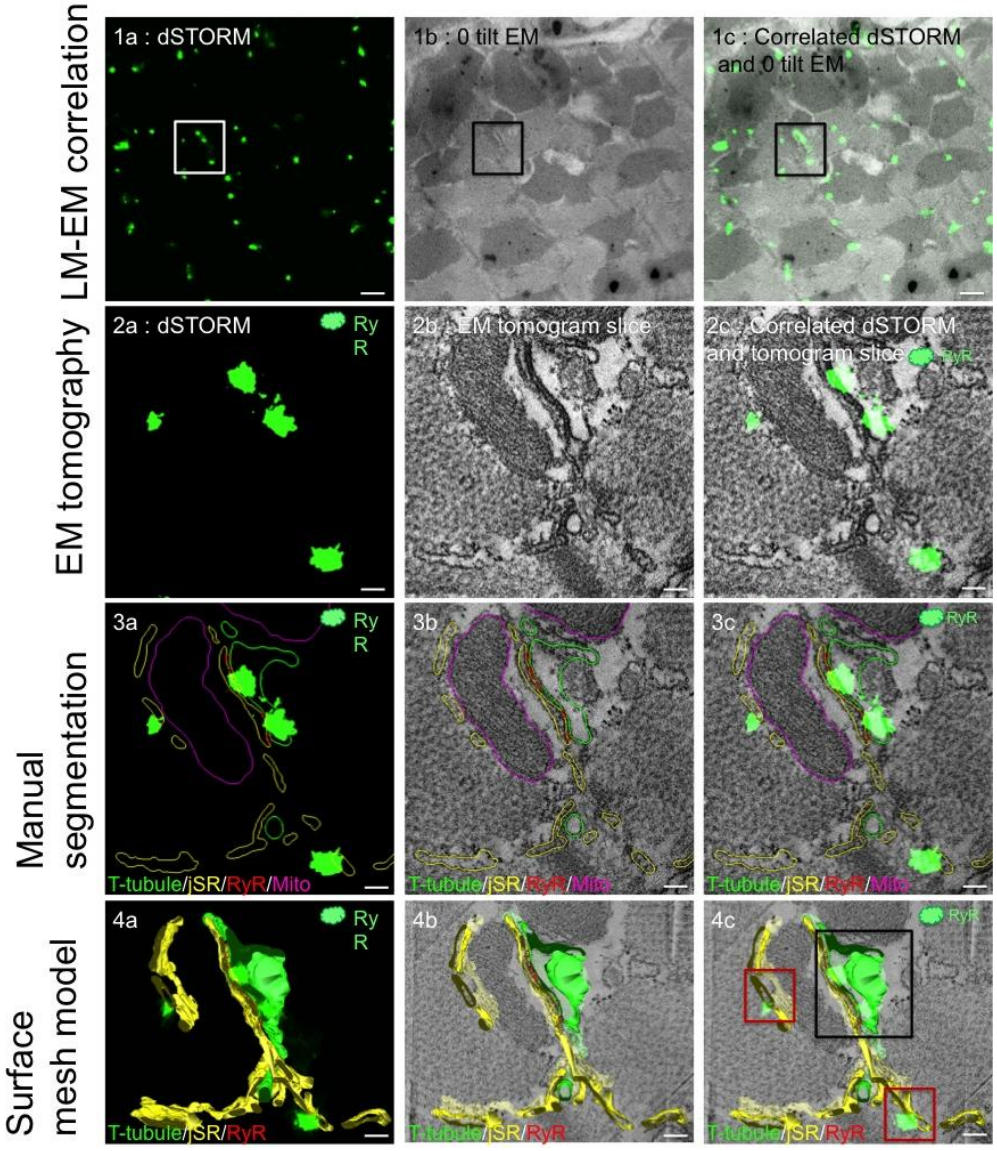
LM-EM correlation
EM tomography
Manual segmentation
Surface mesh model
1a : dSTORM
1b : 0 tilt EM
1c : Correlated dSTORM and 0 tilt EM
2a : dSTORM
Ry R
2b : EM tomogram slice
2c : Correlated dSTORM and tomogram slice
RyR
3a
3b
3c
T-tubule/jSR/RyR/Mito
4a
4b
4c
T-tubule/jSR/RyR

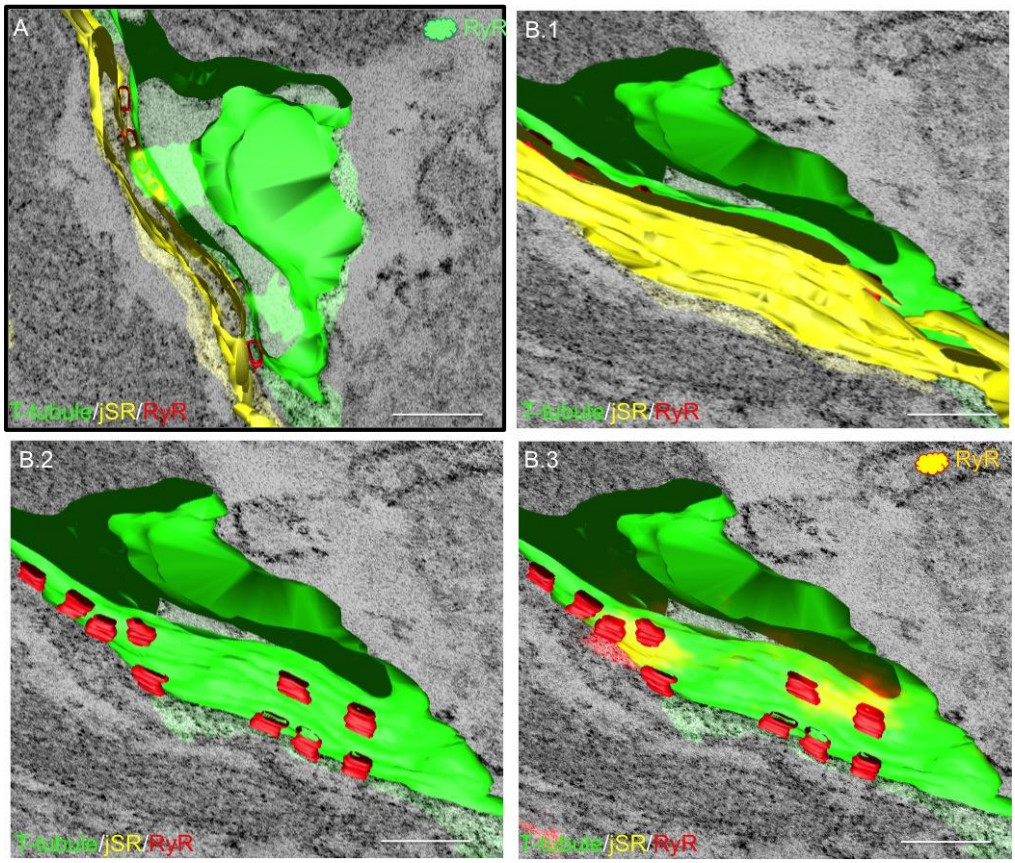

Figure 3.8. : Correlated STORM and electron tomography data of junctional RyR: (A) is a magnified top view of the dyadic cleft and junctional RyR identified in the black box in Figure 1 (4c). Mesh models of the T-tubule (green), SR (yellow) and RyR (red) are correlated with fluorescent STORM RyR data (green) in (A). EM tomography enables the 3D mapping of individual RyR feet in the junction between the opposing SR and T-tubule membranes .The STORM data (green) localizes with the RyR (red) structures identified in the tomogram. (B.1) is a side view of the T-tubule (green), SR (yellow) and RyR (red) in (A) shown in reference to an individual tomogram slice. (B.2) is after the removal of the SR to reveal RyR (red) organization within the cleft. The correlated STORM fluorescence (red) is yellow where it associates with the T-tubule and RyR mesh models (red) (B.3). Scale bars 100nm.

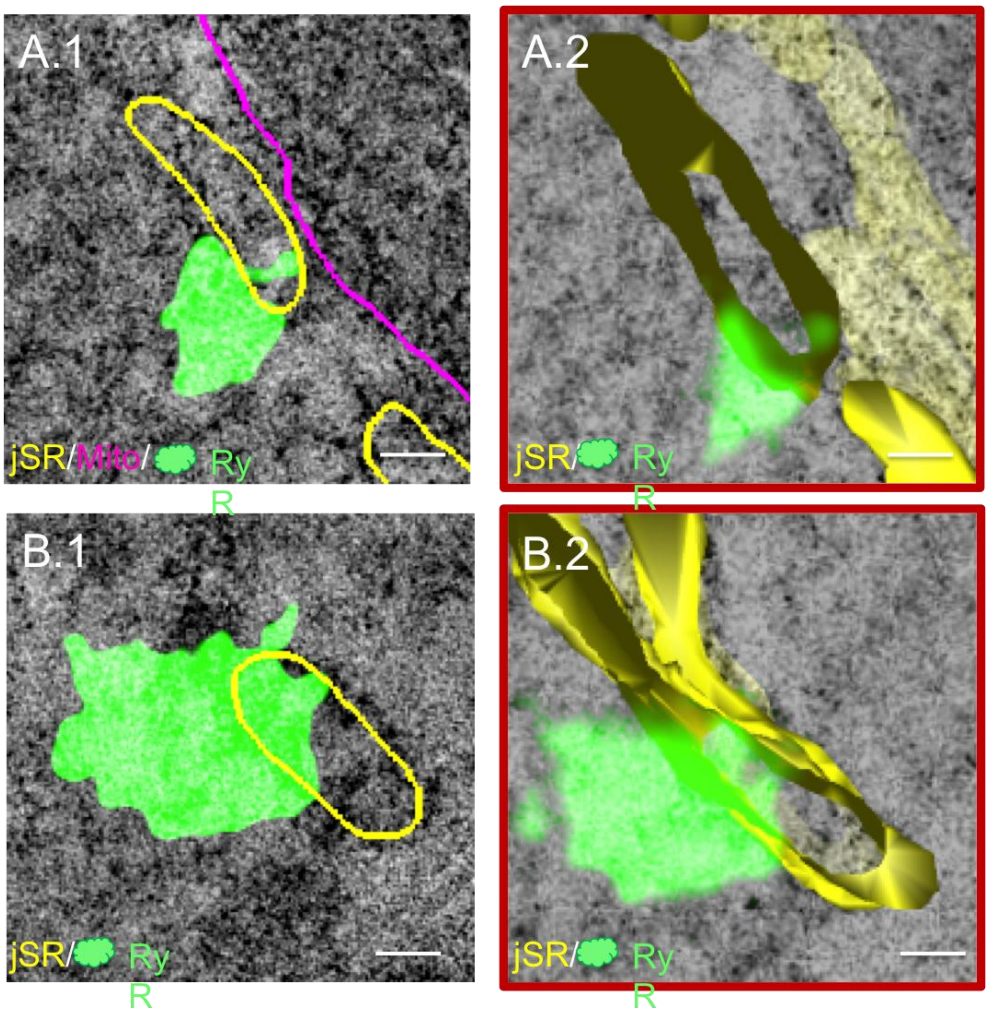

Figure 3.9. : Correlated STORM and electron tomography data of non-junctional RyR: (A.1) and (B.1) correlate fluorescent STORM RyR data (green) with manually segmented SR (yellow) and mitochondria (magenta) in a 2D slice image reconstructed from tomography. (A.2) and (B.2) correlate fluorescent STORM RyR data with mesh models of SR identified in (A.1) and (B.1) respectively. The correlated fluorescent data provided by STORM allows for the positive identification of the difficult to locate RyR not associated with the dyadic cleft. RyR clusters (green) can be seen associating with mesh models of SR (yellow) with no interaction with T-tubules (A.2,B.2) .Scale bars 50nm.

Figure 3.10. : Correlated STORM data and EM tomography of mitochondria associated non-junctional RyR. The region of interest is located diffraction limited microscopy (A) followed by dSTORM imaging (B). The same section is imaged at 0 tilt using a TEM at low magnification (C). 100nm Tetraspeck™ beads are used to correlate the dSTORM image with the low magnification TEM micrograph (D). A region is identified with non-junctional RyR fluorescence in close association with mitochondria (boxed region in D) and is imaged for EM tomography. Non-junctional RyR (green) fluorescence can be identified on the nSR (E). The mitochondria (magenta), jSR (yellow) and mitochondrial tethers (red) are manually segmented in the tomogram and correlated with green fluorescent dSTORM data in an individual tomogram slice (F). The contours (F) are meshed to generate surface mesh models of the mitochondria (magenta), SR (yellow) and tether (red) and correlated with green fluorescent STORM data and shown in reference to a 2D slice image reconstructed from tomography (G).(H) is (G) with the SR removed to show the close association between the mitochondrial tethers and correlated RyR fluorescence. Scale bar 2.5um (A, B, C, D), 200nm (E), 100nm (F, G, H).

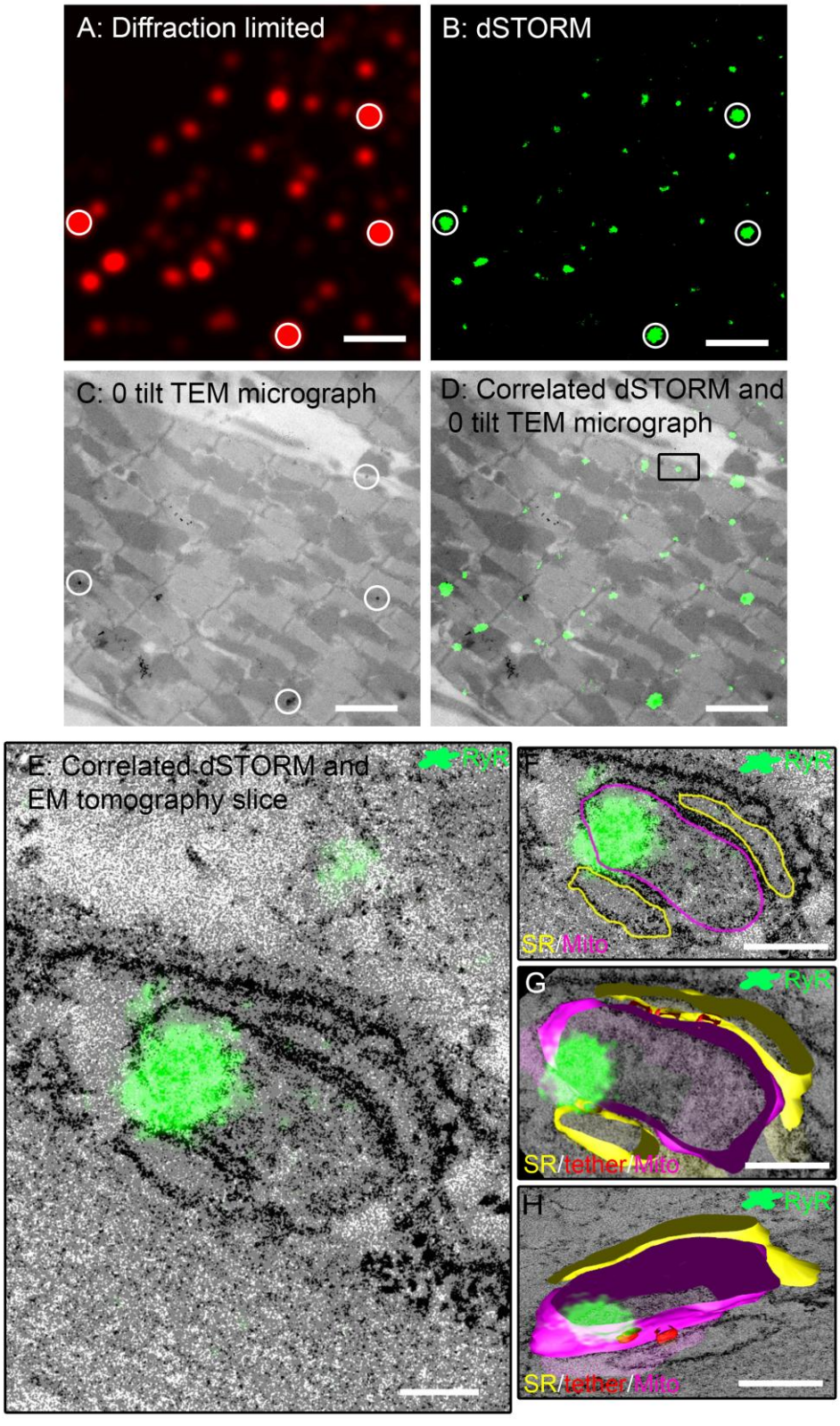
A: Diffraction limited
B: dSTORM
C: 0 tilt TEM micrograph
D: Correlated dSTORM and
0 tilt TEM micrograph
E: Correlated dSTORM and
EM tomography slice
RyR
F
RyR
SR/Mito
G
RyR
SR/tether/Mito
H
RyR
SR/tether/Mito

3.6. Discussion

Electrophysiological recordings coupled with simultaneous Ca measurements of the cytosol and SR lumen have suggested the significance of non-junctional RyRs in E-C coupling and Ca wave propagation; however, the distribution of non-junctional RyRs has yet to be elucidated in a cellular context using conventional LM or EM [Chen-Izu et al., 2006; Soeller et al., 2007; Jayasinghe et al.; 2009; Torres et al., 2014]. Thus, for the first time, both junctional and non-junctional RyRs were positively identified and visualized using targeted fluorescent antibodies in 2D SEM micrographs as well as in 3D EM tomographic reconstructions. The correlated EM data permitted us to visualize RyRs on underlying sub-cellular membranes, allowing for more precise discrimination between junctional and non-junctional RyRs. Consistent with previous reports, most RyR labeling was associated with couplons, showing that these RyRs were primarily involved in E-C coupling. RyRs have been localized at junctions on thin resin sections via immunogold labeling, but the silver enhancement of colloidal gold as well as the low resolution of thin section TEM was not ideal for identifying feet structures [Salnikov et al., 2009]. Thus for the first time, we demonstrate the successful colocalization of immunolabeled RyRs with electron dense “feet” structures in dyadic junctions identified in EM tomograms. This not only establishes the efficacy of the antibodies, but also confirms the identity of these electron dense structures to be RyRs. However, not all feet structures identified within the cleft were associated with fluorescent labeling. This is most likely because the fluorescent signal was out of the plane of focus due to the differing axial locations of RyRs and, on account of poor localization, was discarded during STORM data rendering. Additionally, as

mentioned in Chapter 2 some antibody labeling may have been lost during EM sample preparation.

We report that approximately one-fifth of the fluorescent signal was found to be outside of couplon junctions. This value is comparable to the previously reported 16% in rats reported using diffraction limited confocal microscopy [Jayasinghe et al., 2009]. A significant proportion of the non-junctional RyRs were observed at the SR-mitochondrial cleft. The functional contribution of these non-junctional RyRs to E-C coupling varies based on their location with respect to couplons as well as other organelles such as the mitochondria. Non-junctional RyRs that are in close proximity to a dyadic cleft and that share the same SR Ca pool are more likely to behave as secondary amplification systems during E-C couplin, whereas RyRs within the SR-mitochondrial cleft most likely play a role in SR-mitochondrial communication. Their close association to the outer mitochondrial membrane suggests that these RyRs play a role in local Ca transfer to the mitochondria during E-C coupling to synchronize ATP production with the needs of muscle contraction. The tethers identified in the tomogram most likely create a microdomain of high Ca between the SR and mitochondria, facilitating the local control of Ca between the RyRs and mitochondrial Ca uptake sites. Understanding the spatial relation between SR, the mitochondrial surface, and RyRs is crucial to evaluating the relative contribution of local SR-mitochondrial Ca signaling and global Ca to the control of mitochondrial Ca uptake in cardiomyocytes.

Additionally, with the development of high resolution LM and EM techniques, detailed structural data are now available for the physiological modeling of Ca sparks in cardiomyocytes. Hake and colleagues were the first to

create a detailed simulation of a partial calcium spark in CRUs using computational geometries obtained from electron tomographic volumes [Hake et al., 2014]. However, like most 3D models, theirs was lacking in the localization of key proteins, such as RyRs, that structurally and functionally contribute to Ca spark propagation [Stern et al., 2012; Hake et al., 2014]. Thus, such simulations are limited due to the lack of structural data with protein localization. Such information is necessary to develop realistic models of Ca spark dynamics. Thus, the correlated LM-EM analyses reported in this chapter are the first step towards combining the molecular localization of LM with the high resolving power of EM to identify RyRs on cardiac ultrastructure. These techniques will, for the first time, allow for the generation of models that explore the relationship between subcellular Ca dynamics and the spatial organization of E-C coupling molecules using realistic geometric maps.

This chapter, in part, is a reprint of the material as it appears in Journal of Molecular and Cellular Cardiology, 2013. Das T, Hoshijima M. The dissertation author was the primary investigator and author of this paper. This chapter, in part, is currently being prepared for submission for publication of the material. Das T, Hoshijima M. The dissertation/thesis author was the primary investigator and author of this material.

Chapter 4:

E-C Coupling Molecule Compartmentation II:

L-type Calcium Channel, Sodium-Calcium Exchanger and Caveolin

4.1. E-C coupling

The ubiquitous second messenger Ca is essential for E-C coupling and subsequent myofilament contraction. Ion channels in the plasma membrane work in harmony to maintain the membrane potential at a steady state of about -90 mV. Action potentials conducted from neighboring cells via gap junctions open Na voltage-gated channels, flooding the cell with Na ions and depolarizing it. Next, Ca enters the into the junctional membrane space through depolarization-activated LTCCs, which triggers Ca release from the RyRs. The released Ca then binds to troponin C, initiating contraction. For relaxation to occur, the cytosolic Ca level needs to lower, thereby causing Ca to disassociate from the myofilaments. Thus, during relaxation, Ca is removed from the cytosol via the NCX, PMCA, SERCA mitochondrial uniporter, and Ca buffers. NCX and PMCA pump the Ca back into the extracellular space, whereas SERCA restores the SR Ca concentration.

Fig. 4.1 is a simple illustration of all the components and steps involved in E-C coupling. The sarcolemma and SR membrane are the main sites for Ca exchange via pumps and ion channels. These membranes are structurally specialized to organize the ion channels for functional E-C coupling. Sarcolemmal invaginations in the form of T-tubules couple with the SR, creating specialized microdomains for CICR between the LTCCs and RyRs.

Thus, the first step towards investigating the functional roles of ion channels in in E-C coupling lies in understanding protein localization in relation to the dyadic cleft. Accordingly, this chapter will begin with a review of the chief proteins involved in E-C coupling, with a focus on the current state of knowledge regarding their organization (Fig. 4.2). Unlike RyRs, most of these proteins are

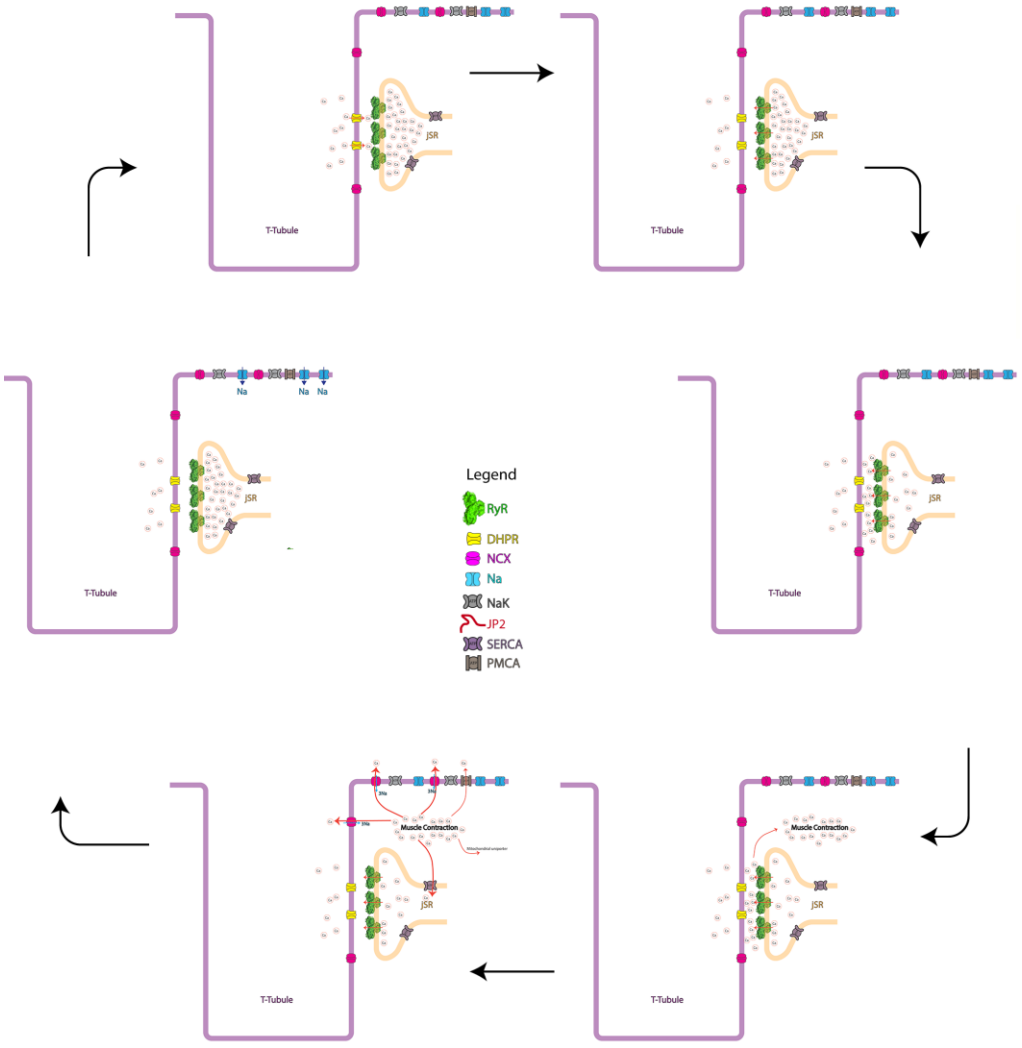

Figure 4.1. : E-C coupling process. Na voltage-gated channels open in response to the action potential flooding the cell with Na ions, depolarizing the cell. Next, Ca enters into cell via LTCCs, which triggers Ca release from the RyRs. The released Ca binds to troponin C initiating contraction. For relaxation NCX and PMCA pump the Ca back into the extracellular space where as SERCA restores the SR Ca concentration.

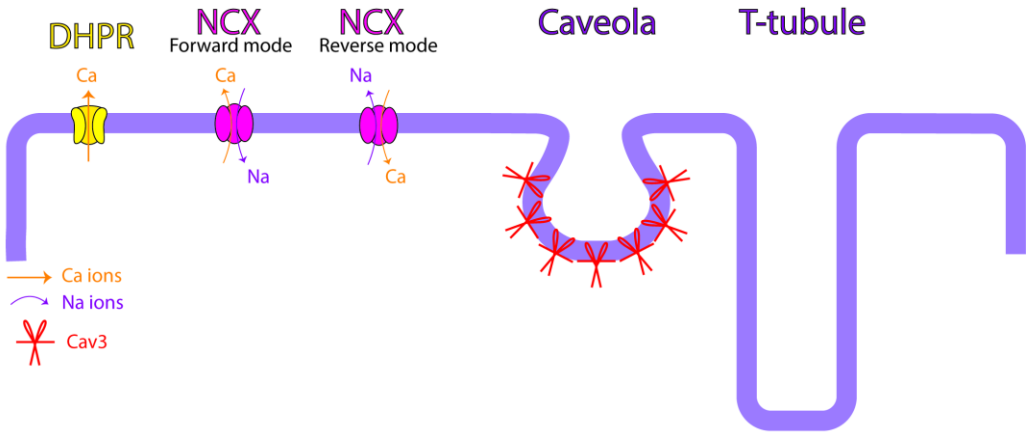

Figure 4.2. : Illustration of DHPR/LTCC, NCX, and Cav 3 localization in Caveolae.

indistinguishable from other transmembrane proteins in EM micrographs, and, as a result, are harder to characterize.

4.2. L-Type Ca channel (LTCC)

4.2.1. LTCC function

LTCCs are voltage-gated Ca channels located on the sarcolemma that initiate E-C coupling by allowing an influx of Ca ions across the sarcolemma. They are also referred to as dihydropyridine receptors (DHPRs), owing to their unique pharmacological sensitivity to dihydropyridine agents, a fact that was critical to their identification and isolation [Kanngiesser et al., 1988]. The predominant isoform in ventricular cardiac cells is Cav 1.2, which is a multimeric protein with a voltage sensing and pore-forming subunit Cav 1.2 (α_1) and auxiliary subunits (α_2, δ, β and delta) that are involved in modulating gating, trafficking and response to stimuli. These receptors activate at a membrane potential of -30 mV, and Ca flows along an electrochemical gradient into the cell. The Ca current declines over time as a result of voltage-dependent and calcium-dependent inactivation processes [Tseng and Boyden, 1989].

4.2.2 LTCC organization

As mentioned previously, LTCCs are indistinguishable from other transmembrane proteins in EM micrographs. As a result, all EM analyses have used immunogold labeling of thin sections to identify LTCCs in micrographs. Although useful, limited antibody penetration and spurious gold enhancement create many false positives. Conventional immunofluorescence studies have revealed that ~75% of these receptors form clusters in close association with

RyRs within couplons [Sedarat et al., 2000; Song et al., 2006; Scriven et al., 2010]. Functional analyses have confirmed that such specialized spatial coupling is essential for both CICR from RyRs and the calcium-dependent inactivation of the LTCCs for E-C coupling. LTCC organization within the couplon is still not clear, but diffraction-limited colocalization studies suggest that LTCCs cluster in the center of the RyR clusters for efficient CICR [Scriven et al., 2010]. Extra-dyadic LTCCs, on the other hand, localize outside couplon structures in specialized microdomains, such as caveolae and lipid rafts, as demonstrated by immunofluorescence and immunogold microscopy [Scriven et al., 2005; Balijepalli et al., 2006]. They are involved in signal transduction pathways such as hypertrophic signaling as well as protein recycling [Simons and Ikonen , 1997; Maxfield, 2002; Scriven et al., 2005; Balijepalli et al., 2006; Partons and Simons, 2007; Best and Kamp, 2012]. In mammalian cardiomyocytes, it has been estimated that ~4-10 RyRs associate with a LTCC receptor [Bers, 2002].

4.3. Sodium- Ca exchanger (NCX)

4.3.1. NCX function

The NCX was first discovered in cardiomyocytes and the squid axon [Reuter and Seitz, 1968; Baker et al., 1969]. It exists as three isoforms (NCX 1, NCX 2, NCX 3) with the splice variant NCX 1.1 being highly expressed in the heart. It is a secondary active transporter localized on the sarcolemma, which exchanges three Na ions for one Ca ion either into the cell or out of the cell depending on the membrane potential and electrochemical gradient. Whereas LTCCs are the major sarcolemmal influx pathway for Ca in cardiomyocytes, the

NCXs manage myoplasmic Ca by acting as the primary efflux pathway across the sarcolemma during the decay phase of the intracellular Ca transient.

4.3.2. NCX organization

Consistent with its primary function, immunofluorescence and immunoelectron microscopy have shown the NCX to be distributed in clusters on the sarcolemma, including the intercalated disks, with the highest density of labeling primarily found along the T-system [Frank et al., 1992; Scriven et al., 2000; Thomas et al., 2003; Scriven et al., 2005; Dan et al., 2007; Jayasinghe et al., 2009; Jon et al., 2011]. The reversible nature of the exchanger, along with evidence from cardiac specific NCX knockout (KO) mice, suggests that NCXs can play a role in initiating E-C coupling [Henderson et al., 2004; Pott et al., 2005]. This implies that a sub-population of NCX molecules must be located close enough to couplons to impact their functioning. Whether the exchangers are located within the couplons or on the periphery of the couplons is still up for debate. Immunofluorescence studies using diffraction-limited microscopy have reported conflicting RyR and NCX colocalization values ranging from 3-10% to ~42%. [Dan et al., 2007; Scriven et al., 2000b; Jayasinghe et al., 2009]. Triple labeling experiments of RyRs, LTCCs, and NCX in atrial cells demonstrated a significant number of triplets, accounting for ~13% of the total RyR and NCX labeling [Schulson et al., 2011]. The tighter localization of LTCCs with RyRs than NCX with RyR-LTCCs suggests that NCXs could possibly be localized on the edge of the RyR clusters. Additionally, it has also been hypothesized that a sub-population of NCXs associate with Caveolin 3 (Cav 3). Interestingly, LM studies by different groups have reported conflicting degrees of localization between

NCX and Cav 3 [Kieval et al., 1992, Frank et al., 1992; Thomas et al., 2003]. Thus, further studies are required to clarify the localization of NCX molecules as well as their functional implications in cardiomyocytes.

4.4. Caveolin (Cav)

4.4.1 Cav function

Caveolins are integral membrane proteins (21-24 KDa) that form the principal structural and regulatory component of bulb-shaped microdomains in the plasma membrane called caveolae [Rothberg et al., 1992; Glenney and Soppet , 1992; Glenney , 1992; Dupree et al.,1993] .Caveolins exist in three isoforms: Cav 1, Cav 2, Cav 3. Cav 1 is expressed in multiple cell types, including endothelial, epithelial and smooth muscle cells, whereas Cav 3 is the predominant isoform expressed in skeletal and cardiac tissue [Rothberg et al., 1992; Song et al., 1996; Smart et al., 1999]. Cav 3 knockdown and KO models were lacking in cardiac caveolae, confirming that Cav 3 is essential for the formation of caveolae in cardiomyocytes [Balijepalli et al., 2006; Galbiati et al., 2001). The formation of these structures is critical for the sub-cellular localization of signaling molecules, such as upstream transmembrane receptors, intermediate kinases, and ion channels, forming macromolecular complexes for highly localized and efficient signaling.

4.4.2. Cav 3 organization

Cav 3 has been shown to associate transiently with T-tubules during development in skeletal muscle, suggesting that it may play a role in the biogenesis of the T-tubule system in cardiomyocytes [Parton et al., 1997; Carozzi

et al., 2000; Lee et al., 2002]. Immunoprecipitation studies and diffraction-limited immunofluorescence colocalization analyses have shown that several sarcolemmal ion channels critical to E-C coupling, such as LTCCs, Ca-ATPase, Na channels, NCX and NaK, are enriched within caveolae. As described previously, there is strong evidence supporting the localization of LTCCs with Cav 3 within caveolae, whereas NCX association is still unclear [Barouch et al., 2002; Wang et al., 2005; Balijepalli et al., 2006; Warrier et al., 2007]. Recent super-resolution studies and EM tomography analyses have confirmed previous diffraction-limited reports of RyRs colocalizing with Cav 3 [Scriven et al., 2010; Wong et al, 2012]. However, the increased resolution afforded by these new techniques showed that very few RyR clusters were found to couple with caveolae. Although Cav 3 was widely distributed throughout the T-system, only a small fraction of RyRs colocalized with Cav 3. The structural and functional role of Cav 3 in T-systems is still unclear and requires further investigation to elucidate its role in E-C coupling.

Therefore, in this chapter, the CLEM technique developed in Chapter 2 will be extended to investigate the cellular localization of the E-C coupling ion channels, NCXs, and LTCCs, which are the main pathways for Ca exchange across the sarcolemma. Additionally, we examine the organization of Cav 3, a protein that has been implicated to co-localize with RyRs, LTCCs and NCXs to some degree outside of dyadic regions [Bossuyt et al., 2002; Scriven et al., 2005; Asghari et al., 2009; Jayasinghe et al., 2009; Scriven et al., 2010; Wong et al., 2013].

4.5. Methods

Please refer to Section 2.3 in Chapter 2 for the methods. The same protocol was followed with the following changes:

1) In addition to mice, tissue was collected from adult hamsters (12-13 months) for Cav 3 localization.

2) The primary antibodies used were rabbit polyclonal anti-Cav 1.2 (L-type of Voltage-Gated Ca channel) antibody (ACC-003, Alomone Labs, 1:200), mouse monoclonal anti-NCX antibody (R3F1, Swant, 1:100), and rabbit polyclonal anti-Cav 3 antibody (ab2912, Abcam, 1:200).

3) Lastly, reduced osmium was used to process the tissue samples.

4.6. Results

The CLEM method developed in Chapter 2 facilitates the identification and high resolution localization of E-C coupling proteins that are otherwise indistinguishable at the EM level. For proteins with readily available antibodies, LM-targeted molecular labeling was used to identify the protein of interest on EM maps of cellular architecture, as described below.

4.6.1. Correlated in-resin STORM and SEM imaging of LTCCs in sarcolemmal sub-domains

STORM-SEM imaging facilitates the identification and localization of E-C coupling proteins across whole cells. STORM imaging of LTCCs demonstrated receptor distribution in the interior of the cell as well as at the edge of the cell. Upon correlation, the localization of LTCC immuno-fluorescence signals was found to be associated with the sarcolemma, including the T-system of

cardiomyocytes (Fig. 4.3). Most LTCC signals were localized in association with the T-system membrane at the Z–lines, and their majority was in dyadic clefts. Only a minor population of LTCCs appeared to associate with T-systems lacking SR associations. Fig. 4.3 shows the localization of possible extra-dyadic LTCCs within caveolar structures forming in the sarcolemma.

4.6.1. Correlated in-resin STORM and EM tomography of LTCCs in sarcolemmal sub-domains

The localization of LTCC-labeled molecules on 3D cellular reconstructions was achieved using 3D EM tomography (Fig. 4.4). All LTCC labeling was observed to associate with either the sarcolemma or the T-tubules. In Fig. 4.4, LTCC molecules can be seen colocalizing with the electron dense RyR feet within the dyadic cleft. Consistent with STORM-SEM imaging, LTCCs localize towards the interior of the cleft. Along the sarcolemma, LTCC molecules were localized within caveolae and peripheral junctional domains.

4.6.2. Correlated in-resin STORM and SEM imaging of NCX in sarcolemmal sub-domains

STORM imaging of NCX immunolabeling revealed a punctate distribution of NCX following the T-system. NCX density was higher along the T-system in the interior of the cell than along the surface sarcolemma (Fig. 4.5). NCX channels were also distributed along both the transverse as well as axial elements of the T-system. Most NCX signals located on the T-system forming junctional domains with SR were localized outside of the dyadic cleft , whereas

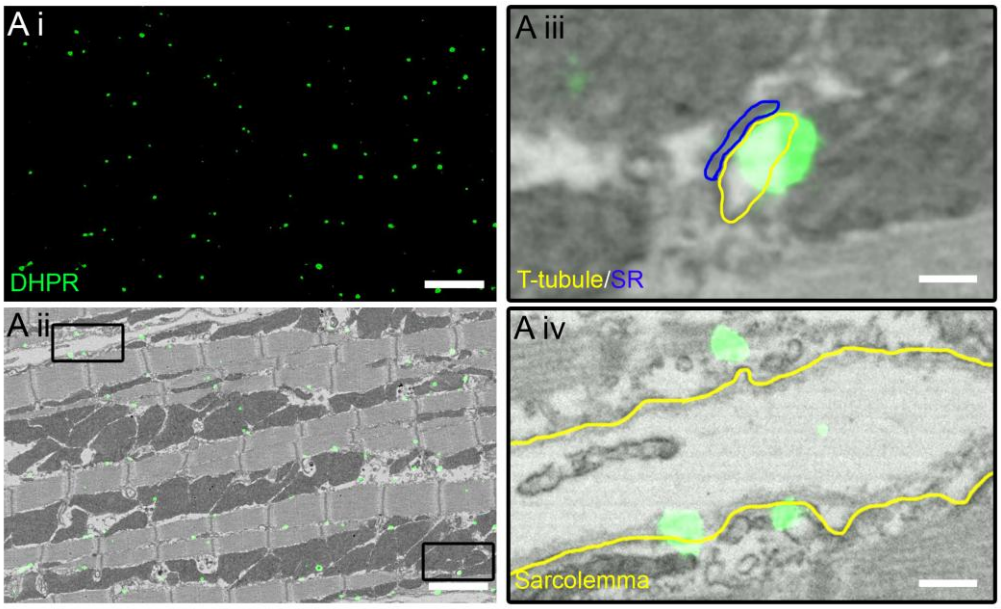

Figure 4.3. : Correlated STORM data and SEM of immunolabeled DHPR in cardiac mouse tissue sections processed with reduced osmium. The region of interest is located using diffraction-limited microscopy followed by subsequent STORM imaging (Ai). The section is post stained and the same area is imaged using SEM at low magnification. 100nm Tetraspeck™ are used to correlate the STORM image with SEM at low magnification (Aii). (Aiii, Aiv) are magnified views of the jSR (blue), T-tubule and sarcolemma (yellow) with correlated DHPR (green) fluorescence from boxed regions illustrated in (Aii). Correlated DHPR signal is localized within the junctional domain on the T-tubule (Aiii) and along the sarcolemma as expected (Aiv). Scale Bars 2um (Ai, Aii), 100nm (Aiii, Aiv).

Figure 4.4. : Correlated STORM data and EM tomography of immunolabeled DHPR in cardiac mouse tissue sections processed with reduced osmium. The region of interest is located using diffraction-limited microscopy (A) followed by subsequent STORM imaging (B). The same section is imaged at 0 tilt using a TEM at low magnification (C). 100nm Tetraspeck™ beads are used to correlate the STORM image with the low magnification TEM micrograph (D). A region is identified with DHPR fluorescence labeling (boxed region in D) and is imaged for EM tomography. DHPR (green) fluorescence (B) can be identified on the SR, and within the dyadic cleft at Z-lines in individual sections of the tomogram (E). (F-I) are magnified views of the red-boxed region in (E). Dense feet-like RyR can be identified in (E) which cololocalizes with DHPR fluorescence (G). The T-tubule (yellow), jSR (blue) and RyR (red) are manually segmented in the tomogram (H) and correlated with green fluorescent STORM data in an individual tomogram slice (I). Scale bars 2um (A, B, C,D), 1um (E), 100nm (F, G, H, I).

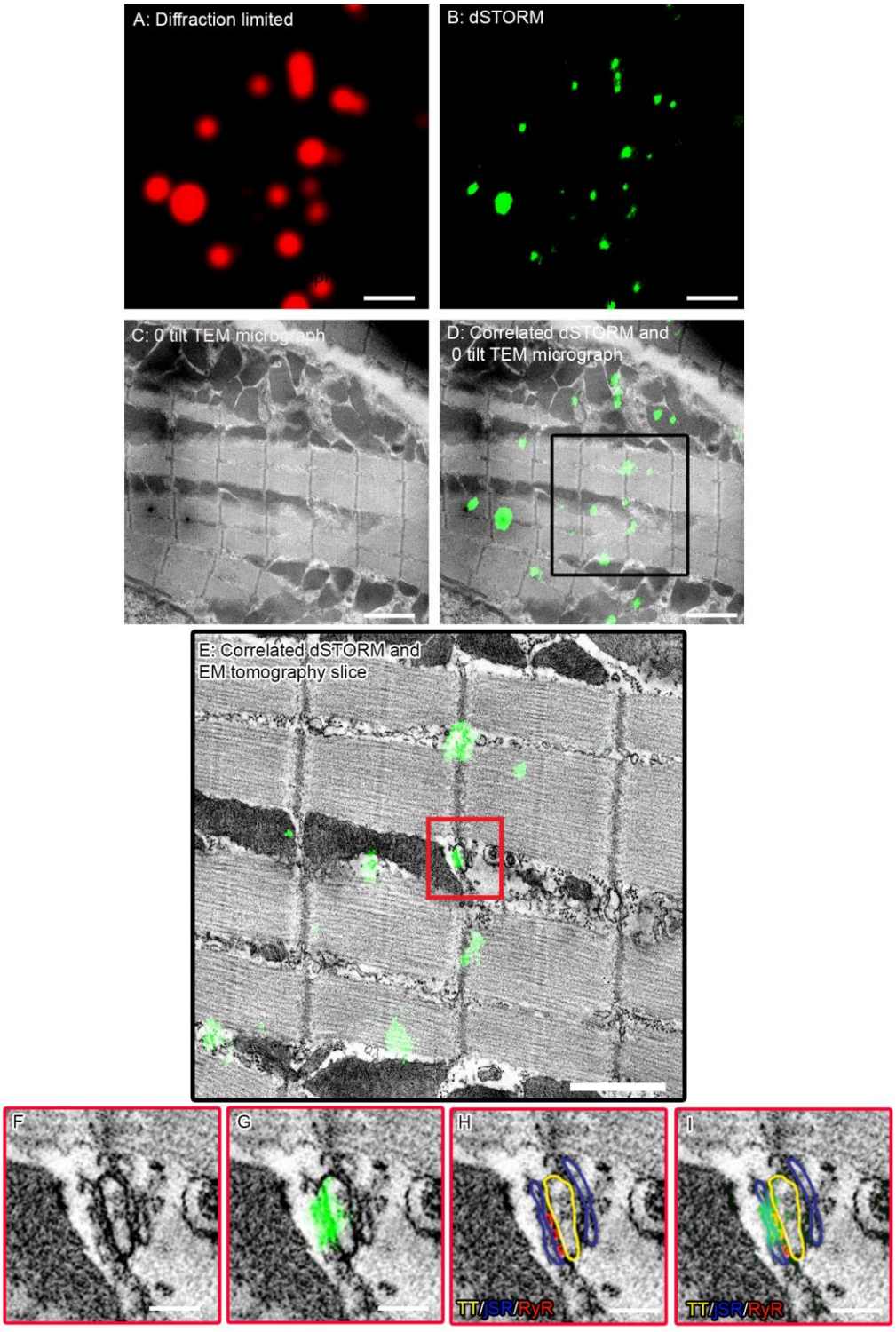
A: Diffraction limited
B: dSTORM
C: 0 tilt TEM micrograph
D: Correlated dSTORM and
0 tilt TEM micrograph
E: Correlated dSTORM and
EM tomography slice
F
G
H
I
TT/SR/RyR
TT/SR/RyR

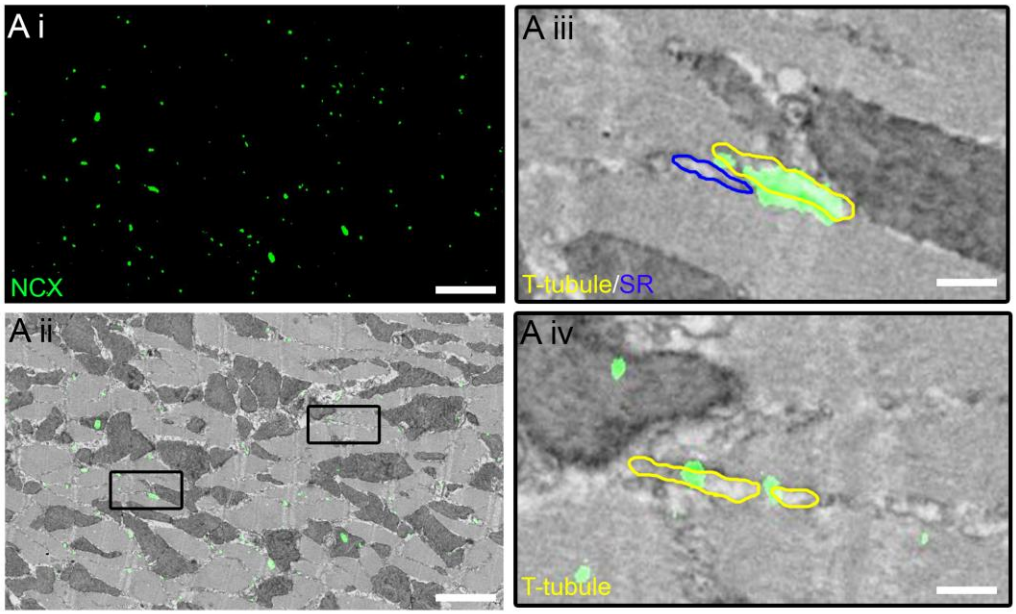

Figure 4.5. : Correlated STORM data and SEM of immunolabeled NCX in cardiac mouse tissue sections processed with reduced osmium. The region of interest is located using diffraction-limited microscopy followed by subsequent STORM imaging (Ai). The section is post stained and the same area is imaged using SEM at low magnification. 100nm Tetraspeck™ are used to correlate the STORM image with SEM at low magnification (Aii). (Aiii, Aiv) are magnified views of the jSR (blue) and T-tubule (yellow) with correlated NCX (green) fluorescence from boxed regions illustrated in (Aii). Correlated NCX signal is found to be primarily localized in the T-system along both transverse and axial tubules (Aiv) .NCX labeling associated with couplons was mostly localized at the periphery of the dyad (Aiii). Scale Bars 2um (Ai, Aii), 100nm (Aiii, Aiv).

the majority of the NCX channels along the surface sarcolemma did not associate with the sub-sarcolemmal SR or caveolae.

4.6.3 Correlated in-resin STORM and SEM imaging of Cav 3 in the sarcolemma

Since both RyRs and LTCCs were observed to associate with caveolar structures to some degree, and it is debated whether NCX does the same, I investigated the localization of Cav 3, the principal structural component of cardiac caveolae, which is expressed in T-tubules as well. STORM imaging demonstrated a striated, punctate labeling similar to the T-tubule distribution in cardiomyocytes. The results of STORM imaging show that Cav 3 is distributed along the edge of the cell as well as in the cell's interior (Fig. 4.6). After superimposing the STORM data onto the SEM image, fluorescent signal can be seen localized on the T-tubule membranes in the interior of the cell as well as along the sarcolemma on caveolar structures.

4.6.4 Correlated Array tomography for 3D CLEM

To investigate the organization of Cav 3 within a complete 3D caveola, we turned to 3D correlated LM-EM. Although EM tomography offers better axial resolution, it lacks 3D LM data. Serial 80 nm sections were imaged using STORM followed by SEM. After LM-EM correlation, consecutive sections were aligned by patch cross-correlation to generate 3D CLEM volumes (Fig. 4.7). Representative slices of one such volume are shown in Fig. 6. The caveolae in each section were segmented and meshed to generate a 3D model, which is shown overlaid with STORM data to demonstrate how Cav 3 localizes on the

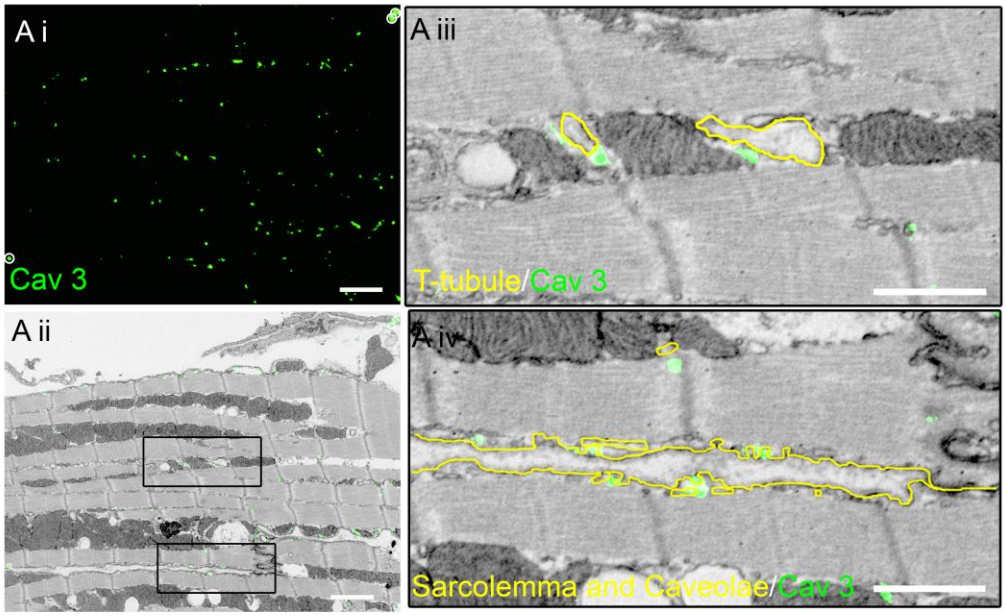

Figure 4.6. : Correlated STORM data and SEM of immunolabeled CAV 3 in cardiac hamster tissue sections processed with reduced osmium. The region of interest is located using diffraction-limited microscopy followed by subsequent STORM imaging (Ai). The section is post stained and the same area is imaged using SEM at low magnification. 100nm Tetraspeck™ are used to correlate the STORM image with SEM at low magnification (Aii). (Aiii, Aiv) are magnified views of the sarcolemma and T-tubule (yellow) with correlated Cav 3 (green) fluorescence from boxed regions illustrated in (Aii). Cav 3 (green) can be identified on T-tubules at the Z-lines (Aiii) and on caveolae (yellow) on the sarcolemma in (Aiv). Scale Bars 2um (Ai, Aii), 1um (Aiii, Aiv).

Figure 4.7. : Correlated Cav 3 array tomography in cardiac hamster tissue sections. 4 consecutive 80nm thin sections are imaged using STORM followed by SEM (Ai, Bi, Ci, Di) and correlated. (Aii, Bii, Cii, Dii) are magnified views of caveolae (yellow) on the plasma membrane with correlated CAV3 (green) fluorescence from the boxed regions illustrated in (Ai, Bi, Ci, Di). Using patch cross-correlation, the consecutive sections are aligned into a 3D volume. The caveolae (yellow) is segmented in each section and a surface mesh model is shown in correlation with RyR fluorescence data at corresponding z positions (Aiii, Biii, Ciii, Diii). Scale Bars 2um (Ai, Bi, Ci, Di), 1um (Aii, Bii, Cii, Dii), 0.75um (Aiii, Biii, Ciii, Diii).

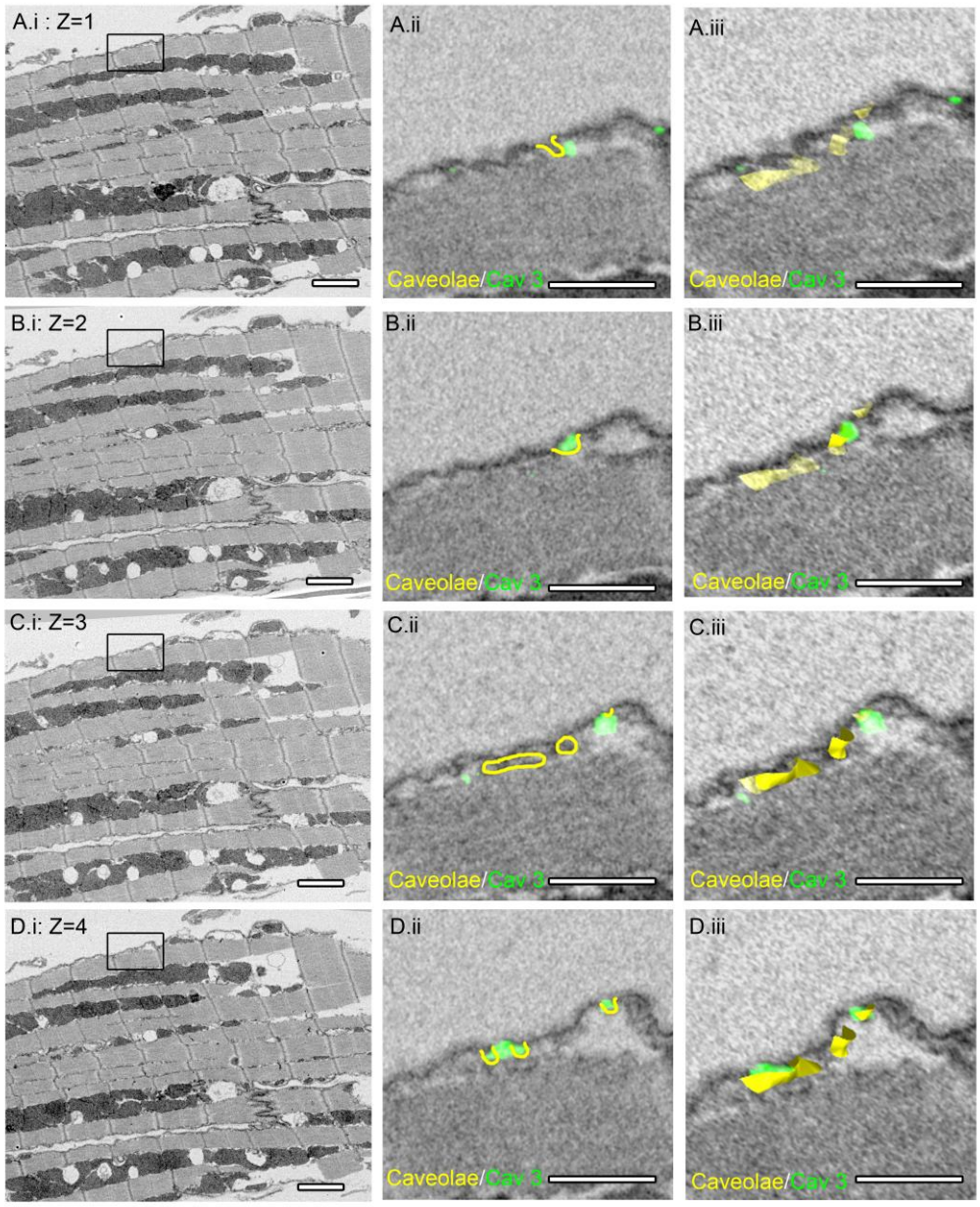
A.i : Z=1
A.ii
A.iii
Caveolae/Cav 3
Caveolae/Cav 3
B.i: Z=2
B.ii
B.iii
Caveolae/Cav 3
Caveolae/Cav 3
C.i: Z=3
C.ii
C.iii
Caveolae/Cav 3
Caveolae/Cav 3
D.i: Z=4
D.ii
D.iii
Caveolae/Cav 3
Caveolae/Cav 3

caveolar structure. Fig 6 Aii-Dii depicts a close-up view of a few caveolae segmented in yellow.

4.7. Discussion

The punctate labeling of LTCCs along the edge and interior of the cell depicted in STORM images is consistent with previous findings that LTCCs are distributed in clusters throughout the sarcolemma. This was confirmed in correlated immunolocalization studies, which showed that all LTCC labels were associated with the sarcolemma, including the T-system, in SEM images. Most of the LTCCs were confined to the inter-membrane space between the sarcolemma and jSR, creating the molecular architecture essential for CICR during E-C coupling. Limitations in LM-EM correlation precision limited our ability to determine where LTCCs are exactly localized in the dyadic cleft. However, based on observations from the data collected here, LTCCs, unlike NCXs, tend to localize more towards the interior of the dyadic cleft. The extra-dyadic LTCCs that were observed in association with caveolae suggest that these channels most likely colocalized with Cav 3, the main scaffolding protein in caveolae. This is consistent with co-labeling immunoelectron studies of LTCCs and Cav 3 in neonatal ventricular myocytes [Balijepalli et al., 2006; Shibata et al., 2006]. Additionally, extra-dyadic LTCCs were not associated with the jSR, suggesting that this sub-population of LTCCs may have functional roles other than regulating Ca concentrations during E-C coupling.

The morphology of NCX labeling observed in STORM images was comparable to diffraction-limited reports from previous studies [Jayasinghe et al., 2009]. Similar to LTCC labeling, the majority of the NCX labeling was associated

with the T-system in the interior of the cell. However, unlike LTCC organization, most NCX clusters on T-tubules forming junctional domains with jSR were localized on the edge of the dyadic cleft. Their close proximity (< 150 nm) to the junctional domain suggests that those channels may play a role in E-C coupling. On the other hand, the majority of the NCX channels along the sarcolemma did not associate with caveolar structures or jSR, implying that these channels most likely manage myoplasmic Ca concentrations. Interestingly, LM studies by different groups have reported varying degrees of localization between NCXs and Cav 3 [Kieval et al., 1992, Frank et al., 1992; Thomas et al., 2003]. Although we report little or no localization of NCXs in caveolar structures, two-color STORM-SEM with NCX and Cav 3 co-labeling is a potential approach to resolve the debate over whether NCX and Cav 3 colocalize.

The distribution of Cav 3 labeling was comparable to that reported by diffraction-limited and super-resolution studies [Scriven et al., 2010; Wong et al., 2013]. However, the localization was more punctate than continuous, as was observed in whole cell STORM images. This is most likely because we are restricted to imaging only an 80-100 nm thickness of the tissue. Additionally, antibody loss during EM processing could contribute to the incomplete localization of Cav 3 in caveolae. As expected, Cav 3 labeling was observed to colocalize with the sarcolemma, including T-tubules and caveolae. Although Cav 3 was localized on the T-tubules, very few molecules were associated with the jSR. This is in accordance with recent STORM reports by Wong et al., which demonstrate only ~4% colocalization between RyR and Cav 3 labeling. Lastly, Cav 3 analyses were performed on hamster tissue, demonstrating the versatility and ease of applying this method to a range of proteins in different host species.

The knowledge of spatial information is critical for the generation of accurate physiological models of Ca sparks in cardiomyocytes. Most current models contain sufficient structural geometry but lack the localization of key proteins such as the RyRs, LTCCs and NCXs, which contribute to Ca spark propagation both structurally and functionally. Furthermore, there is increasing evidence that ultrastructural alterations to the TT-jSR junction contribute to the desynchronous Ca release seen in heart failure [Wei et al., 2010; Wu et al., 2012; Zhang et al., 2013]. Imaging studies using LM and fluorescent labeling have revealed the dissociation of RyR clusters from TTs and the reduced co-localization of LTCCs and RyRs during heart failure [Stern et al., 1992; Van Oort et al., 2011]. However, it is completely unknown where such dissociated ion channels localize in the cytoplasm, and the possibility that dyadic cleft remodeling alters the distribution of E-C coupling proteins such as RyRs within junctional clefts and between the cleft and non-cleft micro-domains has not been investigated. Thus, the techniques presented here provide us with a tool to visualize protein reorganization within the context of cellular remodeling, helping us to better understand the pathological changes that ultimately lead to the development of heart failure.

This chapter, in part, is a reprint of the material as it appears in Journal of Molecular and Cellular Cardiology, 2013. Das T, Hoshijima M. The dissertation author was the primary investigator and author of this paper. This chapter, in part, is currently being prepared for submission for publication of the material. Das T, Hoshijima M. The dissertation/thesis author was the primary investigator and author of this material.

Chapter 5:

Membrane Junctions and E-C Coupling Molecule Compartmentation, and Future Perspectives.

5.1. Junctophilin types and structure

Junctophilins are junctional complexes between the plasma membrane and sarcoplasmic reticulum that are responsible for mediating cross talk between cell surface and intracellular ion channels (Fig. 5.1). In mice, there are four subtypes: JP 1, JP 2, JP 3 and JP 4 [Takeshima et al., 2000]. JP1 was the first subtype to be identified after it was discovered in the jSR fraction of rabbit skeletal muscle [Takeshima et al., 2000]. JP2 is abundantly expressed in the heart and is localized within dyads. JP3 and JP4 are widely expressed in neurons [Nishi et al., 2003]. JP subtypes have a large cytoplasmic domain and share conserved sequences of 14 amino acid MORN motifs at the N-terminal, which are thought to mediate JP attachment to the sarcolemma. This is followed by an alpha helical region and a SR spanning C-terminal transmembrane segment [Takeshima et al., 2000].

5.2. Junctophilin function and organization

It has been hypothesized that JP2 keeps the plasma membrane and SR at a fixed distance of 12-15 nm, which is essential for proper CICR during E-C coupling (Rudy 2011). This is supported by a report from Takeshima and colleagues describing a deficiency of peripheral couplings in JP2 KO cardiomyocytes [Takshima et al., 2000]. The genetic ablation of *JP2 was found to result* in embryonic lethality, most likely arising as a result of the absence of cardiac contractility that occurs around embryonic day 10.5 due to the inability to form peripheral junctions. This established that JP2 is required in the embryonic heart for functional E-C coupling. Furthermore, the induced reduction of JP2 expression in cultured NRVMs resulted in a reduced T-tubule and jSR coupling

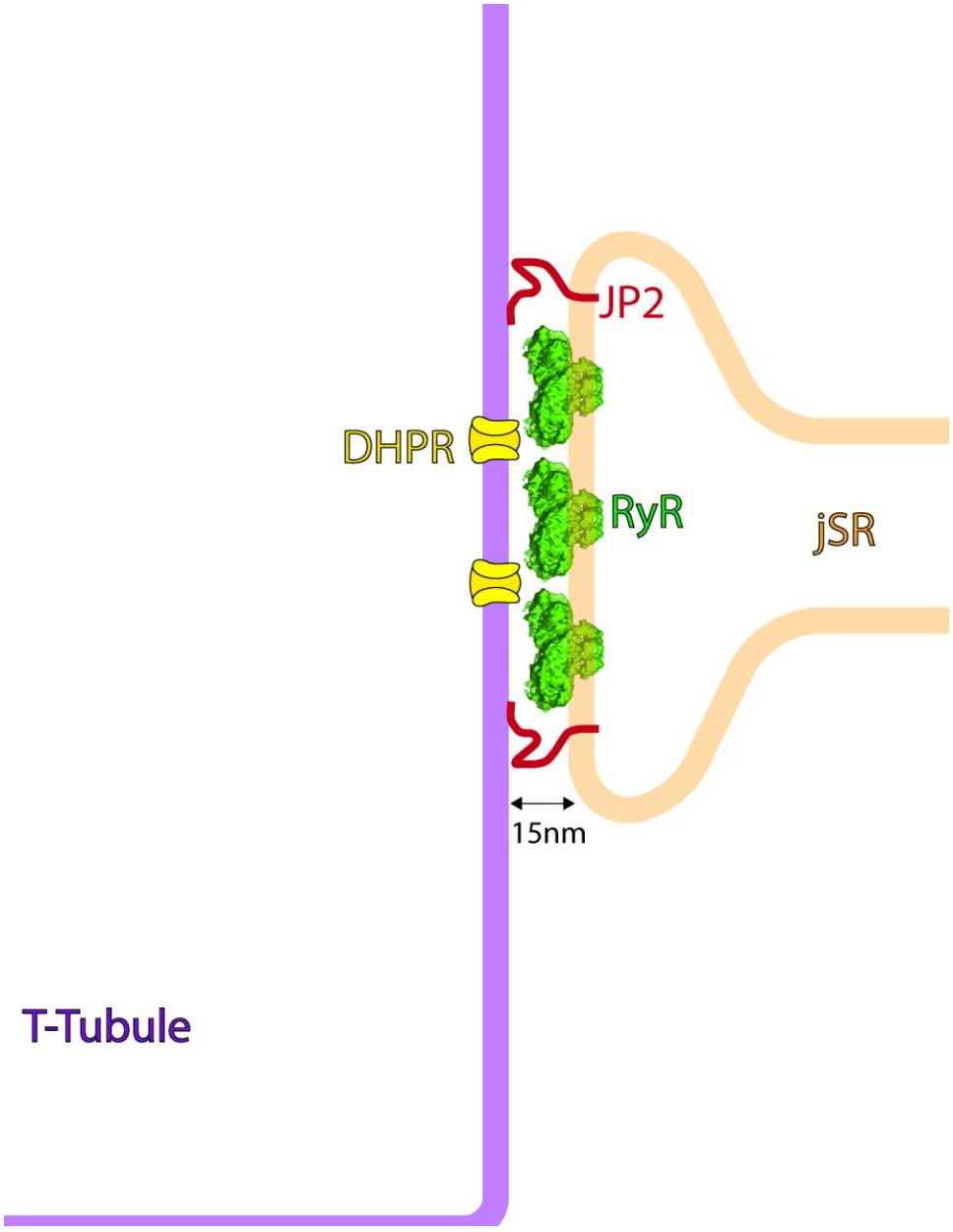

Figure 5.1. : Illustration of a junctional membrane complex maintained by junctophilin 2 (JP2). (CryoEM map of RyR1 channel (EMDB 1606) was uploaded from https://www.cgl.ucsf.edu/chimera/) [Pettersen et al., 2004].

area [Wu et al., 2012]. Similarly, JP2 gene silencing in AMCMs resulted in the loss of T-tubule integrity [Wei et al., 2010]. The shRNA-induced knockdown of JP in adult mice was found to result in sudden death due to acute heart failure [Wei et al., 2010; Van Oort et al., 2011]. Interestingly, although cardiac RyR expression levels were found to remain constant following JP knockdown, the whole cell E-C coupling gain and density of functional couplons were reduced [Van Oort et al., 2011]. Diffraction-limited LM and EM revealed the uncoupling of RyRs from the LTCCs and disrupted T-tubules, providing compelling evidence of the role of JP2 in stabilizing junctional membrane complexes.

Additionally, JP has been shown to co-immunoprecipitate with RyRs. It could potentially function as an allosteric regulator of RyR2 that impairs Ca dynamics in knockdown cells, leading to impaired Ca dynamics [Van Oort et al., 2011]. Recent studies also suggest that in addition to RyRs, JP molecules directly interact with caveolins and LTCCs forming a stable junctional complex between the membranes, thereby stabilizing the dyad and bringing about normal SR Ca release [Minamisawa et al., 2004; Phimister et al.,2007; Golini et al.,2011; Beavers et al., 2013]. Super-resolution imaging studies have reported that RyRs and JP2 highly colocalize in peripheral junctions after adding a 30 nm boundary zone around RyR clusters, suggesting that a subset of JP molecules are not interspersed among the RyRs but are instead located around the periphery of the clusters [Jayasinghe et al.; 2012]. Thus, further investigation is required to resolve the biological relationship of JP2 with RyRs in the formation and maintenance of functional E-C coupling microdomains.

5.3. Junctophilin and heart failure

In addition to the role it plays in the normal development of cardiac E–C coupling machinery, JP2 is an essential safeguard against cardiac stress. Evidence suggests that couplon remodeling in heart failure may be due in part to the loss and mislocalization of JP [Landstrom et al., 2007; Van Oort et al., 2011; Wu et al., 2012 Zhang et al. 2013; Zhang et al., 2014]. Loss of JP2 expression has been observed in rodent models of heart failure as well as in patients with hypertrophic cardiomyopathy [Minamisawa et al., 2004; Wei et al., 2010; Landstrom et al., 2011; Chen et al., 2012; Xie et al., 2012; Xu et al., 2012; Wu et al., 2012, Zhang et al., 2013, Wu et al., 2014]. Accordingly, the specific shRNA-induced knockdown of JP2 in mice caused sudden cardiac death due to acute heart failure [Van Oort et al., 2011]. Microtubule polymerization, calpain cleavage, and the up-regulation of microRNAs are some of the mechanisms proposed to be responsible for the downregulation of JP2 expression in heart failure [Xu et al., 2012, Zhang et al., 2013, Wu et al., 2014].

While structural changes to sub-cellular anatomy in JP2 downregulated models and heart failure models have been extensively studied using EM, it is much more challenging to study the accompanying ion channel reorganization. Diffraction-limited LM imaging following acute JP2 knockdown in adult mice demonstrated reduced colocalization of LTCCs and RyRs [Van Oort et al., 2011]. Similarly, LM imaging studies using fluorescent labeling have revealed the dissociation of RyR clusters from T-tubules and uncoupling of LTCCs from RyRs during heart failure [Wu et al., 2012]. Recent super-resolution observations by Munro and colleagues claim that JP knockdown is also accompanied by a reduction of superclusters, which are smaller and more spaced apart [Munro et al., 2014]. However, it is unclear whether this breakdown of clustering is confined

to junctional RyRs, non-junctional RyRs, or both. It is also unclear whether the reorganization of RyRs is in response to the loss of JP as a RyR anchor or due to the decoupling of T-tubules from the jSR. Thus, junctional membrane complex remodeling in response to JP loss could lead to RyR2 cluster disassembly and instability and affect the Ca release properties of SR. To understand how the downregulation of JP in response to cardiac stress leads to the development of heart failure, the remodeling of nanometer-tight RyR clusters in couplons and the accompanying changes in Ca dynamics need to be further investigated and computationally modeled.

Thus, in this chapter, I investigate the dynamic remodeling of couplons and the associated junctional and non-junctional RyR redistributions in response to JP knockout, which has been shown to lead to heart failure. The worsking hypothesis is that the dynamic disassembly of junctional RyR groups and the increase in non-junctional RyRs in response to lowering JP expression results in abnormal Ca transients.

5.4. Methods

Junctophilin KO Mice: Dr. Masahiko Hoshijima provided a new conditional JP2 deletion mouse line for adult JP2 removal using αMHC-MCreM mice for cardiac inducible gene deletion. Both groups (n=3 for control and n=3 JPKO) were treated with tamoxifen (~30mg/kg) for five days, and then the corresponding tissues were collected as described in Section 2.3 in chapter 2. Both control and KO tissues were processed in parallel with polyclonal anti-RyR antibodies as described in Section 2.3, and then treated with reduced osmium for EM processing.

5.5. Results

5.5.1. Diffraction-limited imaging

AMCMs isolated from JPKO and control animals were fixed, immunolabeled, and imaged in a confocal microscope. As expected, the RyR distribution and T-tubule organization demonstrated a striated pattern typical to Z-line organization in the control cells. T-tubule labeling was continuous with elements in the longitudinal and axial directions. RyR and T-tubule labeling coloocalized highly, as demonstrated in Fig 5.2C. On the other hand, the demonstrated JPKO labeling pattern was more punctate for both RyRs and T-tubules. T-tubule labeling was discontinuous and less periodic than in the control. The reduced colocalization of RyRs and T-tubule labeling is evident in Fig 5.2F.

5.5.2. Correlated STORM and SEM of RyRs in junctions and non-junctional cytoplasm

Correlated STORM-SEM imaging was used to allow the identification of RyR cluster distributions on associated sub-cellular membranes across the whole cell (Fig. 5.3). The application of super-resolution imaging to RyRs in JPKO demonstrated a similar Z pattern staining to the control. However, further examination of the underlying membrane architecture using SEM demonstrated significant remodeling of T-tubules and SR. As a result, a significant population of junctional RyRs was observed to be disassociated from the T-tubule. Taking advantage of the geometric cellular map provided by SEM imaging, we classified the clusters into four categories. RyR clusters located at the interface between the sarcolemma (including the T-system) and closely coupled to the relatively flat junctional cistern of the SR (junctional cleft) were classified as junctional RyRs

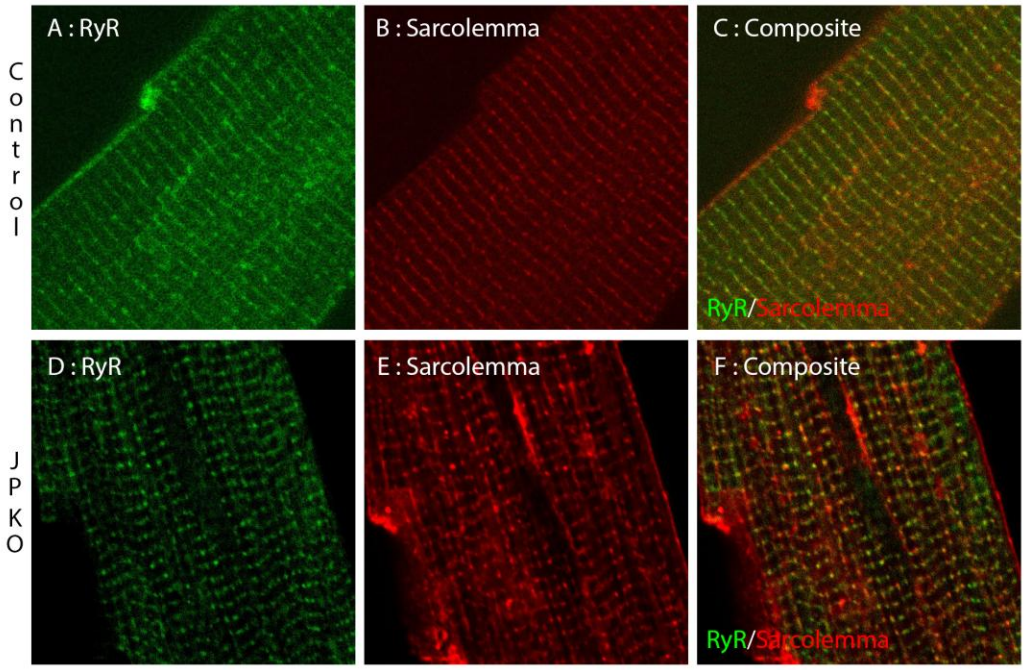

Figure 5.2. : Diffraction-limited imaging of RyR (A,D) and sarcolemma (B,E) in control and JPKO cardiomyocytes , respectively. JPKO demonstrates reduced colocalization of RyR with T-tubules in JPKO (E) than the control (C).

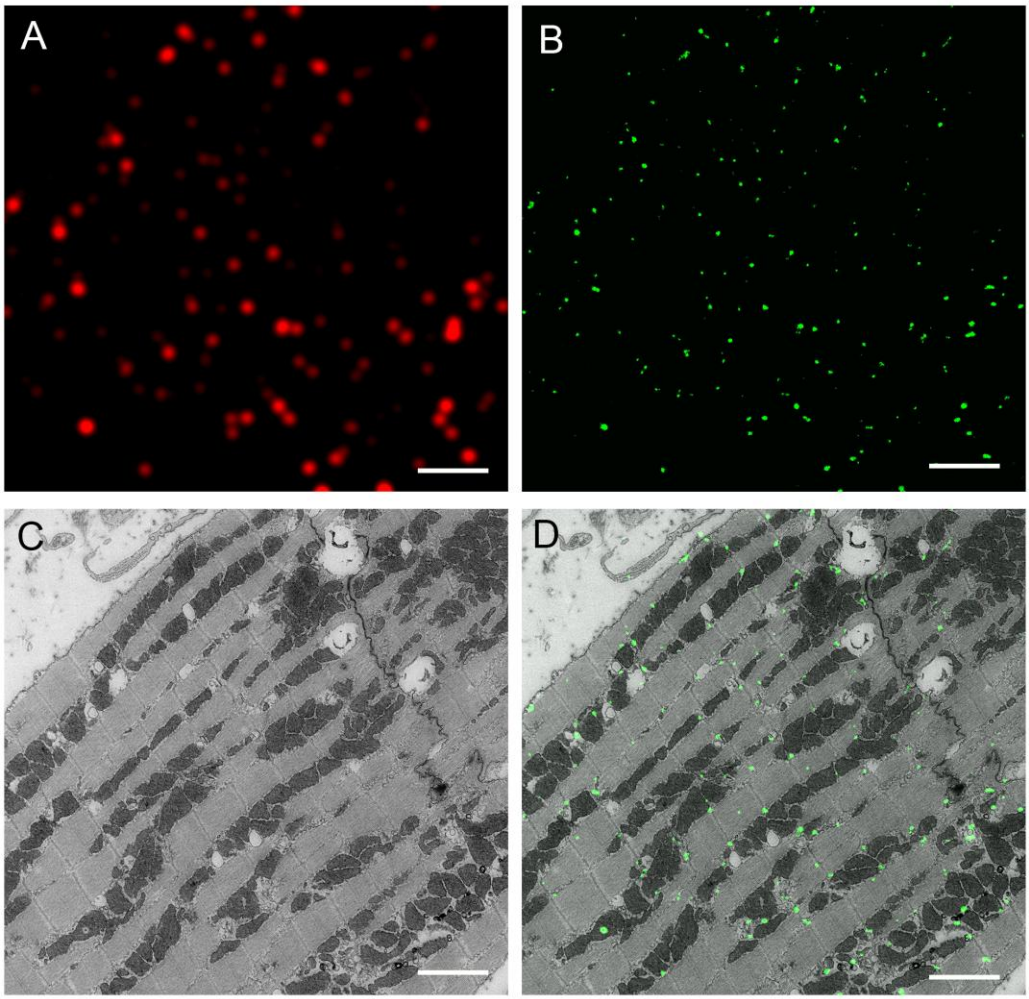

Fig 5.3. : Correlated in-resin STORM data and SEM of RyR with RyR –Ax 647 in cardiac JPKO mouse tissue processed with reduced osmium. The region of interest is located using diffraction limited microscopy (A) followed by subsequent STORM imaging (B). The section is post stained and the same area is imaged using SEM at low magnification (C). 100nm Tetraspeck™ are used to correlate the STORM image with the SEM image (D). Although RyR labeling can be identified at typical Z-line locations, the underlying junctional membranes are disorganized and uncoupled. Scale Bars 2um (A, B, C, D).

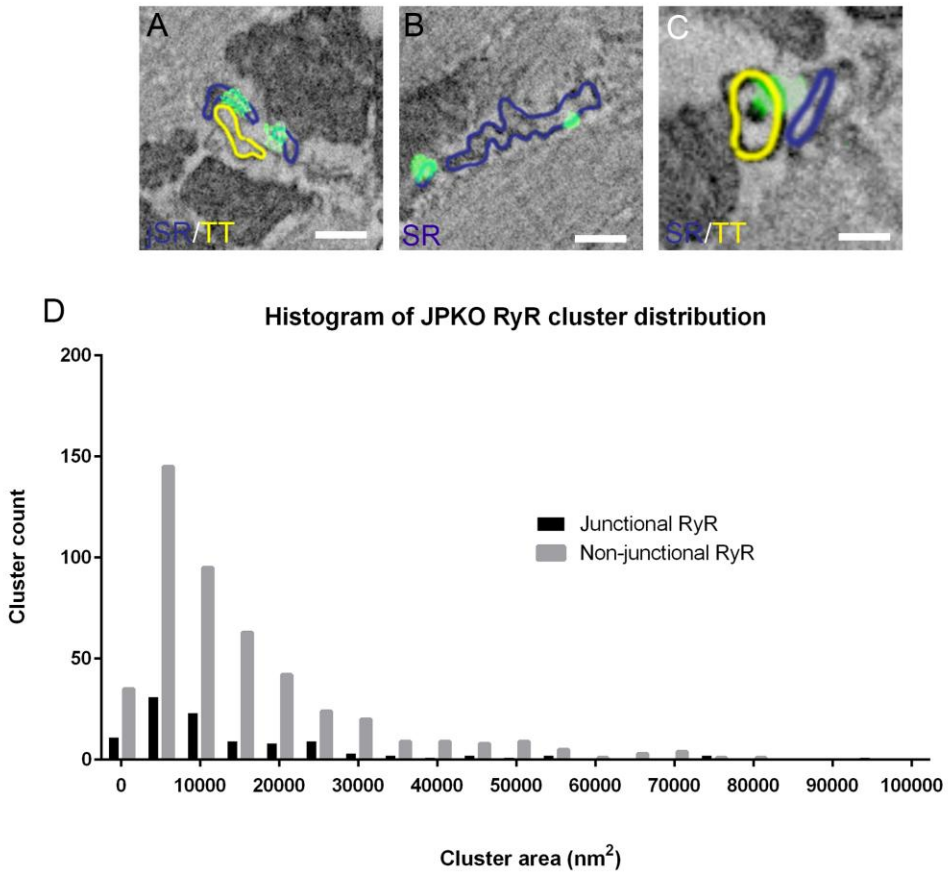

Figure 5.4. : Junctional and non-junctional RyR distribution in correlated STORM –SEM in JPKO tissue. Junctional RyR clusters (green) were identified on the jSR (blue) at the Z-lines adjacent to T-tubules (TT, yellow) in (A). However, some RyR labeling was disassociated from T-tubules (A, C). A significant population non-junctional RyR clusters (green) were identified on the nSR (blue). A histogram of the RyR cluster sizes shows that the distribution is exponential (D) with non-junctional RyRs accounting for 71.7% ± 8.0% (mean ± SD, cells (n) =5, animals (n) =2) of the total RyR clusters in JPKO mouse ventricular tissue. Scale Bars 100nm (A, B, C).

(Fig 5.4A). RyRs localized within junctional clefts wider than 15 nm were classified as un-coupled-non-junctional RyRs or “orphaned RyRs” (Fig. 5.4C). RyR clusters associated with the network SR membrane were classified as nSR-non-junctional RyRs (Fig 5.4B). Lastly, some T-tubule and SR membranes were too disorganized to identify, and, as a result, their associated correlated fluorescence was categorized as unidentified-RyR.

A closer examination of RyRs on the membrane architecture revealed that most RyRs were non-junctional. Some intact dyadic cleft junctions were identified with correlated RyR labeling as in Fig. 5.4A. However, a significant population of junctional membrane complexes was disorganized, and the correlated RyR labeling was orphaned from the T-tubules (Fig. 5.4C). T-tubule structure was deformed, and a higher frequency of nSR and associated correlated RyR labeling was observed (Fig. 5.4B).

We applied the RyR cluster quantification strategy used by Baddeley et al. to the in-resin STORM imaging and found that non-junctional RyRs accounted for 71.7% ± 4.5% (mean ± SD, cells (n) =5, animals (n)=2) of the total recorded RyR localization signals in mouse ventricular tissue [Baddeley et al., 2009]. The frequency histogram of RyR cluster size distributions was found to be exponential, with mean cluster sizes of 15,259 ± 1617 nm^2 (mean ± SEM) and 14,982 ± 654 nm^2 (mean ± SEM) for junctional and non-junctional RyRs, respectively (Fig. 5.4D).

The control demonstrated an exponential distribution of RyR cluster sizes as well. In the control, 21% ± 4.5% (mean ± SD, cells (n) =6, animals (n)=2) of the total RyRs were nSR-non-junctional RyRs with a mean cluster size of 10,286 ± 526 nm^2 (Mean ± SEM). The remaining were junctional RyRs with a mean

cluster size of 14,317 ± 526 nm^2 (Mean ± SEM). The distribution of junctional to non-junctional RyRs is inverted in the JPKO tissue when compared to the control (Fig. 5.5). Analysis of mean cluster sizes of nSR-non-junctional RyRs showed that the JPKO nSR-non-junctional RyR clusters were larger than the wild type ($P < 0.001$ unpaired t – test). There was no significant difference in junctional cluster sizes.

5.5.3. Correlated STORM and EM tomography of RyRs in junctions and non-junctional cytoplasm.

Although SEM imaging allows larger fields of view for imaging and correlation, it lacks any 3D structural information. Thus, we applied EM tomography following STORM imaging to analyze RyR reorganization with respect to sub-cellular membrane remodeling. Fig. 5.6 demonstrates the 3D changes in JPKO ultrastructure following JP2 knock out. Typical T-tubule-jSR coupling in EM tomograms assume smooth, elliptical T-tubule membranes surrounded by closely coupled jSR membranes as seen in the control tissue (Fig. 5.6A). In contrast, JPKO tissue demonstrates enlarged T-tubule diameters with sparse jSR couplings (Fig. 5.6B). In some cases, the T-tubule was observed to drift away from the Z-lines.

Correlated super-resolution imaging of immunolabeled RyRs with low magnification TEM images showed RyRs to be localized at Z-lines (Fig. 5.7). However, further investigation using EM-tomography revealed disrupted membrane organelles associating with RyRs (Fig. 5.7E). The mitochondria (magenta), T-tubule (yellow) and jSR (blue) were manually segmented in the

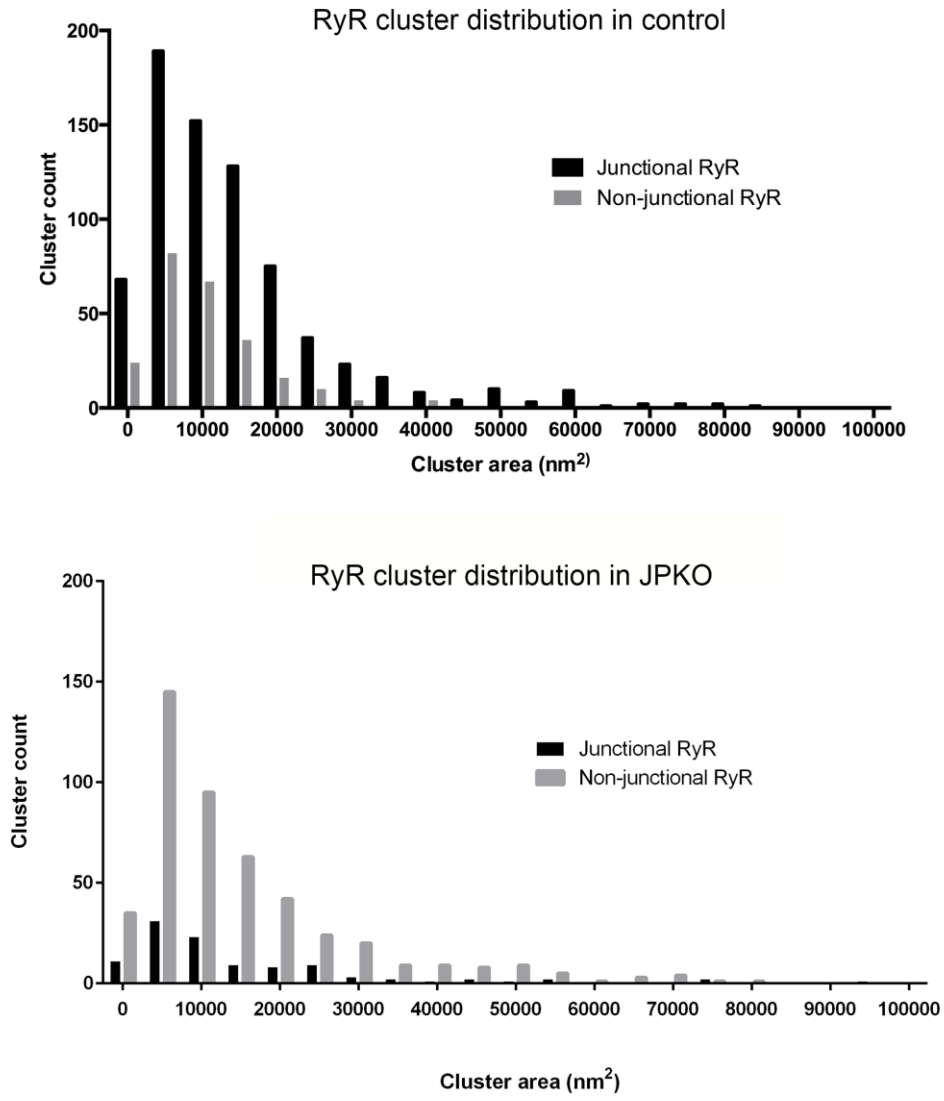

Figure 5.5. : Comparison of junctional and non-junctional RyR cluster distribution in control (A) and JPKO mice (B). There is a significant increase in non-junctional RyR population in JPKO tissue.

Figure 5.6.: Ultrastructure remodeling in JPKO tissue. EM tomography reveals sub-cellular membrane reorganization in JPKO cardiomyocytes. The T-tubule (yellow) and jSR (blue) are manually segmented in tomograms to generate contours. The contours are meshed to generate 3D mesh models of the T-tubule (yellow) and jSR (blue) shown in reference to a 2D slice image reconstructed from tomography. In contrast to the control (A), dilated T-tubules with fragmented jSR are observed in JPKO tissue. Scale bars 500nm (A, B).

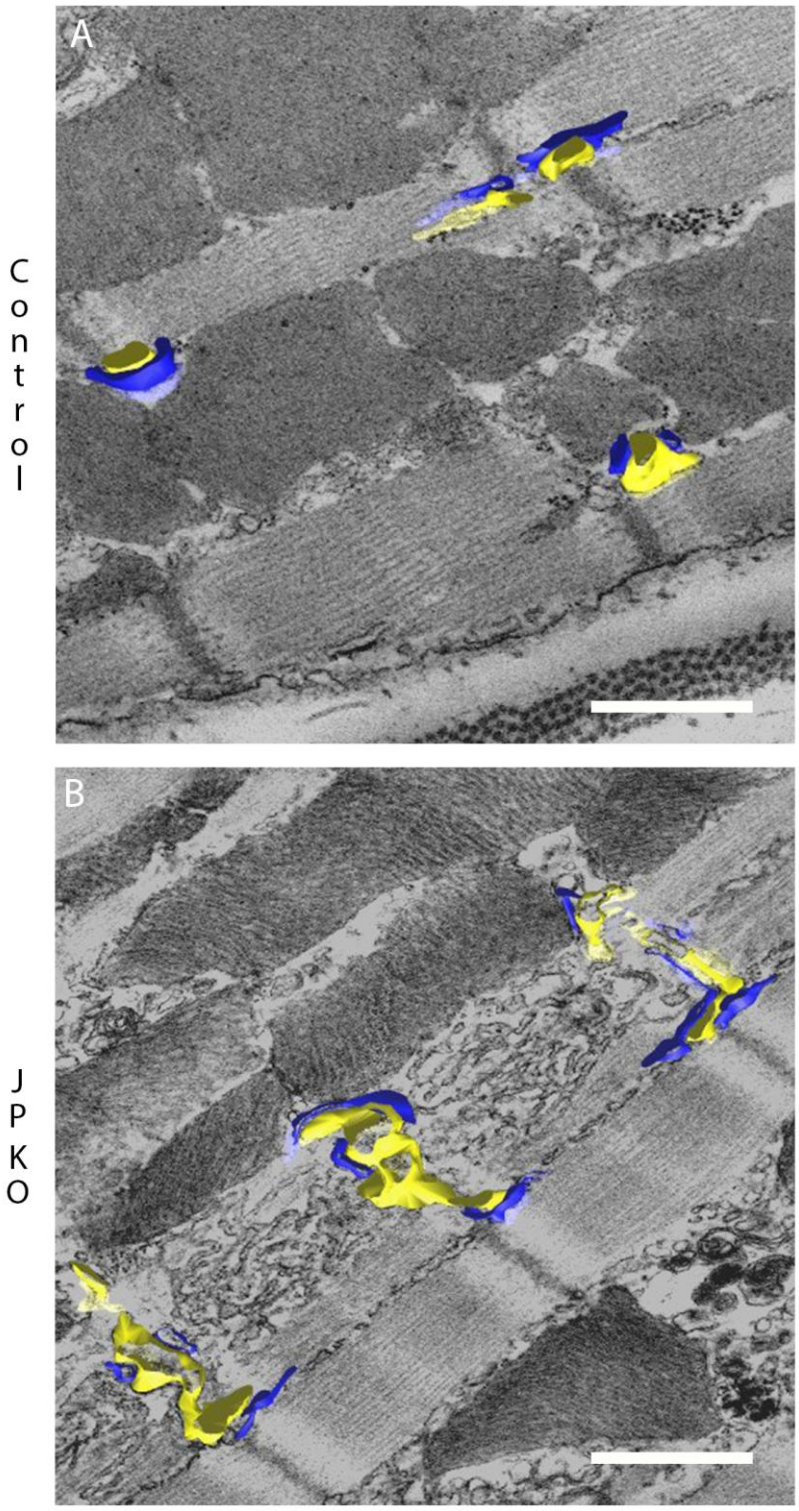
A
Control
B
JPKO

Figure 5.7. : Correlated STORM and electron tomography of immunolabeled RyR in JPKO tissue: The region of interest is identified with diffraction-limited microscopy (A) and then dSTORM imaged (B). The same section is imaged at 0 tilt using a TEM at low magnification (C). 100nm Tetraspeck™ beads are used to correlate the STORM image with the low magnification TEM micrograph (D). A region is identified with RyR fluorescence labeling (boxed region in D) and is imaged for EM tomography. Correlated RyR (green) fluorescence can be identified on the nSR, and jSR in individual sections of the tomogram (E). (F, G, and H) are magnified views of regions in (E). The ultrastructural remodeling of T-tubule and SR have been identified in yellow and blue respectively. RyR labeling is localized extensively on the nSR as well as (F, H) as well as in dyadic clefts (G). Scale bars 2um (A, B, C, D), 1um (E), 100nm (F, G, H).

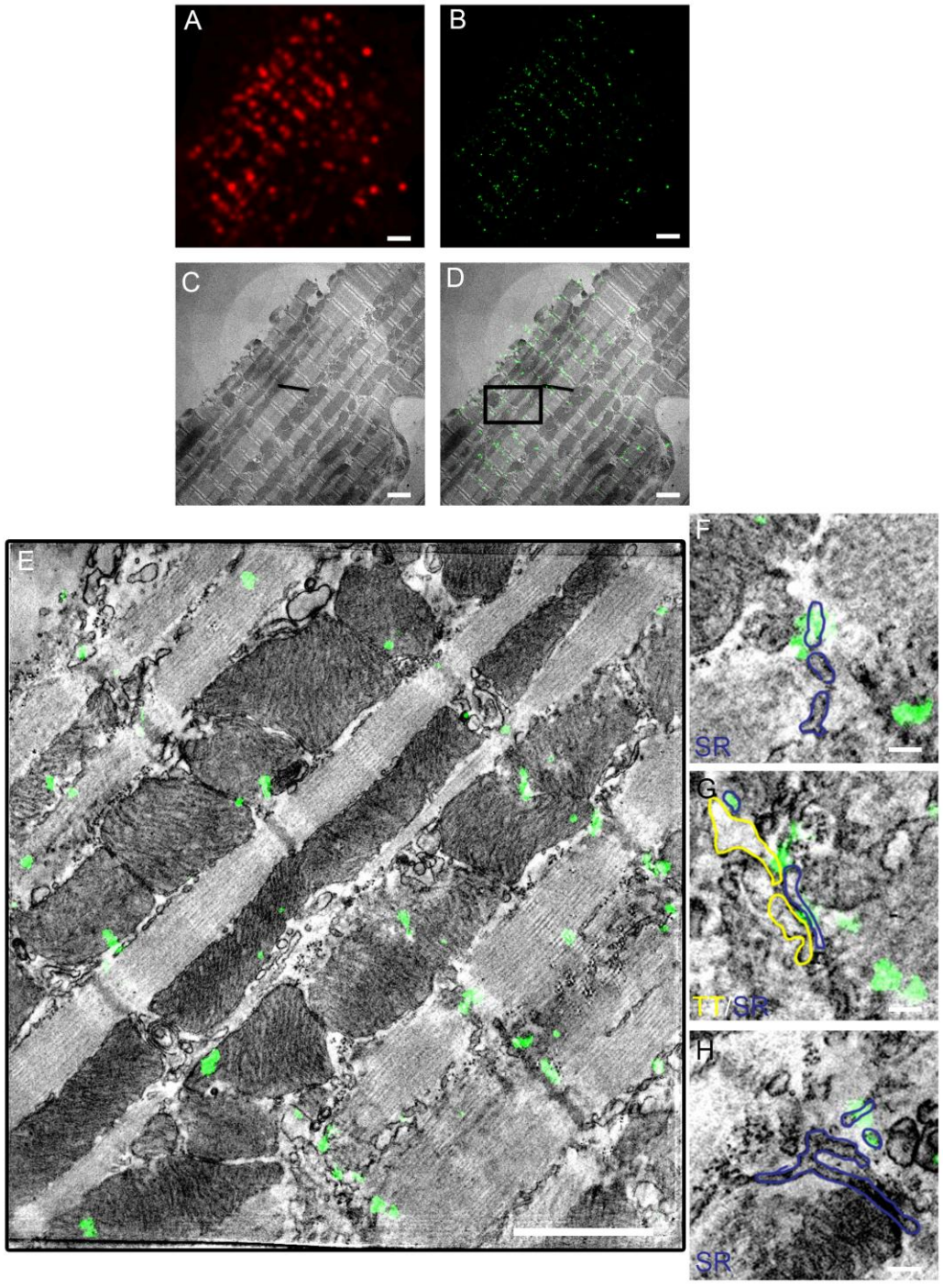
A
B
C
D
E
F
SR
G
TT
SR
H
SR

Figure 5.8. : RyR re-organization and associated structural remodeling in JPKO correlated STORM-EM tomography data. RyR labeling (green) is observed to be localized in dyadic clefts wider than 15nm in (A) as well as in nearby nSR. (blue). (B) demonstrates dilated T-tubules with RyR fluorescence colocalizing at intact junctional membrane complexes. Scale bars 500nm (A,B).

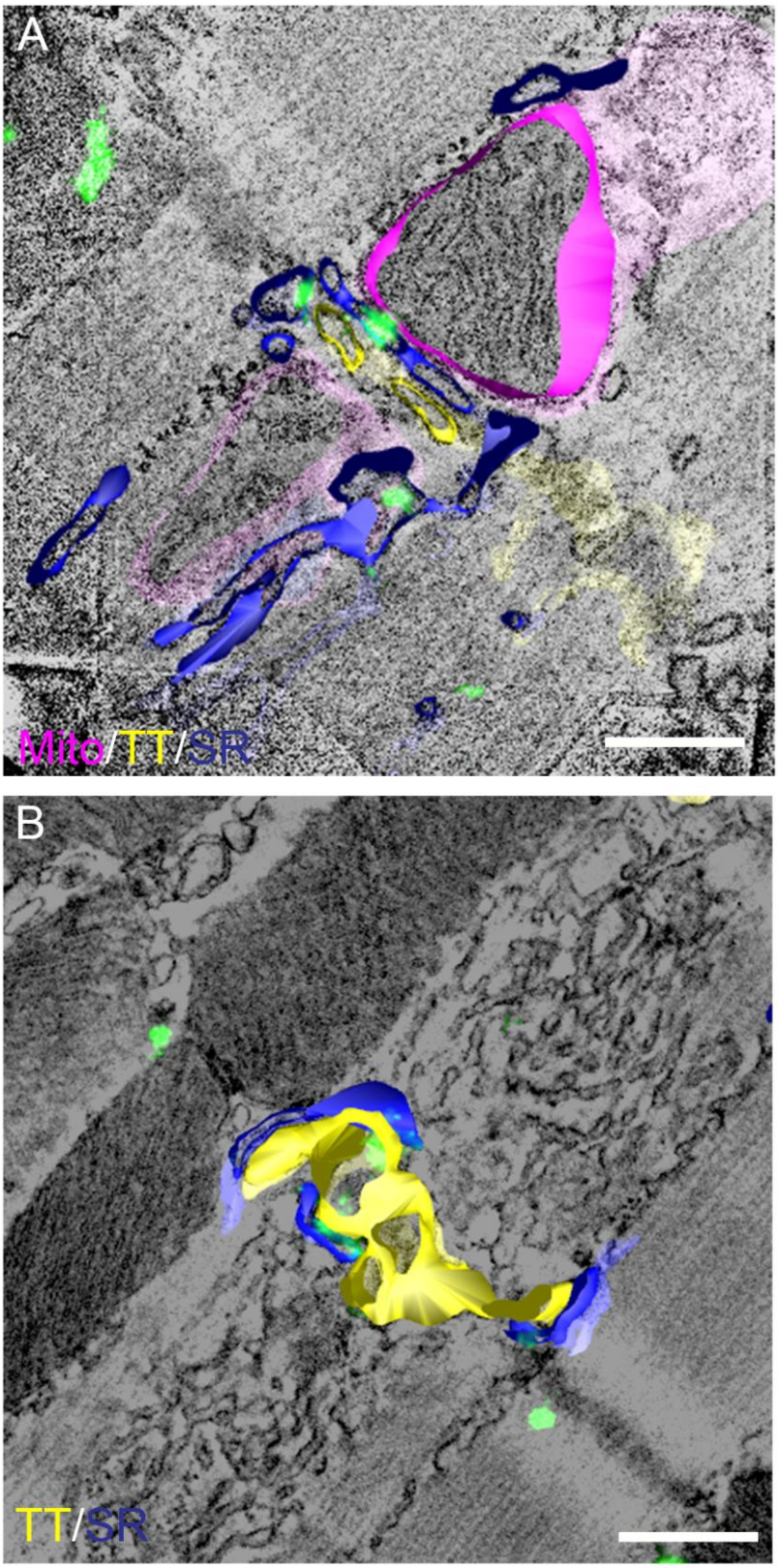
A
Mito/TT/SR
B
TT/SR

tomogram and correlated with green fluorescent STORM data in an individual tomogram slice. As observed in SEM data, a large subset of RyRs was observed to associate with the free SR network. Very few intact dyadic couplings were found.

Surface mesh models of the mitochondria (magenta), T-tubule (yellow) and jSR (blue) were correlated with green fluorescent STORM data and shown in reference to a 2D slice image reconstructed from the tomogram (Fig. 5.8). Dyadic clefts wider than 15nm were identified with correlated RyR fluorescence in Fig. 5.8A. Despite T-tubule dilation, T-tubules were observed to form junctional membrane complexes, which colocalized with STORM RyR data.

5.6. Discussion

Similar to the JP knockdown mouse line established by Van Oort and colleagues, JPKO mice demonstrated a high mortality rate. Therefore, JPKO tamoxifan treatment was limited to 5-7 days like in the Van Oort study. Diffraction limited co-staining of RyRs and T-tubules demonstrated the uncoupling of RyRs from T-tubules in JPKO. T-tubules were more disorganized with damaged elements. However, confocal microscopy has limited resolution and co-staining methods are not enough to discern the extent of RyR disorganization in relation to all membrane architecture. Thus, we applied the super-resolution CLEM technique developed in Chapter 2 to characterize RyR reorganization in response to the knockout of JP2.

We observed that JP knock out resulted in a decrease in junctional RyRs. A similar RyR-LTCC disassociation was reported in JP2 knockdown mice [Van Oort et al., 2011], further cementing the role of JP2 in maintaining junctional cleft

architecture. Disrupted junctional membrane complexes were observed to be near free SR networks with clusters of RyR labeling. To our knowledge, this is the first CLEM study demonstrating the existence of orphaned RyRs at the EM level. Although ~30% of junctional membrane complexes remained intact, most were composed of deformed T-tubules. This is evident in the correlated EM tomography data, in which heavily dilated T-tubules forming junctional complexes with fragments of SR were observed. Accordingly, it has been hypothesized that JP2 plays a role not only in creating junctional membrane complexes, but also in maintaining T-tubule integrity. It is interesting to note that despite the grossly deformed structure, some T-tubules were still able to maintain functional jSR coupling.

A large subset of non-junctional RyRs was observed to localize on the nSR in both SEM and EM tomographic volumes. I realized that the free-floating RyR labeling among myosin filaments in SEM images was not erroneous, but rather was signal arising from nSR networks above and below the section being imaged. The 3D analysis of sections using EM tomography revealed a large population of non-junctional RyRs localized on the free SR. Although more sample analysis is required, it is interesting to note that the increase in JPKO non-junctional-RyRs could possibly be a result of junctional RyRs being redirected away from the uncoupled jSRs. This is in accordance with our findings of non-junctional-RyRs clusters being significantly larger in JPKO cardiomyocytes. Although we don't report an accompanying significant decrease in junctional RyR cluster size, it is possible that the density of RyR clusters is reduced. The remodeling of nSR and sequestering of potential junctional RyRs in the nSR might be another factor contributing to reduced E-C coupling gain due

to the reduced density of intact junctional RyRs. Thus, ion channel re-organization in diseased states is most likely a cumulative result of ultrastructural remodeling and compensatory RyR trafficking in response to cardiac stresses. Studies such as the one conducted in this chapter pose to be an invaluable tool for investigating the functional re-distribution of E-C coupling molecules in response to couplon structure remodeling in diseased states.

5.7. Future perspectives

As microscopy techniques continue to evolve and achieve higher resolution, they radically redefined our view on the structure-function relationship at the E-C coupling site. High-resolution EM tomography studies from my lab were one of the first to report the incomplete filling of dyadic clefts with RyRs [Hayashi et al, 2009]. Super-resolution techniques, which now allow resolutions down to 30nm have further supported these claims, reporting RyR cluster sizes to be smaller than previously thought [Baddeley et al., 2009]. However, as described earlier in chapter 1 each modality has its advantages and scientists greatly benefit from combining the specificity of super-resolution LM with the ultrastructural detailing of EM. As CLEM techniques continue to gain popularity, commercial integrative LM-EM (iCLEM) microscopes are now available for this purpose. However, since both LM-EM imaging is performed in the same chamber, usually one modality suffers for better contrast in the other.

A quick literature search of available CLEM protocols will show that most CLEM protocols have been developed for cultured cell lines. CLEM techniques that are compatible with primary cells and/or thick tissues are very few and far between. Additionally, most CLEM protocols are focused on correlative imaging,

where LM is performed on the full sample and then correlated with individual EM sections. Although correlative LM-EM techniques are useful, they fail to provide the true correlated localization of proteins. Diffraction-limited CLEM strategies have been around since the 1980's, however the added challenge of preserving fluorophore photoswitching for correlated super-resolution and EM has made this challenge even more daunting. Super-resolution imaging was crucial to my project since recent studies have already revealed that diffraction-limited microscopies grossly overestimate cluster sizes [Baddeley et al., 2009]. Combining super-resolution LM with EM structural maps was vital to my project to accurately identify the distribution of RyR subtypes in cardiomycoytes

Thus, the CLEM technique presented in this dissertation aims to provide a versatile super-resolution-LM and EM protocol that can be used with imaging modalities and reagents commonly available in a microscopy lab. The super-resolution technique STORM was chosen for this challenge, as it doesn't require specialized fluorophores for imaging. Targets need to be labeled with Alexa 647, which can be done via traditional immunolabeling techniques. Live cell targeting is also possible with systems such as SNAP-tag. Following fluorescent labeling the sample is processed with commonly used reagents for EM. Thin sections can be imaged via diffraction-limited imaging or STORM followed by SEM, TEM or EM tomography. This allows for CLEM studies in both 2D and 3D using the same protocol. The process of correlation has also been another factor that has hindered the development of CLEM techniques. This is especially a problem in correlative imaging where thin EM sections need to be correlated with whole-block LM imaging. The development of nanometer-sized fluorescent microscopheres that are electron dense has streamlined this process. The CLEM

technique discussed in this thesis further simplified correlation since the same section area is imaged in both LM and EM allowing easier identification of the same ROI in both modalities. In the case of section warping, higher order correlations can be performed. Additionally, since EM is performed separately after LM, the sections can be post-stained for improved contrast during EM imaging. Although there is loss of antibodies during EM processing, using polyclonal antibodies with multiple binding sites can help.

Since most proteins appear are black dense blobs in EM images, it is not possible to discern their identity based on EM staining alone. The distinct shape and location of these blobs on organellar membranes gives us a clue to the identity for some proteins. In the case of RyRs, only junctional RyRs observed as opaque dense bridges across the dyadic cleft can be identified to an extent. Similarly, corbular SR can also be identified to a degree because of the high density of RyR clusters. However, individual and smaller non-junctional RyRs are difficult to localize among the darkly stained sub-cellular membranes. Similarly, ion-channels such as the LTCCs and NCX are indistinguishable from other transmembrane protiens A traditional approach towards identifying proteins within EM micrographs involves using post-embedding antibody-based colloidal gold labeling. Unfortunately, these methods are limited by antigen availability in resin sections. In this regard, the CLEM method introduced here acts as an invaluable tool to discern protein distribution at EM scale resolutions.

These techniques can also provide scientists with the much-needed geometrical data needed to generate mathematical models to explore the relationship between sub-cellular Ca dynamics and the spatial clustering of RyRs. Such modeling is necessary since studies have revealed substantial

ultrastructural alterations in the SR and T-tubule of cardiomyocytes during times of cardiac disease, as well as in the distribution of ion channels and pumps. Most simulation models rely on simplified representations of organelle geometry and completely disregard protein distribution. The impact of realistic geometries included in reaction-diffusion calculations was demonstrated in a recent study by Hake et al. [Hake et al., 2013]. Realistic geometries with associated E-C coupling molecule organization will help refine such modeling research environments and allow for more physiologically accurate simulations.

Additionally, molecular organizations of receptors on the membrane as well as dynamic membrane folding processes, all of which contribute to functional E-C coupling, still remain undetermined. It has been proposed that RyR clustering on membranes may not be static due to channel diffusion and membrane remodeling. Individual tetramers tend to diffuse along the lipid membrane and reorient themselves within the membrane. Receptor reorganization affects direct allosteric effects and CICR between RyRs within a cluster as well as the interaction between CRU sub-clusters, which are coupled via diffusion in the junctional space [Soeller et al., 1997, Peng et al., 2005; Sobie et al., 2006]. Furthermore, membrane modifications could alter CICR as well as the functional coupling between the LTCCs located on the sarcolemma and the closely opposing RyR clusters on SR, which is crucial for efficient and synchronous E-C coupling [Koh et al.,2006; Tanskanen et al., 2007]. Thus, there is a need to be able to resolve nano-scopic biological structures along with the dynamic nature of the assembly of macromolecular signaling complexes. This further requires combining sub-diffraction limit live imaging of molecular movements with 3D EM technologies.

Lastly, the CLEM method developed in this dissertation was also used as screening technique for EM. We applied this technique to identify induced pluripotent cells grafted onto mouse hearts for differentiation. These cells expressed genetic markers in the nucleus, which were targeted with Alexa 647. Since we were using the fluorescence just to identify cells (not for super-resolution) we opted for higher Os concentrations for higher EM contrast. Embedded sections were then sectioned and imaged . Using the nuclear fluorescence as an anatomical marker, the iPS cells could successfully be identified from the native mouse heart cardiomyocytes and the extent of differentiation was studied at the EM level.

In summary, the work presented in this dissertation provides a novel correlated super-resolution and EM technique to identify the distribution E-C coupling molecules in relation to sub-cellular E-C coupling membrane compartmentation. Correlated 2D STORM-SEM and 3D STORM-EM tomography techniques were developed to study the localization of protiens across the cell and on high-resolution reconstructions of the 3D ultrastructure of cells, respectively. . The validity of the technique was tested and established by successfully correlating super-resolution RyR labeling with electron-dense feet structures in EM tomography. Lesser-characterized non-junctional RyRs could be now be identified and were studied with this novel technique. Additionally, the cellular maps provided by EM allowed the investigation of E-C coupling ion channel reorganization in response to structural remodeling during cardiac heart failure. The number and mean cluster size of non-junctional RyRs was observed to increase in genetic ablation JP mouse models. While microscopic technologies continue to advance rapidly in both EM and LM, the CLEM techniques developed

here complementarily enhance nanoscale information on subcellular structures equipping scientists with better tools to investigate the basis of cardiac E-C coupling. Ongoing developments such as those introduced in this dissertation are simplifying the CLEM process and will ultimately help establish CLEM as a routine technique in the laboratory.

This chapter, in part, is a reprint of the material as it appears in Journal of Molecular and Cellular Cardiology, 2013. Das T, Hoshijima M. The dissertation author was the primary investigator and author of this paper. This chapter, in part, is currently being prepared for submission for publication of the material. Das T, Hoshijima M. The dissertation/thesis author was the primary investigator and author of this material.

References

Abbe, E. 1873. Beiträge zur Theorie des Mikroskops und der mikroskopischen Wahrnehmung. Archiv für mikroskopische Anatomie. 9:413–418.

Adams SR, Campbell RE, Gross LA, Martin BR, Walkup GK, Yao Y, Llopis J, Tsien RY. New biarsenical ligands and tetracysteine motifs for protein labeling in vitro and in vivo: synthesis and biological applications. J Am Chem Soc. 2002 May 29;124(21):6063-76. PubMed PMID: 12022841.

Agard, David A., and John W. Sedat. "Three-dimensional architecture of a polytene nucleus." *Nature* 302.5910 (1983): 676-681.

Ahern GP, Junankar PR, Dulhunty AF. Single channel activity of the ryanodine receptor calcium release channel is modulated by FK-506. FEBS Lett. 1994 Oct 3;352(3):369-74. PubMed PMID: 7523191.

Andersson KB, Winer LH, Mørk HK, Molkentin JD, Jaisser F. Tamoxifen administration routes and dosage for inducible Cre-mediated gene disruption in mouse hearts. Transgenic Res. 2010 Aug;19(4):715-25. doi: 10.1007/s11248-009-9342-4. Epub 2009 Nov 6. PubMed PMID: 19894134.

Asghari P, Schulson M, Scriven DR, Martens G, Moore ED. Axial tubules of rat ventricular myocytes form multiple junctions with the sarcoplasmic reticulum. Biophys J. 2009;96:4651-60.

Asghari P, Scriven DR, Hoskins J, Fameli N, van Breemen C, Moore ED. The structure and functioning of the couplon in the mammalian cardiomyocyte. Protoplasma. 2012 Feb;249 Suppl 1:S31-8. doi: 10.1007/s00709-011-0347-5. Epub 2011 Nov 5. Review. PubMed PMID: 22057630.

Asghari P, Scriven DR, Sanatani S, Gandhi SK, Campbell AI, Moore ED. Nonuniform and variable arrangements of ryanodine receptors within mammalian ventricular couplons. Circ Res. 2014 Jul 7;115(2):252-62. doi: 10.1161/CIRCRESAHA.115.303897. Epub 2014 Apr 30. PubMed PMID: 24786399.

Baddeley D, Jayasinghe ID, Lam L, Rossberger S, Cannell MB, Soeller C. Optical single-channel resolution imaging of the ryanodine receptor distribution in rat cardiac myocytes. Proc Natl Acad Sci U S A. 2009;106:22275-80.

Baker PF, Blaustein MP, Hodgkin AL, Steinhardt RA. The influence of calcium on sodium efflux in squid axons. *The Journal of Physiology*. 1969;200(2):431-458.

Balijepalli RC, Foell JD, Hall DD, Hell JW, Kamp TJ. Localization of cardiac L-type Ca(2+) channels to a caveolar macromolecular signaling complex is required for beta(2)-adrenergic regulation. Proc Natl Acad Sci U S A. 2006 May 9;103(19):7500-5. Epub 2006 Apr 28. PubMed PMID: 16648270; PubMed Central PMCID: PMC1564282.

Bárcena M, Koster AJ. Electron tomography in life science. Semin Cell Dev Biol. 2009 Oct;20(8):920-30. doi: 10.1016/j.semcdb.2009.07.008. Epub 2009 Aug 5. Review. PubMed PMID: 19664718.

Barg S, Copello JA, Fleischer S. Different interactions of cardiac and skeletal muscle ryanodine receptors with FK-506 binding protein isoforms. Am J Physiol. 1997 May;272(5 Pt 1):C1726-33. PubMed PMID: 9176165.

Barouch LA, Harrison RW, Skaf MW, Rosas GO, Cappola TP, Kobeissi ZA, Hobai IA, Lemmon CA, Burnett AL, O'Rourke B, Rodriguez ER, Huang PL, Lima JA, Berkowitz DE, Hare JM. Nitric oxide regulates the heart by spatial confinement of nitric oxide synthase isoforms. Nature. 2002 Mar 21;416(6878):337-9. PubMed PMID: 11907582.

Bates M, Huang B, Dempsey GT, Zhuang X. Multicolor super-resolution imaging with photo-switchable fluorescent probes. Science. 2007 Sep 21;317(5845):1749-53. Epub 2007 Aug 16. PubMed PMID: 17702910; PubMed Central PMCID: PMC2633025.

Battig CG, Low FN. The ultrastructure of human cardiac muscle and its associated tissue space. American Journal of Anatomy. 1961;108:199-229.

Beavers DL, Wang W, Ather S, Voigt N, Garbino A, Dixit SS, Landstrom AP, Li N, Wang Q, Olivotto I, Dobrev D, Ackerman MJ, Wehrens XH. Mutation E169K in junctophilin-2 causes atrial fibrillation due to impaired RyR2 stabilization. J Am Coll Cardiol. 2013 Nov 19;62(21):2010-9. doi: 10.1016/j.jacc.2013.06.052. Epub 2013 Aug 21. PubMed PMID: 23973696; PubMed Central PMCID: PMC3830688.

Beck M, Förster F, Ecke M, Plitzko JM, Melchior F, Gerisch G, Baumeister W, Medalia O. Nuclear pore complex structure and dynamics revealed by cryoelectron tomography. Science. 2004 Nov 19;306(5700):1387-90. Epub 2004 Oct 28. PubMed PMID: 15514115.

Benacquista BL, Sharma MR, Samsó M, Zorzato F, Treves S, Wagenknecht T. Amino acid residues 4425-4621 localized on the three-dimensional structure of the skeletal muscle ryanodine receptor. Biophys J. 2000 Mar;78(3):1349-58. PubMed PMID: 10692321; PubMed Central PMCID: PMC1300734.

Bennett HS, Porter KR. An electron microscope study of sectioned breast muscle of the domestic fowl. The American journal of anatomy. 1953;93:61-105.

Bers DM. Calcium cycling and signaling in cardiac myocytes. Annu Rev Physiol. 2008;70:23-49.

Bers DM. Cardiac excitation-contraction coupling. Nature. 2002 Jan 10;415(6868):198-205. Review. PubMed PMID: 11805843.

Bertocchini F, Ovitt CE, Conti A, Barone V, Schöler HR, Bottinelli R, Reggiani C, Sorrentino V. Requirement for the ryanodine receptor type 3 for efficient

contraction in neonatal skeletal muscles. EMBO J. 1997 Dec 1;16(23):6956-63. PubMed PMID: 9384575; PubMed Central PMCID: PMC1170299.

Best JM, Kamp TJ. Different subcellular populations of L-type Ca2+ channels exhibit unique regulation and functional roles in cardiomyocytes. J Mol Cell Cardiol. 2012 Feb;52(2):376-87. doi: 10.1016/j.yjmcc.2011.08.014. Epub 2011 Aug 23. Review. PubMed PMID: 21888911; PubMed Central PMCID: PMC3264751.

Betzig E, Lewis A, Harootunian A, Isaacson M, Kratschmer E. Near Field Scanning Optical Microscopy (NSOM): Development and Biophysical Applications. Biophys J. 1986 Jan;49(1):269-79. PubMed PMID: 19431633; PubMed Central PMCID: PMC1329633.

Betzig E, Patterson GH, Sougrat R, Lindwasser OW, Olenych S, Bonifacino JS, Davidson MW, Lippincott-Schwartz J, Hess HF. Imaging intracellular fluorescent proteins at nanometer resolution. Science. 2006 Sep 15;313(5793):1642-5. Epub 2006 Aug 10. PubMed PMID: 16902090.

Beuckelmann DJ, Näbauer M, Erdmann E. Intracellular calcium handling in isolated ventricular myocytes from patients with terminal heart failure. Circulation. 1992 Mar;85(3):1046-55. PubMed PMID: 1311223.

Beutner G, Sharma VK, Giovannucci DR, Yule DI, Sheu SS. Identification of a ryanodine receptor in rat heart mitochondria. J Biol Chem. 2001 Jun 15;276(24):21482-8. Epub 2001 Apr 10. PubMed PMID: 11297554.

Beutner G, Sharma VK, Lin L, Ryu SY, Dirksen RT, Sheu SS. Type 1 ryanodine receptor in cardiac mitochondria: transducer of excitation-metabolism coupling. Biochim Biophys Acta. 2005 Nov 10;1717(1):1-10. Epub 2005 Oct 11. PubMed PMID: 16246297.

Brette F, Orchard C. T-tubule function in mammalian cardiac myocytes. Circ Res. 2003;92:1182-92.

Briggman KL, Bock DD. Volume electron microscopy for neuronal circuit reconstruction. Curr Opin Neurobiol. 2012 Feb;22(1):154-61. doi: 10.1016/j.conb.2011.10.022. Epub 2011 Nov 24. Review. PubMed PMID: 22119321.

Brillantes AB, Ondrias K, Scott A, Kobrinsky E, Ondriasová E, Moschella MC, Jayaraman T, Landers M, Ehrlich BE, Marks AR. Stabilization of calcium release channel (ryanodine receptor) function by FK506-binding protein. Cell. 1994 May 20;77(4):513-23. PubMed PMID: 7514503.

Brochet DX, Xie W, Yang D, Cheng H, Lederer WJ. Quarky calcium release in the heart. Circ Res. 2011 Jan 21;108(2):210-8. doi: 10.1161/CIRCRESAHA.110.231258. Epub 2010 Dec 9. PubMed PMID: 21148431; PubMed Central PMCID: PMC3036985.

Brochet DX, Yang D, Cheng H, Lederer WJ. Elementary calcium release events from the sarcoplasmic reticulum in the heart. Adv Exp Med Biol. 2012;740:499-509.

Brochet DX, Yang D, Di Maio A, Lederer WJ, Franzini-Armstrong C, Cheng H. Ca2+ blinks: rapid nanoscopic store calcium signaling. Proceedings of the National Academy of Sciences of the United States of America. 2005;102:3099-104.

Bron C, Gremillet P, Launay D, Jourlin M, Gautschi HP, Bächi T, Schüpbach J. Three-dimensional electron microscopy of entire cells. J Microsc. 1990 Jan;157(Pt 1):115-26. PubMed PMID: 2299660.

Bushby AJ, P'ng KM, Young RD, Pinali C, Knupp C, Quantock AJ. Imaging three-dimensional tissue architectures by focused ion beam scanning electron microscopy. Nat Protoc. 2011 Jun;6(6):845-58. doi: 10.1038/nprot.2011.332. Epub 2011 May 26. PubMed PMID: 21637203.

Cannell MB, Kong CH, Imtiaz MS, Laver DR. Control of sarcoplasmic reticulum Ca2+ release by stochastic RyR gating within a 3D model of the cardiac dyad and importance of induction decay for CICR termination. Biophys J. 2013 May 21;104(10):2149-59. doi: 10.1016/j.bpj.2013.03.058. PubMed PMID: 23708355; PubMed Central PMCID: PMC3660628.

Cannell MB, Kong CH. Local control in cardiac E-C coupling. Journal of molecular and cellular cardiology. 2012;52:298-303.

Carozzi AJ, Ikonen E, Lindsay MR, Parton RG. Role of cholesterol in developing T-tubules: analogous mechanisms for T-tubule and caveolae biogenesis. Traffic. 2000 Apr;1(4):326-41. PubMed PMID: 11208118.

Chen B, Li Y, Jiang S, Xie YP, Guo A, Kutschke W, Zimmerman K, Weiss RM, Miller FJ, Anderson ME, Song LS. β-Adrenergic receptor antagonists ameliorate myocyte T-tubule remodeling following myocardial infarction. FASEB J. 2012 Jun;26(6):2531-7. doi: 10.1096/fj.11-199505. Epub 2012 Feb 28. PubMed PMID: 22375019; PubMed Central PMCID: PMC3360148.

Chen-Izu Y, McCulle SL, Ward CW, Soeller C, Allen BM, Rabang C, et al. Three-dimensional distribution of ryanodine receptor clusters in cardiac myocytes. Biophysical journal. 2006;91:1-13.

Cheng H, Lederer WJ, Cannell MB. Calcium sparks: elementary events underlying excitation-contraction coupling in heart muscle. Science. 1993;262:740-4.

Cheng H, Lederer WJ. Calcium sparks. Physiol Rev. 2008;88:1491-545.

Ching LL, Williams AJ, Sitsapesan R. Evidence for Ca(2+) activation and inactivation sites on the luminal side of the cardiac ryanodine receptor complex. Circ Res. 2000 Aug 4;87(3):201-6. PubMed PMID: 10926870.

Chu A, Díaz-Muñoz M, Hawkes MJ, Brush K, Hamilton SL. Ryanodine as a probe for the functional state of the skeletal muscle sarcoplasmic reticulum calcium release channel. Mol Pharmacol. 1990 May;37(5):735-41. PubMed PMID: 1692609.

Costantin LL, Franzini-Armstrong C, Podolsky RJ. Localization of Calcium-Accumulating Structures in Striated Muscle Fibers. Science. 1965;147:158-60.

Cremer C, Cremer T. Considerations on a laser-scanning-microscope with high resolution and depth of field. Microsc Acta. 1978 Sep;81(1):31-44. PubMed PMID: 713859.

Crossman DJ, Ruygrok PR, Soeller C, Cannell MB. Changes in the organization of excitation-contraction coupling structures in failing human heart. PLoS One. 2011;6:e17901.

Csordás G, Renken C, Várnai P, Walter L, Weaver D, Buttle KF, Balla T, Mannella CA, Hajnóczky G. Structural and functional features and significance of the physical linkage between ER and mitochondria. J Cell Biol. 2006 Sep 25;174(7):915-21. Epub 2006 Sep 18. PubMed PMID: 16982799; PubMed Central PMCID: PMC2064383.

Dan P, Lin E, Huang J, Biln P, Tibbits GF. Three-dimensional distribution of cardiac Na+-Ca2+ exchanger and ryanodine receptor during development. Biophys J. 2007 Oct 1;93(7):2504-18. Epub 2007 Jun 8. PubMed PMID: 17557789; PubMed Central PMCID: PMC1965441.

Das T, Hoshijima M. Adding a new dimension to cardiac nano-architecture using electron microscopy: coupling membrane excitation to calcium signaling. J Mol Cell Cardiol. 2013 May;58:5-12. doi: 10.1016/j.yjmcc.2012.11.009. Epub 2012 Nov 29. Review. PubMed PMID: 23201225.

Deerinck TJ, Martone ME, Lev-Ram V, Green DP, Tsien RY, Spector DL, Huang S, Ellisman MH. Fluorescence photooxidation with eosin: a method for high resolution immunolocalization and in situ hybridization detection for light and electron microscopy. J Cell Biol. 1994 Aug;126(4):901-10. PubMed PMID: 7519623; PubMed Central PMCID: PMC2120127.

Deivanayagam CC, Carson M, Thotakura A, Narayana SV, Chodavarapu RS. Structure of FKBP12.6 in complex with rapamycin. Acta Crystallogr D Biol Crystallogr. 2000 Mar;56(Pt 3):266-71. PubMed PMID: 10713512.

Dempsey GT, Vaughan JC, Chen KH, Bates M, Zhuang X. Evaluation of fluorophores for optimal performance in localization-based super-resolution

imaging. Nat Methods. 2011 Nov 6;8(12):1027-36. doi: 10.1038/nmeth.1768. PubMed PMID: 22056676; PubMed Central PMCID: PMC3272503.

Denk W, Horstmann H. Serial block-face scanning electron microscopy to reconstruct three-dimensional tissue nanostructure. PLoS Biol. 2004 Nov;2(11):e329. Epub 2004 Oct 19. PubMed PMID: 15514700; PubMed Central PMCID: PMC524270.

Di Maio A, Karko K, Snopko RM, Mejia-Alvarez R, Franzini-Armstrong C. T-tubule formation in cardiacmyocytes: two possible mechanisms? Journal of muscle research and cell motility. 2007;28:231-41.

Donnert G, Keller J, Wurm CA, Rizzoli SO, Westphal V, Schönle A, Jahn R, Jakobs S, Eggeling C, Hell SW. Two-color far-field fluorescence nanoscopy. Biophys J. 2007 Apr 15;92(8):L67-9. Epub 2007 Feb 16. PubMed PMID: 17307826; PubMed Central PMCID: PMC1831704.

Dulhunty AF. Excitation-contraction coupling from the 1950s into the new millennium. Clin Exp Pharmacol Physiol. 2006;33:763-72.

E.H. Synge (1928). "A suggested method for extending the microscopic resolution into the ultramicroscopic region". Phil. Mag. 6: 356

Ebashi S, Lipmann F. Adenosine Triphosphate-Linked Concentration of Calcium Ions in a Particulate Fraction of Rabbit Muscle. The Journal of cell biology. 1962;14:389-400.

Ellisman MH, Deerinck TJ, Shu X, Sosinsky GE. Picking faces out of a crowd: genetic labels for identification of proteins in correlated light and electron microscopy imaging. Methods in cell biology. 2012;111:139-55.

Endo M, Tanaka M, Ogawa Y. Calcium induced release of calcium from the sarcoplasmic reticulum of skinned skeletal muscle fibres. Nature. 1970;228:34-6.

Fabiato A, Fabiato F. Excitation-contraction coupling of isolated cardiac fibers with disrupted or closed sarcolemmas. Calcium-dependent cyclic and tonic contractions. Circulation research. 1972;31:293-307.

Fawcett DW, McNutt NS. The ultrastructure of the cat myocardium. I. Ventricular papillary muscle. The Journal of cell biology. 1969;42:1-45.

Fernandez JJ. Computational methods for electron tomography. Micron. 2012 Oct;43(10):1010-30. doi: 10.1016/j.micron.2012.05.003. Epub 2012 May 18. Review. PubMed PMID: 22658288.

Fill M, Copello JA. Ryanodine receptor calcium release channels. Physiol Rev. 2002 Oct;82(4):893-922. Review. PubMed PMID: 12270947.

Fleischer S, Ogunbunmi EM, Dixon MC, Fleer EA. Localization of Ca2+ release channels with ryanodine in junctional terminal cisternae of sarcoplasmic reticulum of fast skeletal muscle. Proceedings of the National Academy of Sciences of the United States of America. 1985;82:7256-9.

Forbes MS, Hawkey LA, Sperelakis N. The transverse-axial tubular system (TATS) of mouse myocardium: its morphology in the developing and adult animal. Am J Anat. 1984;170:143-62.

Forbes MS, Sperelakis N. Bridging junctional processes in coupling fo skeletal, cardiac, and smooth muscle. Muscle Nerve. 1982;5:674-81.

Forbes MS, Sperelakis N. Ultrastructure of mammalian cardiac muscle. In: Sperelakis N, editor. Physiology and pathophysiology of the heart. Dordrecht, the Netherlands: Kluwer Academic Publishers; 1984. p. 3-42.

Ford LE, Podolsky RJ. Regenerative calcium release within muscle cells. Science. 1970;167:58-9.

Frank GB. The current view of the source of trigger calcium in excitation-contraction coupling in vertebrate skeletal muscle. Biochem Pharmacol. 1980;29:2399-406.

Frank JS, Beydler S, Mottino G. Membrane structure in ultrarapidly frozen, unpretreated, freeze-fractured myocardium. Circulation research. 1987;61:141-7.

Frank JS, Mottino G, Reid D, Molday RS, Philipson KD. Distribution of the Na(+)-Ca2+ exchange protein in mammalian cardiac myocytes: an immunofluorescence and immunocolloidal gold-labeling study. J Cell Biol. 1992 Apr;117(2):337-45. PubMed PMID: 1373142; PubMed Central PMCID: PMC2289429.

Frank, Joachim. "Three-dimensional reconstruction of single molecules."Methods in cell biology 22 (1981): 325-344.

Franzini-Armstrong C, Porter KR. Sarcolemmal Invaginations Constituting the T System in Fish Muscle Fibers. The Journal of cell biology. 1964;22:675-96.

Franzini-Armstrong C, Protasi F, Ramesh V. Comparative ultrastructure of Ca2+ release units in skeletal and cardiac muscle. Annals of the New York Academy of Sciences. 1998;853:20-30.

Franzini-Armstrong C, Protasi F, Ramesh V. Shape, size, and distribution of Ca(2+) release units and couplons in skeletal and cardiac muscles. Biophysical Journal. 1999;77:1528-39.

Franzini-Armstrong C. ER-mitochondria communication. How privileged? Physiology (Bethesda). 2007 Aug;22:261-8. Review. PubMed PMID: 17699879.

Franzini-Armstrong C. Fine Structure of Sarcoplasmic Reticulum and Tranverse Tubular System in Muscle Fibers. Fed Proc. 1964;23:887-95.

Franzini-Armstrong C. Structure of sarcoplasmic reticulum. Fed Proc. 1980;39:2403-9.

Frey TG, Perkins GA, Ellisman MH. Electron tomography of membrane-bound cellular organelles. Annu Rev Biophys Biomol Struct. 2006;35:199-224. Review. PubMed PMID: 16689634.

Galeotti N, Quattrone A, Vivoli E, Norcini M, Bartolini A, Ghelardini C. Different involvement of type 1, 2, and 3 ryanodine receptors in memory processes. Learn Mem. 2008 Apr 25;15(5):315-23. doi: 10.1101/lm.929008. Print 2008 May. PubMed PMID: 18441289; PubMed Central PMCID: PMC2364603.

Gathercole DV, Colling DJ, Skepper JN, Takagishi Y, Levi AJ, Severs NJ. Immunogold-labeled L-type calcium channels are clustered in the surface plasma membrane overlying junctional sarcoplasmic reticulum in guinea-pig myocytes-implications for excitation-contraction coupling in cardiac muscle. J Mol Cell Cardiol. 2000 Nov;32(11):1981-94. PubMed PMID: 11040103.

Gautier A, Juillerat A, Heinis C, Corrêa IR Jr, Kindermann M, Beaufils F, Johnsson K. An engineered protein tag for multiprotein labeling in living cells. Chem Biol. 2008 Feb;15(2):128-36. doi: 10.1016/j.chembiol.2008.01.007. PubMed PMID: 18291317.

Giepmans BN, Adams SR, Ellisman MH, Tsien RY. The fluorescent toolbox for assessing protein location and function. Science. 2006 Apr 14;312(5771):217-24. Review. PubMed PMID: 16614209.

Glenney JR Jr, Soppet D. Sequence and expression of caveolin, a protein component of caveolae plasma membrane domains phosphorylated on tyrosine in Rous sarcoma virus-transformed fibroblasts. Proc Natl Acad Sci U S A. 1992 Nov 1;89(21):10517-21. PubMed PMID: 1279683; PubMed Central PMCID: PMC50370.

Glenney, John R. "The sequence of human caveolin reveals identity with VIP21, a component of transport vesicles." FEBS letters 314.1 (1992): 45-48.

Go AS, Mozaffarian D, Roger VL, Benjamin EJ, Berry JD, Blaha MJ, Dai S, Ford ES, Fox CS, Franco S, Fullerton HJ, Gillespie C, Hailpern SM, Heit JA, Howard VJ, Huffman MD, Judd SE, Kissela BM, Kittner SJ, Lackland DT, Lichtman JH, Lisabeth LD, Mackey RH, Magid DJ, Marcus GM, Marelli A, Matchar DB, McGuire DK, Mohler ER 3rd, Moy CS, Mussolino ME, Neumar RW, Nichol G, Pandey DK, Paynter NP, Reeves MJ, Sorlie PD, Stein J, Towfighi A, Turan TN, Virani SS, Wong ND, Woo D, Turner MB; American Heart Association Statistics Committee and Stroke Statistics Subcommittee. Executive summary: heart disease and stroke statistics--2014 update: a report from the American Heart

Association. Circulation. 2014 Jan 21;129(3):399-410.doi: 10.1161/01.cir.0000442015.53336.12. PubMed PMID: 24446411.

Golini L, Chouabe C, Berthier C, Cusimano V, Fornaro M, Bonvallet R, Formoso L, Giacomello E, Jacquemond V, Sorrentino V. Junctophilin 1 and 2 proteins interact with the L-type Ca2+ channel dihydropyridine receptors (DHPRs) in skeletal muscle. J Biol Chem. 2011 Dec 23;286(51):43717-25. doi: 10.1074/jbc.M111.292755. Epub 2011 Oct 21. PubMed PMID: 22020936; PubMed Central PMCID: PMC3243543.

Gómez AM, Valdivia HH, Cheng H, Lederer MR, Santana LF, Cannell MB, McCune SA, Altschuld RA, Lederer WJ. Defective excitation-contraction coupling in experimental cardiac hypertrophy and heart failure. Science. 1997 May 2;276(5313):800-6. PubMed PMID: 9115206.

Guo T, Cornea RL, Huke S, Camors E, Yang Y, Picht E, Fruen BR, Bers DM. Kinetics of FKBP12.6 binding to ryanodine receptors in permeabilized cardiac myocytes and effects on Ca sparks. Circ Res. 2010 Jun 11;106(11):1743-52. doi: 10.1161/CIRCRESAHA.110.219816. Epub 2010 Apr 29. PubMed PMID: 20431056; PubMed Central PMCID: PMC2895429.

Gustafsson MG, Agard DA, Sedat JW. I5M: 3D widefield light microscopy with better than 100 nm axial resolution. J Microsc. 1999 Jul;195(Pt 1):10-6. PubMed PMID: 10444297.

Gustafsson MG. Surpassing the lateral resolution limit by a factor of two using structured illumination microscopy. J Microsc. 2000 May;198(Pt 2):82-7. PubMed PMID: 10810003.

Györke I, Györke S. Regulation of the cardiac ryanodine receptor channel by luminal Ca2+ involves luminal Ca2+ sensing sites. Biophys J. 1998 Dec;75(6):2801-10. PubMed PMID: 9826602; PubMed Central PMCID: PMC1299953.

Györke I, Hester N, Jones LR, Györke S. The role of calsequestrin, triadin, and junctin in conferring cardiac ryanodine receptor responsiveness to luminal calcium. Biophys J. 2004 Apr;86(4):2121-8. PubMed PMID: 15041652; PubMed Central PMCID: PMC1304063.

Györke S, Stevens SC, Terentyev D. Cardiac calsequestrin: quest inside the SR. J Physiol. 2009 Jul 1;587(Pt 13):3091-4. doi: 10.1113/jphysiol.2009.172049. Review. PubMed PMID: 19567748; PubMed Central PMCID: PMC2727018.

Hain J, Onoue H, Mayrleitner M, Fleischer S, Schindler H. Phosphorylation modulates the function of the calcium release channel of sarcoplasmic reticulum from cardiac muscle. J Biol Chem. 1995 Feb 3;270(5):2074-81. PubMed PMID: 7836435.

Hakamata Y, Nakai J, Takeshima H, Imoto K. Primary structure and distribution of a novel ryanodine receptor/calcium release channel from rabbit brain. FEBS Lett. 1992 Nov 9;312(2-3):229-35. PubMed PMID: 1330694.

Hake J, Edwards AG, Yu Z, Kekenes-Huskey PM, Michailova AP, McCammon JA, Holst MJ, Hoshijima M, McCulloch AD. Modelling cardiac calcium sparks in a three-dimensional reconstruction of a calcium release unit. J Physiol. 2012 Sep 15;590(Pt 18):4403-22. doi: 10.1113/jphysiol.2012.227926. Epub 2012 Apr 10. PubMed PMID: 22495592; PubMed Central PMCID: PMC3477749.

Hake J, Kekenes-Huskey PM, McCulloch AD. Computational modeling of subcellular transport and signaling. Curr Opin Struct Biol. 2014 Apr;25:92-7. doi: 10.1016/j.sbi.2014.01.006. Epub 2014 Feb 7. Review. PubMed PMID: 24509246; PubMed Central PMCID: PMC4040296.

Hasenfuss G. Alterations of calcium-regulatory proteins in heart failure. Cardiovasc Res. 1998 Feb;37(2):279-89. Review. PubMed PMID: 9614485.

Hayashi T, Martone ME, Yu Z, Thor A, Doi M, Holst MJ, Ellisman MH, Hoshijima M. Three-dimensional electron microscopy reveals new details of membrane systems for Ca2+ signaling in the heart. J Cell Sci. 2009 Apr 1;122(Pt 7):1005-13. doi: 10.1242/jcs.028175. PubMed PMID: 19295127; PubMed Central PMCID: PMC2720931.

Heilemann M, van de Linde S, Mukherjee A, Sauer M. Super-resolution imaging with small organic fluorophores. Angew Chem Int Ed Engl. 2009;48(37):6903-8. doi: 10.1002/anie.200902073. PubMed PMID: 19670280.

Heintzmann, Rainer, and Christoph G. Cremer. "Laterally modulated excitation microscopy: improvement of resolution by using a diffraction grating." *BiOS Europe'98* (1999): 185-196.

Hell S, Stelzer EHK. Fundamental improvement of resolution with a 4Pi-confocal fluorescence microscope using two-photon excitation. Opt. Comm. 1992;93:277–282.

Hell SW, Wichmann J. Breaking the diffraction resolution limit by stimulated emission: stimulated-emission-depletion fluorescence microscopy. Opt Lett. 1994 Jun 1;19(11):780-2. PubMed PMID: 19844443.

Hell SW. Far-field optical nanoscopy. Science. 2007 May 25;316(5828):1153-8. Review. PubMed PMID: 17525330.

Henderson SA, Goldhaber JI, So JM, Han T, Motter C, Ngo A, Chantawansri C, Ritter MR, Friedlander M, Nicoll DA, Frank JS, Jordan MC, Roos KP, Ross RS, Philipson KD. Functional adult myocardium in the absence of Na+-Ca2+ exchange: cardiac-specific knockout of NCX1. Circ Res. 2004 Sep 17;95(6):604-11. Epub 2004 Aug 12. PubMed PMID: 15308581.

Henriques R, Lelek M, Fornasiero EF, Valtorta F, Zimmer C, Mhlanga MM. QuickPALM: 3D real-time photoactivation nanoscopy image processing in ImageJ. Nat Methods. 2010 May;7(5):339-40. doi: 10.1038/nmeth0510-339. PubMed PMID: 20431545.

Hess ST, Girirajan TP, Mason MD. Ultra-high resolution imaging by fluorescence photoactivation localization microscopy. Biophys J. 2006 Dec 1;91(11):4258-72. Epub 2006 Sep 15. PubMed PMID: 16980368; PubMed Central PMCID: PMC1635685.

Huxley AF, Taylor RE. Local activation of striated muscle fibres. The Journal of physiology. 1958;144:426-41.

Huxley AF. Local activation of muscle. Annals of the New York Academy of Sciences. 1959;81:446-52.

Huxley HE. Evidence for Continuity between the Central Elements of the Triads and Extracellular Space in Frog Sartorius Muscle. Nature. 1964;202:1067-71.

Imagawa T, Smith JS, Coronado R, Campbell KP. Purified ryanodine receptor from skeletal muscle sarcoplasmic reticulum is the Ca2+-permeable pore of the calcium release channel. J Biol Chem. 1987 Dec 5;262(34):16636-43. PubMed PMID: 2445748.

Inui M, Saito A, Fleischer S. Isolation of the ryanodine receptor from cardiac sarcoplasmic reticulum and identity with the feet structures. The Journal of biological chemistry. 1987;262:15637-42.

Inui M, Saito A, Fleischer S. Purification of the ryanodine receptor and identity with feet structures of junctional terminal cisternae of sarcoplasmic reticulum from fast skeletal muscle. J Biol Chem. 1987 Feb 5;262(4):1740-7. PubMed PMID: 3805051.

Izu LT, Means SA, Shadid JN, Chen-Izu Y, Balke CW. Interplay of ryanodine receptor distribution and calcium dynamics. Biophysical Journal. 2006;91:95-112.

Jayasinghe I, Crossman D, Soeller C, Cannell M. Comparison of the organization of t-tubules, sarcoplasmic reticulum and ryanodine receptors in rat and human ventricular myocardium. Clin Exp Pharmacol Physiol. 2012;39:469-76.

Jayasinghe ID, Baddeley D, Kong CH, Wehrens XH, Cannell MB, Soeller C. Nanoscale organization of junctophilin-2 and ryanodine receptors within peripheral couplings of rat ventricular cardiomyocytes. Biophys J. 2012 Mar 7;102(5):L19-21. doi: 10.1016/j.bpj.2012.01.034. Epub 2012 Mar 6. PubMed PMID: 22404946; PubMed Central PMCID: PMC3296050.

Jayasinghe ID, Cannell MB, Soeller C. Organization of ryanodine receptors, transverse tubules, and sodium-calcium exchanger in rat myocytes. Biophys J.

2009 Nov 18;97(10):2664-73. doi: 10.1016/j.bpj.2009.08.036. PubMed PMID: 19917219; PubMed Central PMCID: PMC2776253.

Jessup M, Abraham WT, Casey DE, Feldman AM, Francis GS, Ganiats TG, Konstam MA, Mancini DM, Rahko PS, Silver MA, Stevenson LW, Yancy CW. 2009 focused update: ACCF/AHA Guidelines for the Diagnosis and Management of Heart Failure in Adults: a report of the American College of Cardiology Foundation/American Heart Association Task Force on Practice Guidelines: developed in collaboration with the International Society for Heart and Lung Transplantation. Circulation. 2009 Apr 14;119(14):1977-2016. doi: 10.1161/CIRCULATIONAHA.109.192064. Epub 2009 Mar 26. PubMed PMID: 19324967.

Jewett PH, Leonard SD, Sommer JR. Chicken cardiac muscle: its elusive extended junctional sarcoplasmic reticulum and sarcoplasmic reticulum fenestrations. The Journal of cell biology. 1973;56:595-600.

Jeyakumar LH, Ballester L, Cheng DS, McIntyre JO, Chang P, Olivey HE, Rollins-Smith L, Barnett JV, Murray K, Xin HB, Fleischer S. FKBP binding characteristics of cardiac microsomes from diverse vertebrates. Biochem Biophys Res Commun. 2001 Mar 9;281(4):979-86. PubMed PMID: 11237759.

John SA, Ribalet B, Weiss JN, Philipson KD, Ottolia M. Ca2+-dependent structural rearrangements within Na+-Ca2+ exchanger dimers. Proc Natl Acad Sci U S A. 2011 Jan 25;108(4):1699-704. doi: 10.1073/pnas.1016114108. Epub 2011 Jan 5. PubMed PMID: 21209335; PubMed Central PMCID: PMC3029690.

Johnson EA, Sommer JR. A strand of cardiac muscle. Its ultrastructure and the electrophysiological implications of its geometry. The Journal of cell biology.

Jorgensen AO, Shen AC, Arnold W, McPherson PS, Campbell KP. The Ca2+-release channel/ryanodine receptor is localized in junctional and corbular sarcoplasmic reticulum in cardiac muscle. J Cell Biol. 1993 Feb;120(4):969-80. PubMed PMID: 8381786; PubMed Central PMCID: PMC2200068.

Juette MF, Gould TJ, Lessard MD, Mlodzianoski MJ, Nagpure BS, Bennett BT, Hess ST, Bewersdorf J. Three-dimensional sub-100 nm resolution fluorescence microscopy of thick samples. Nat Methods. 2008 Jun;5(6):527-9. doi: 10.1038/nmeth.1211. Epub 2008 May 11. PubMed PMID: 18469823.

Kanngiesser U, Nalik P, Pongs O. Purification and affinity labeling of dihydropyridine receptor from rabbit skeletal muscle membranes. Proc Natl Acad Sci U S A. 1988 May;85(9):2969-73. PubMed PMID: 2834724; PubMed Central PMCID: PMC280124.

Kapiloff MS, Jackson N, Airhart N. mAKAP and the ryanodine receptor are part of a multi-component signaling complex on the cardiomyocyte nuclear envelope. J Cell Sci. 2001 Sep;114(Pt 17):3167-76. PubMed PMID: 11590243.

Kentish JC, McCloskey DT, Layland J, Palmer S, Leiden JM, Martin AF, Solaro RJ. Phosphorylation of troponin I by protein kinase A accelerates relaxation and crossbridge cycle kinetics in mouse ventricular muscle. Circ Res. 2001 May 25;88(10):1059-65. PubMed PMID: 11375276.

Keppler A, Gendreizig S, Gronemeyer T, Pick H, Vogel H, Johnsson K. A general method for the covalent labeling of fusion proteins with small molecules in vivo. Nat Biotechnol. 2003 Jan;21(1):86-9. Epub 2002 Dec 9. PubMed PMID: 12469133.

Kim D, Deerinck TJ, Sigal YM, Babcock HP, Ellisman MH, Zhuang X. Correlative stochastic optical reconstruction microscopy and electron microscopy. PLoS One. 2015 Apr 15;10(4):e0124581. doi: 10.1371/journal.pone.0124581. eCollection 2015. PubMed PMID: 25874453; PubMed Central PMCID: PMC4398493.

Klar TA, Hell SW. Subdiffraction resolution in far-field fluorescence microscopy. Opt Lett. 1999 Jul 15;24(14):954-6. PubMed PMID: 18073907.

Klein T, Löschberger A, Proppert S, Wolter S, van de Linde S, Sauer M. Live-cell dSTORM with SNAP-tag fusion proteins. Nat Methods. 2011 Jan;8(1):7-9. doi: 10.1038/nmeth0111-7b. PubMed PMID: 21191367.

Knoll, Max (1935). "Aufladepotentiel und Sekundäremission elektronenbestrahlter Körper". *Zeitschrift für technische Physik***16**: 467–475.

Koh X, Srinivasan B, Ching HS, Levchenko A. A 3D Monte Carlo analysis of the role of dyadic space geometry in spark generation. Biophysical Journal. 2006;90:1999-2014.

Kopek BG, Shtengel G, Xu CS, Clayton DA, Hess HF. Correlative 3D superresolution fluorescence and electron microscopy reveal the relationship of mitochondrial nucleoids to membranes. Proceedings of the National Academy of Sciences of the United States of America. 2012;109:6136-41.

Kremer JR, Mastronarde DN, McIntosh JR. Computer visualization of three-dimensional image data using IMOD. J Struct Biol. 1996 Jan-Feb;116(1):71-6. PubMed PMID: 8742726.

Kreshuk A, Koethe U, Pax E, Bock DD, Hamprecht FA. Automated detection of synapses in serial section transmission electron microscopy image stacks. PLoS One. 2014 Feb 6;9(2):e87351. doi: 10.1371/journal.pone.0087351. eCollection 2014. PubMed PMID: 24516550; PubMed Central PMCID: PMC3916342.

Ladinsky MS, Howell KE. Electron tomography of immunolabeled cryosections. Methods in cell biology. 2007;79:543-58.

Lai FA, Dent M, Wickenden C, Xu L, Kumari G, Misra M, Lee HB, Sar M, Meissner G. Expression of a cardiac Ca(2+)-release channel isoform in

mammalian brain. Biochem J. 1992 Dec 1;288 (Pt 2):553-64. PubMed PMID: 1334409; PubMed Central PMCID: PMC1132046.

Lai FA, Erickson HP, Rousseau E, Liu QY, Meissner G. Purification and reconstitution of the calcium release channel from skeletal muscle. Nature. 1988 Jan 28;331(6154):315-9. PubMed PMID: 2448641.

Landstrom AP, Kellen CA, Dixit SS, van Oort RJ, Garbino A, Weisleder N, Ma J, Wehrens XH, Ackerman MJ. Junctophilin-2 expression silencing causes cardiocyte hypertrophy and abnormal intracellular calcium-handling. Circ Heart Fail. 2011 Mar;4(2):214-23. doi: 10.1161/CIRCHEARTFAILURE.110.958694. Epub 2011 Jan 7. PubMed PMID: 21216834; PubMed Central PMCID: PMC3059380.

Landstrom AP, Weisleder N, Batalden KB, Bos JM, Tester DJ, Ommen SR, Wehrens XH, Claycomb WC, Ko JK, Hwang M, Pan Z, Ma J, Ackerman MJ. Mutations in JPH2-encoded junctophilin-2 associated with hypertrophic cardiomyopathy in humans. J Mol Cell Cardiol. 2007 Jun;42(6):1026-35. Epub 2007 Apr 18. PubMed PMID: 17509612; PubMed Central PMCID: PMC4318564.

Langer GA, Peskoff A. Calcium concentration and movement in the diadic cleft space of the cardiac ventricular cell. Biophysical Journal. 1996;70:1169-82.

Laver DR, Baynes TM, Dulhunty AF. Magnesium inhibition of ryanodine-receptor calcium channels: evidence for two independent mechanisms. J Membr Biol. 1997 Apr 1;156(3):213-29. PubMed PMID: 9096063.

Laver DR, Honen BN. Luminal Mg2+, a key factor controlling RYR2-mediated Ca2+ release: cytoplasmic and luminal regulation modeled in a tetrameric channel. J Gen Physiol. 2008 Oct;132(4):429-46. doi: 10.1085/jgp.200810001. PubMed PMID: 18824590; PubMed Central PMCID: PMC2553390.

Laver DR, O'Neill ER, Lamb GD. Luminal Ca2+-regulated Mg2+ inhibition of skeletal RyRs reconstituted as isolated channels or coupled clusters. J Gen Physiol. 2004 Dec;124(6):741-58. Epub 2004 Nov 15. PubMed PMID: 15545399; PubMed Central PMCID: PMC2234024.

Laver DR. Ca2+ stores regulate ryanodine receptor Ca2+ release channels via luminal and cytosolic Ca2+ sites. Biophys J. 2007 May 15;92(10):3541-55. Epub 2007 Mar 9. PubMed PMID: 17351009; PubMed Central PMCID: PMC1853142.

Laver DR. Regulation of RyR Channel Gating by Ca(2+), Mg(2+) and ATP. Curr Top Membr. 2010;66:69-89. doi: 10.1016/S1063-5823(10)66004-8. Epub 2010 Jul 25. PubMed PMID: 22353477.

Lederer WJ, Niggli E, Hadley RW. Sodium-calcium exchange in excitable cells: fuzzy space. Science. 1990;248:283.

Lee E, Marcucci M, Daniell L, Pypaert M, Weisz OA, Ochoa GC, Farsad K, Wenk MR, De Camilli P. Amphiphysin 2 (Bin1) and T-tubule biogenesis in muscle. Science. 2002 Aug 16;297(5584):1193-6. PubMed PMID: 12183633.

Lewis, A. M. A. A., et al. "Development of a 500 Å spatial resolution light microscope: I. light is efficiently transmitted through λ/16 diameter apertures."*Ultramicroscopy* 13.3 (1984): 227-231.

Li L, Desantiago J, Chu G, Kranias EG, Bers DM. Phosphorylation of phospholamban and troponin I in beta-adrenergic-induced acceleration of cardiac relaxation. Am J Physiol Heart Circ Physiol. 2000 Mar;278(3):H769-79. PubMed PMID: 10710345.

Lipp P, Egger M, Niggli E. Spatial characteristics of sarcoplasmic reticulum Ca2+ release events triggered by L-type Ca2+ current and Na+ current in guinea-pig cardiac myocytes. J Physiol. 2002 Jul 15;542(Pt 2):383-93. PubMed PMID: 12122139; PubMed Central PMCID: PMC2290414.

Lipp P, Niggli E. Fundamental calcium release events revealed by two-photon excitation photolysis of caged calcium in Guinea-pig cardiac myocytes. The Journal of physiology. 1998;508 (Pt 3):801-9.

Lokuta AJ, Rogers TB, Lederer WJ, Valdivia HH. Modulation of cardiac ryanodine receptors of swine and rabbit by a phosphorylation-dephosphorylation mechanism. J Physiol. 1995 Sep 15;487 (Pt 3):609-22. PubMed PMID: 8544125; PubMed Central PMCID: PMC1156649.

Los GV, Encell LP, McDougall MG, Hartzell DD, Karassina N, Zimprich C, Wood MG, Learish R, Ohana RF, Urh M, Simpson D, Mendez J, Zimmerman K, Otto P, Vidugiris G, Zhu J, Darzins A, Klaubert DH, Bulleit RF, Wood KV. HaloTag: a novel protein labeling technology for cell imaging and protein analysis. ACS Chem Biol. 2008 Jun 20;3(6):373-82. doi: 10.1021/cb800025k. PubMed PMID: 18533659.

Louch WE, Bito V, Heinzel FR, Macianskiene R, Vanhaecke J, Flameng W, Mubagwa K, Sipido KR. Reduced synchrony of Ca2+ release with loss of T-tubules-a comparison to Ca2+ release in human failing cardiomyocytes. Cardiovasc Res. 2004 Apr 1;62(1):63-73. PubMed PMID: 15023553.

Louch WE, Hake J, Mørk HK, Hougen K, Skrbic B, Ursu D, Tønnessen T, Sjaastad I, Sejersted OM. Slow Ca^{2+} sparks de-synchronize Ca^{2+} release in failing cardiomyocytes: evidence for altered configuration of Ca^{2+} release units? J Mol Cell Cardiol. 2013 May;58:41-52. doi: 10.1016/j.yjmcc.2013.01.014. Epub 2013 Jan 30. PubMed PMID: 23376034.

Lu L, Xia L, Zhu X. Simulation of arrhythmogenic effect of rogue RyRs in failing heart by using a coupled model. Comput Math Methods Med. 2012;2012:183978. doi: 10.1155/2012/183978. Epub 2012 Sep 29. PubMed PMID: 23056145; PubMed Central PMCID: PMC3465912.

Manley S, Gillette JM, Patterson GH, Shroff H, Hess HF, Betzig E, Lippincott-Schwartz J. High-density mapping of single-molecule trajectories with photoactivated localization microscopy. Nat Methods. 2008 Feb;5(2):155-7. doi: 10.1038/nmeth.1176. Epub 2008 Jan 13. PubMed PMID: 18193054.

Mann DL. Mechanisms and models in heart failure: A combinatorial approach. Circulation. 1999 Aug 31;100(9):999-1008. Review. PubMed PMID: 10468532.

Martinez-Sanchez A, Garcia I, Fernandez JJ. A ridge-based framework for segmentation of 3D electron microscopy datasets. J Struct Biol. 2013 Jan;181(1):61-70. doi: 10.1016/j.jsb.2012.10.002. Epub 2012 Oct 17. PubMed PMID: 23085430.

Marx SO, Gaburjakova J, Gaburjakova M, Henrikson C, Ondrias K, Marks AR. Coupled gating between cardiac calcium release channels (ryanodine receptors). Circ Res. 2001 Jun 8;88(11):1151-8. PubMed PMID: 11397781.

Marx SO, Ondrias K, Marks AR. Coupled gating between individual skeletal muscle Ca2+ release channels (ryanodine receptors). Science. 1998 Aug 7;281(5378):818-21. PubMed PMID: 9694652.

Marx SO, Reiken S, Hisamatsu Y, Gaburjakova M, Gaburjakova J, Yang YM, Rosemblit N, Marks AR. Phosphorylation-dependent regulation of ryanodine receptors: a novel role for leucine/isoleucine zippers. J Cell Biol. 2001 May 14;153(4):699-708. PubMed PMID: 11352932; PubMed Central PMCID: PMC2192391.

Marx SO, Reiken S, Hisamatsu Y, Jayaraman T, Burkhoff D, Rosemblit N, Marks AR. PKA phosphorylation dissociates FKBP12.6 from the calcium release channel (ryanodine receptor): defective regulation in failing hearts. Cell. 2000 May 12;101(4):365-76. PubMed PMID: 10830164.

Matsko N, Mueller M. Epoxy resin as fixative during freeze-substitution. J Struct Biol. 2005 Nov;152(2):92-103. Epub 2005 Aug 19. PubMed PMID: 16214372.

Maxfield FR. Plasma membrane microdomains. Curr Opin Cell Biol. 2002 Aug;14(4):483-7. Review. PubMed PMID: 12383800.

McCall E, Li L, Satoh H, Shannon TR, Blatter LA, Bers DM. Effects of FK-506 on contraction and Ca2+ transients in rat cardiac myocytes. Circ Res. 1996 Dec;79(6):1110-21. PubMed PMID: 8943949.

McIntosh JR. Electron microscopy of cells: a new beginning for a new century. J Cell Biol. 2001 Jun 11;153(6):F25-32. Review. PubMed PMID: 11402057; PubMed Central PMCID: PMC2192021.

Meissner G, Darling E, Eveleth J. Kinetics of rapid Ca2+ release by sarcoplasmic reticulum. Effects of Ca2+, Mg2+, and adenine nucleotides. Biochemistry. 1986 Jan 14;25(1):236-44. PubMed PMID: 3754147.

Meissner G, Henderson JS. Rapid calcium release from cardiac sarcoplasmic reticulum vesicles is dependent on Ca2+ and is modulated by Mg2+, adenine nucleotide, and calmodulin. J Biol Chem. 1987 Mar 5;262(7):3065-73. PubMed PMID: 2434495.

Micheva KD, O'Rourke N, Busse B, Smith SJ. Array tomography: high-resolution three-dimensional immunofluorescence. Cold Spring Harb Protoc. 2010 Nov 1;2010(11):pdb.top89. doi: 10.1101/pdb.top89. PubMed PMID: 21041404.

Micheva KD, Smith SJ. Array tomography: a new tool for imaging the molecular architecture and ultrastructure of neural circuits. Neuron. 2007 Jul 5;55(1):25-36. Erratum in: Neuron. 2007 Sep 6;55(5):824. PubMed PMID: 17610815; PubMed Central PMCID: PMC2080672.

Minamisawa S, Oshikawa J, Takeshima H, Hoshijima M, Wang Y, Chien KR, Ishikawa Y, Matsuoka R. Junctophilin type 2 is associated with caveolin-3 and is down-regulated in the hypertrophic and dilated cardiomyopathies. Biochem Biophys Res Commun. 2004 Dec 17;325(3):852-6. PubMed PMID: 15541368.

Moneron G, Medda R, Hein B, Giske A, Westphal V, Hell SW. Fast STED microscopy with continuous wave fiber lasers. Opt Express. 2010 Jan 18;18(2):1302-9. doi: 10.1364/OE.18.001302. PubMed PMID: 20173956.

Moore DH, Ruska H. Electron microscope study of mammalian cardiac muscle cells. J Biophys Biochem Cytol. 1957;3:261-8.

Müller SA, Aebi U, Engel A. What transmission electron microscopes can visualize now and in the future. J Struct Biol. 2008 Sep;163(3):235-45. doi: 10.1016/j.jsb.2008.05.008. Epub 2008 Jun 18. Review. PubMed PMID: 18614377.

Nakai J, Imagawa T, Hakamat Y, Shigekawa M, Takeshima H, Numa S. Primary structure and functional expression from cDNA of the cardiac ryanodine receptor/calcium release channel. FEBS Lett. 1990 Oct 1;271(1-2):169-77. PubMed PMID: 2226801.

Nanguneri S, Flottmann B, Horstmann H, Heilemann M, Kuner T. Three-dimensional, tomographic super-resolution fluorescence imaging of serially sectioned thick samples. PLoS One. 2012;7(5):e38098. doi: 10.1371/journal.pone.0038098. Epub 2012 May 25. PubMed PMID: 22662272; PubMed Central PMCID: PMC3360663.

Nelson DA, Benson ES. On the structural continuities of the transverse tubular system of rabbit and human myocardial cells. The Journal of cell biology. 1963;16:297-313.

Niggli E, Lipp P. Subcellular restricted spaces: significance for cell signalling and excitation-contraction coupling. Journal of muscle research and cell motility. 1993;14:288-91.

Nishi M, Sakagami H, Komazaki S, Kondo H, Takeshima H. Coexpression of junctophilin type 3 and type 4 in brain. Brain Res Mol Brain Res. 2003 Oct 21;118(1-2):102-10. PubMed PMID: 14559359.

Nitsch M, Walz J, Typke D, Klumpp M, Essen LO, Baumeister W. Group II chaperonin in an open conformation examined by electron tomography. Nat Struct Biol. 1998 Oct;5(10):855-7. PubMed PMID: 9783741.

Otsu K, Willard HF, Khanna VK, Zorzato F, Green NM, MacLennan DH. Molecular cloning of cDNA encoding the Ca2+ release channel (ryanodine receptor) of rabbit cardiac muscle sarcoplasmic reticulum. J Biol Chem. 1990 Aug 15;265(23):13472-83. PubMed PMID: 2380170.

Page E, Surdyk-Droske M. Distribution, surface density, and membrane area of diadic junctional contacts between plasma membrane and terminal cisterns in mammalian ventricle. Circ Res. 1979 Aug;45(2):260-7. PubMed PMID: 376173.

Page SG, Niedergerke R. Structures of physiological interest in the frog heart ventricle. J Cell Sci. 1972 Jul;11(1):179-203. PubMed PMID: 4538490.

Page SG. A comparison of the fine structures of frog slow and twitch muscle fibers. The Journal of cell biology. 1965;26:477-97.

Pare GC, Easlick JL, Mislow JM, McNally EM, Kapiloff MS. Nesprin-1alpha contributes to the targeting of mAKAP to the cardiac myocyte nuclear envelope. Exp Cell Res. 2005 Feb 15;303(2):388-99. PubMed PMID: 15652351.

Parton RG, Way M, Zorzi N, Stang E. Caveolin-3 associates with developing T-tubules during muscle differentiation. J Cell Biol. 1997 Jan 13;136(1):137-54. PubMed PMID: 9008709; PubMed Central PMCID: PMC2132459.

Peachey LD. The sarcoplasmic reticulum and transverse tubules of the frog's sartorius. J Cell Biol. 1965;25:Suppl:209-31.

Peddie CJ, Collinson LM. Exploring the third dimension: volume electron microscopy comes of age. Micron. 2014 Jun;61:9-19. doi: 10.1016/j.micron.2014.01.009. Epub 2014 Feb 12. PubMed PMID: 24792442.

Peng S, Publicover NG, Airey JA, Hall JE, Haigler HT, Jiang D, Chen SR, Sutko JL. Diffusion of single cardiac ryanodine receptors in lipid bilayers is decreased by annexin 12. Biophys J. 2004 Jan;86(1 Pt 1):145-51. PubMed PMID: 14695258; PubMed Central PMCID: PMC1303778.

Peng S, Publicover NG, Airey JA, Hall JE, Haigler HT, Jiang D, et al. Diffusion of single cardiac ryanodine receptors in lipid bilayers is decreased by annexin 12. Biophysical Journal. 2004;86:145-51.

Perkins GA, Renken CW, Frey TG, Ellisman MH. Membrane architecture of mitochondria in neurons of the central nervous system. J Neurosci Res. 2001 Dec 1;66(5):857-65. PubMed PMID: 11746412.

Pettersen EF, Goddard TD, Huang CC, Couch GS, Greenblatt DM, Meng EC, Ferrin TE. UCSF Chimera--a visualization system for exploratory research and analysis. J Comput Chem. 2004 Oct;25(13):1605-12. PubMed PMID: 15264254.

Phan S, Lawrence A, Molina T, Lanman J, Berlanga M, Terada M, Kulungowski A, Obayashi J, Ellisman M. TxBR montage reconstruction for large field electron tomography. J Struct Biol. 2012 Oct;180(1):154-64. doi: 10.1016/j.jsb.2012.06.006. Epub 2012 Jun 27. PubMed PMID: 22749959.

Phimister AJ, Lango J, Lee EH, Ernst-Russell MA, Takeshima H, Ma J, Allen PD, Pessah IN. Conformation-dependent stability of junctophilin 1 (JP1) and ryanodine receptor type 1 (RyR1) channel complex is mediated by their hyper-reactive thiols. J Biol Chem. 2007 Mar 23;282(12):8667-77. Epub 2007 Jan 19. PubMed PMID: 17237236.

Pohl, Dieter W., W. Denk, and M. Lanz. "Optical stethoscopy: Image recording with resolution λ/20." *Applied physics letters* 44.7 (1984): 651-653.

Porter KR, Palade GE. Studies on the endoplasmic reticulum. III. Its form and distribution in striated muscle cells. J Biophys Biochem Cytol. 1957;3:269-300.

Porter KR. The sarcoplasmic reticulum. Its recent history and present status. J Biophys Biochem Cytol. 1961;10(4)Suppl:219-26.research. 1954;7:130-46.

Pott C, Philipson KD, Goldhaber JI. Excitation-contraction coupling in Na+-Ca2+ exchanger knockout mice: reduced transsarcolemmal Ca2+ flux. Circ Res. 2005 Dec 9;97(12):1288-95. Epub 2005 Nov 17. PubMed PMID: 16293789; PubMed Central PMCID: PMC1790864.

Prestle J, Janssen PM, Janssen AP, Zeitz O, Lehnart SE, Bruce L, Smith GL, Hasenfuss G. Overexpression of FK506-binding protein FKBP12.6 in cardiomyocytes reduces ryanodine receptor-mediated Ca(2+) leak from the sarcoplasmic reticulum and increases contractility. Circ Res. 2001 Feb 2;88(2):188-94. PubMed PMID: 11157671.

Protasi F, Sun XH, Franzini-Armstrong C. Formation and maturation of the calcium release apparatus in developing and adult avian myocardium. Developmental biology. 1996;173:265-78.

R, Williams AJ. Regulation of the gating of the sheep cardiac sarcoplasmic reticulum Ca(2+)-release channel by luminal Ca2+. J Membr Biol. 1994 Feb;137(3):215-26. PubMed PMID: 8182731.

Radermacher M, Rao V, Grassucci R, Frank J, Timerman AP, Fleischer S, Wagenknecht T. Cryo-electron microscopy and three-dimensional reconstruction of the calcium release channel/ryanodine receptor from skeletal muscle. J Cell Biol. 1994 Oct;127(2):411-23. PubMed PMID: 7929585; PubMed Central PMCID: PMC2120200.

Radermacher M, Wagenknecht T, Grassucci R, Frank J, Inui M, Chadwick C, Fleischer S. Cryo-EM of the native structure of the calcium release channel/ryanodine receptor from sarcoplasmic reticulum. Biophys J. 1992 Apr;61(4):936-40. PubMed PMID: 1316182; PubMed Central PMCID: PMC1260352.

Rayleigh, L. 1896. On the theory of optical images, with special reference to the microscope. Philos. Mag. 42:167–195.

Reiken S, Lacampagne A, Zhou H, Kherani A, Lehnart SE, Ward C, Huang F, Gaburjakova M, Gaburjakova J, Rosemblit N, Warren MS, He KL, Yi GH, Wang J, Burkhoff D, Vassort G, Marks AR. PKA phosphorylation activates the calcium release channel (ryanodine receptor) in skeletal muscle: defective regulation in heart failure. J Cell Biol. 2003 Mar 17;160(6):919-28. Epub 2003 Mar 10. PubMed PMID: 12629052; PubMed Central PMCID: PMC2173774.

Renken C, Hsieh CE, Marko M, Rath B, Leith A, Wagenknecht T, Frank J, Mannella CA. Structure of frozen-hydrated triad junctions: a case study in motif searching inside tomograms. J Struct Biol. 2009 Feb;165(2):53-63. doi: 10.1016/j.jsb.2008.09.011. Epub 2008 Nov 5. PubMed PMID: 19028586; PubMed Central PMCID: PMC2655133.

Reuter H, Seitz N. The dependence of calcium efflux from cardiac muscle on temperature and external ion composition. J Physiol. 1968 Mar;195(2):451-70. PubMed PMID: 5647333; PubMed Central PMCID: PMC1351672.

Revel JP. The sarcoplasmic reticulum of the bat cricothroid muscle. The Journal of cell biology. 1962;12:571-88.

Rieder, Conly L. "Thick and thin serial sectioning for the three-dimensional reconstruction of biological ultrastructure." *Methods in cell biology* 22 (1981): 215.

Ries J, Kaplan C, Platonova E, Eghlidi H, Ewers H. A simple, versatile method for GFP-based super-resolution microscopy via nanobodies. Nat Methods. 2012 Jun;9(6):582-4. doi: 10.1038/nmeth.1991. Epub 2012 Apr 29. PubMed PMID: 22543348.

Ringer S. A further Contribution regarding the influence of the different Constituents of the Blood on the Contraction of the Heart. The Journal of physiology. 1883;4:29-42 3.

Robertson JD. Some features of the ultrastructure of reptilian skeletal muscle. J Biophys Biochem Cytol. 1956;2:369-80.

Roger VL, Go AS, Lloyd-Jones DM, Benjamin EJ, Berry JD, Borden WB, Bravata DM, Dai S, Ford ES, Fox CS, Fullerton HJ, Gillespie C, Hailpern SM, Heit JA, Howard VJ, Kissela BM, Kittner SJ, Lackland DT, Lichtman JH, Lisabeth LD, Makuc DM, Marcus GM, Marelli A, Matchar DB, Moy CS, Mozaffarian D, Mussolino ME, Nichol G, Paynter NP, Soliman EZ, Sorlie PD, Sotoodehnia N, Turan TN, Virani SS, Wong ND, Woo D, Turner MB; American Heart Association Statistics Committee and Stroke Statistics Subcommittee. Executive summary: heart disease and stroke statistics--2012 update: a report from the American Heart Association. Circulation. 2012 Jan 3;125(1):188-97. doi: 10.1161/CIR.0b013e3182456d46. Erratum in: Circulation. 2012 Jun 5;125(22):e1001. PubMed PMID: 22215894.

Rothberg KG, Heuser JE, Donzell WC, Ying YS, Glenney JR, Anderson RG. Caveolin, a protein component of caveolae membrane coats. Cell. 1992 Feb 21;68(4):673-82. PubMed PMID: 1739974.

Rothberg, Karen G., et al. "Caveolin, a protein component of caveolae membrane coats." *Cell* 68.4 (1992): 673-682.

Rust MJ, Bates M, Zhuang X. Sub-diffraction-limit imaging by stochastic optical reconstruction microscopy (STORM). Nat Methods. 2006 Oct;3(10):793-5. Epub 2006 Aug 9. PubMed PMID: 16896339; PubMed Central PMCID: PMC2700296.

Schermelleh L, Heintzmann R, Leonhardt H. A guide to super-resolution fluorescence microscopy. The Journal of cell biology. 2010;190:165-75.

Schmidt R, Wurm CA, Jakobs S, Engelhardt J, Egner A, Hell SW. Spherical nanosized focal spot unravels the interior of cells. Nat Methods. 2008 Jun;5(6):539-44. doi: 10.1038/nmeth.1214. Epub 2008 May 18. PubMed PMID: 18488034.

Schmidt R, Wurm CA, Punge A, Egner A, Jakobs S, Hell SW. Mitochondrial cristae revealed with focused light. Nano Lett. 2009 Jun;9(6):2508-10. doi: 10.1021/nl901398t. PubMed PMID: 19459703.

Schulson MN, Scriven DR, Fletcher P, Moore ED. Couplons in rat atria form distinct subgroups defined by their molecular partners. J Cell Sci. 2011 Apr 1;124(Pt 7):1167-74. doi: 10.1242/jcs.080929. Epub 2011 Mar 8. PubMed PMID: 21385843; PubMed Central PMCID: PMC3056609.

Scriven DR, Asghari P, Schulson MN, Moore ED. Analysis of Cav1.2 and ryanodine receptor clusters in rat ventricular myocytes. Biophys J. 2010 Dec

15;99(12):3923-9. doi: 10.1016/j.bpj.2010.11.008. PubMed PMID: 21156134; PubMed Central PMCID: PMC3000512.

Scriven DR, Dan P, Moore ED. Distribution of proteins implicated in excitation-contraction coupling in rat ventricular myocytes. Biophys J. 2000 Nov;79(5):2682-91. PubMed PMID: 11053140; PubMed Central PMCID: PMC1301148.

Scriven DR, Klimek A, Asghari P, Bellve K, Moore ED. Caveolin-3 is adjacent to a group of extradyadic ryanodine receptors. Biophys J. 2005 Sep;89(3):1893-901. Epub 2005 Jun 24. PubMed PMID: 15980179; PubMed Central PMCID: PMC1366692.

Sedarat F, Xu L, Moore ED, Tibbits GF. Colocalization of dihydropyridine and ryanodine receptors in neonate rabbit heart using confocal microscopy. Am J Physiol Heart Circ Physiol. 2000 Jul;279(1):H202-9. PubMed PMID: 10899057.

Sedat, JOHN W. "Fluorescence microscopy in three dimensions." Methods in cell biology, VOL 30Cth: Fluorescence microscopy of living cells in culture, Part B: Quantitative fluorescence microscopy-imaging and spectroscopy. (1989):353

Serysheva II, Orlova EV, Chiu W, Sherman MB, Hamilton SL, van Heel M. Electron cryomicroscopy and angular reconstitution used to visualize the skeletal muscle calcium release channel. Nat Struct Biol. 1995 Jan;2(1):18-24. PubMed PMID: 7719847.

Sharma MR, Penczek P, Grassucci R, Xin HB, Fleischer S, Wagenknecht T. Cryoelectron microscopy and image analysis of the cardiac ryanodine receptor. J Biol Chem. 1998 Jul 17;273(29):18429-34. PubMed PMID: 9660811.

Shroff H, Galbraith CG, Galbraith JA, Betzig E. Live-cell photoactivated localization microscopy of nanoscale adhesion dynamics. Nat Methods. 2008 May;5(5):417-23. doi: 10.1038/nmeth.1202. Epub 2008 Apr 13. PubMed PMID: 18408726.

Shroff H, Galbraith CG, Galbraith JA, White H, Gillette J, Olenych S, Davidson MW, Betzig E. Dual-color superresolution imaging of genetically expressed probes within individual adhesion complexes. Proc Natl Acad Sci U S A. 2007 Dec 18;104(51):20308-13. Epub 2007 Dec 12. Erratum in: Proc Natl Acad Sci U S A. 2008 Sep 30;105(39):15220. PubMed PMID: 18077327; PubMed Central PMCID: PMC2154427.

Shu X, Lev-Ram V, Deerinck TJ, Qi Y, Ramko EB, Davidson MW, Jin Y, Ellisman MH, Tsien RY. A genetically encoded tag for correlated light and electron microscopy of intact cells, tissues, and organisms. PLoS Biol. 2011 Apr;9(4):e1001041. doi: 10.1371/journal.pbio.1001041. Epub 2011 Apr 5. PubMed PMID: 21483721; PubMed Central PMCID: PMC3071375.

Simons K, Ikonen E. Functional rafts in cell membranes. Nature. 1997 Jun 5;387(6633):569-72. Review. PubMed PMID: 9177342.

Simpson FO, Oertelis SJ. The fine structure of sheep myocardial cells; sarcolemmal invaginations and the transverse tubular system. The Journal of cell biology. 1962;12:91-100.

Sitsapesan R, Williams AJ. The gating of the sheep skeletal sarcoplasmic reticulum Ca(2+)-release channel is regulated by luminal Ca2+. J Membr Biol. 1995 Jul;146(2):133-44. PubMed PMID: 7473684.

Sjaastad I, Wasserstrom JA, Sejersted OM. Heart failure -- a challenge to our current concepts of excitation-contraction coupling. J Physiol. 2003 Jan 1;546(Pt 1):33-47. Review. PubMed PMID: 12509477; PubMed Central PMCID: PMC2342477.

Sjöstrand, F. S. "Ultrastructure of retinal rod synapses of the guinea pig eye as revealed by three-dimensional reconstructions from serial sections." *Journal of ultrastructure research* 2.1 (1958): 122-170.

Smart EJ, Graf GA, McNiven MA, Sessa WC, Engelman JA, Scherer PE, Okamoto T, Lisanti MP. Caveolins, liquid-ordered domains, and signal transduction. Mol Cell Biol. 1999 Nov;19(11):7289-304. Review. PubMed PMID: 10523618; PubMed Central PMCID: PMC84723.

Smith JS, Coronado R, Meissner G. Single channel measurements of the calcium release channel from skeletal muscle sarcoplasmic reticulum. Activation by Ca2+ and ATP and modulation by Mg2+. J Gen Physiol. 1986 Nov;88(5):573-88. PubMed PMID: 2431098; PubMed Central PMCID: PMC2228852.

Sobie EA, Guatimosim S, Gómez-Viquez L, Song LS, Hartmann H, Saleet Jafri M, Lederer WJ. The Ca 2+ leak paradox and rogue ryanodine receptors: SR Ca 2+ efflux theory and practice. Prog Biophys Mol Biol. 2006 Jan-Apr;90(1-3):172-85. Epub 2005 Jul 18. Review. PubMed PMID: 16326215; PubMed Central PMCID: PMC1484520.

Soeller C, Cannell MB. Numerical simulation of local calcium movements during L-type calcium channel gating in the cardiac diad. Biophysical Journal. 1997;73:97-111.

Soeller C, Crossman D, Gilbert R, Cannell MB. Analysis of ryanodine receptor clusters in rat and human cardiac myocytes. Proc Natl Acad Sci U S A. 2007 Sep18;104(38):14958-63. Epub 2007 Sep 11. PubMed PMID: 17848521; PubMed Central PMCID: PMC1986595.

Sommer JR, Waugh RA. The ultrastructure of the mammalian cardiac muscle cell--with special emphasis on the tubular membrane systems. A review. Am J Pathol. 1976;82:192-232.

Song KS, Scherer PE, Tang Z, Okamoto T, Li S, Chafel M, Chu C, Kohtz DS, Lisanti MP. Expression of caveolin-3 in skeletal, cardiac, and smooth muscle cells. Caveolin-3 is a component of the sarcolemma and co-fractionates with

dystrophin and dystrophin-associated glycoproteins. J Biol Chem. 1996 Jun 21;271(25):15160-5. PubMed PMID: 8663016.

Song LS, Sobie EA, McCulle S, Lederer WJ, Balke CW, Cheng H. Orphaned ryanodine receptors in the failing heart. Proc Natl Acad Sci U S A. 2006 Mar 14;103(11):4305-10. Epub 2006 Mar 6. PubMed PMID: 16537526; PubMed Central PMCID: PMC1449688.

Sorrentino V, Volpe P. Ryanodine receptors: how many, where and why? Trends Pharmacol Sci. 1993 Mar;14(3):98-103. Review. PubMed PMID: 8387707.

Sosinsky GE, Crum J, Jones YZ, Lanman J, Smarr B, Terada M, Martone ME, Deerinck TJ, Johnson JE, Ellisman MH. The combination of chemical fixation procedures with high pressure freezing and freeze substitution preserves highly labile tissue ultrastructure for electron tomography applications. J Struct Biol. 2008 Mar;161(3):359-71. Epub 2007 Sep 14. PubMed PMID: 17962040; PubMed Central PMCID: PMC2459253.

Stern MD, Pizarro G, Rios E. Local control model of excitation-contraction coupling in skeletal muscle. J Gen Physiol. 1997;110:415-40.

Stern MD. Theory of excitation-contraction coupling in cardiac muscle. Biophys J. 1992 Aug;63(2):497-517. PubMed PMID: 1330031; PubMed Central PMCID: PMC1262173.

Sun XH, Protasi F, Takahashi M, Takeshima H, Ferguson DG, Franzini-Armstrong C. Molecular architecture of membranes involved in excitation-contraction coupling of cardiac muscle. J Cell Biol. 1995 May;129(3):659-71. PubMed PMID: 7730402; PubMed Central PMCID: PMC2120446.

Takekura H, Takeshima H, Nishimura S, Takahashi M, Tanabe T, Flockerzi V, et al. Co-expression in CHO cells of two muscle proteins involved in excitation-contraction coupling. J Muscle Res Cell Motil. 1995;16:465-80.

Takeshima H, Nishimura S, Matsumoto T, Ishida H, Kangawa K, Minamino N, Matsuo H, Ueda M, Hanaoka M, Hirose T, et al. Primary structure and expression from complementary DNA of skeletal muscle ryanodine receptor. Nature. 1989 Jun 8;339(6224):439-45. PubMed PMID: 2725677.

Tanskanen AJ, Greenstein JL, Chen A, Sun SX, Winslow RL. Protein geometry and placement in the cardiac dyad influence macroscopic properties of calcium-induced calcium release. Biophysical Journal. 2007;92:3379-96.

Thomas MJ, Sjaastad I, Andersen K, Helm PJ, Wasserstrom JA, Sejersted OM, Ottersen OP. Localization and function of the Na+/Ca2+-exchanger in normal and detubulated rat cardiomyocytes. J Mol Cell Cardiol. 2003 Nov;35(11):1325-37. PubMed PMID: 14596789.

Thompson RE, Larson DR, Webb WW. Precise nanometer localization analysis for individual fluorescent probes. Biophys J. 2002 May;82(5):2775-83. PubMed PMID: 11964263; PubMed Central PMCID: PMC1302065.

Timerman AP, Ogunbumni E, Freund E, Wiederrecht G, Marks AR, Fleischer S. The calcium release channel of sarcoplasmic reticulum is modulated by FK-506-binding protein. Dissociation and reconstitution of FKBP-12 to the calcium release channel of skeletal muscle sarcoplasmic reticulum. J Biol Chem. 1993 Nov 5;268(31):22992-9. PubMed PMID: 7693682.

Timerman AP, Onoue H, Xin HB, Barg S, Copello J, Wiederrecht G, Fleischer S. Selective binding of FKBP12.6 by the cardiac ryanodine receptor. J Biol Chem. 1996 Aug 23;271(34):20385-91. PubMed PMID: 8702774.

Tokunaga M, Imamoto N, Sakata-Sogawa K. Highly inclined thin illumination enables clear single-molecule imaging in cells. Nat Methods. 2008 Feb;5(2):159-61. doi: 10.1038/nmeth1171. Epub 2008 Jan 6. Erratum in: Nat Methods. 2008 May;5(5):455. PubMed PMID: 18176568.

Tokuyasu KT. Immunochemistry on ultrathin frozen sections. Histochem J. 1980 Jul;12(4):381-403. PubMed PMID: 7440248.

Torres NS, Sachse FB, Izu LT, Goldhaber JI, Spitzer KW, Bridge JH. A modified local control model for Ca2+ transients in cardiomyocytes: junctional flux is accompanied by release from adjacent non-junctional RyRs. J Mol Cell Cardiol. 2014 Mar;68:1-11. doi: 10.1016/j.yjmcc.2013.12.019. Epub 2014 Jan 3. PubMed PMID: 24389341; PubMed Central PMCID: PMC3942534.

Tseng GN, Boyden PA. Multiple types of Ca2+ currents in single canine Purkinje cells. Circ Res. 1989 Dec;65(6):1735-50. PubMed PMID: 2555080.

Valdivia HH, Kaplan JH, Ellis-Davies GC, Lederer WJ. Rapid adaptation of cardiac ryanodine receptors: modulation by Mg2+ and phosphorylation. Science. 1995 Mar 31;267(5206):1997-2000. PubMed PMID: 7701323; PubMed Central PMCID: PMC4242209.

Van de Linde S, Krstić I, Prisner T, Doose S, Heilemann M, Sauer M. Photoinduced formation of reversible dye radicals and their impact on super-resolution imaging. Photochem Photobiol Sci. 2011 Apr;10(4):499-506. doi: 10.1039/c0pp00317d. Epub 2010 Dec 10. Erratum in: Photochem Photobiol Sci. 2012 Dec;11(12):1952. PubMed PMID: 21152594.

Van de Linde S, Loschberger A, Klein T, Heidbreder M, Wolter S, Heilemann M, et al. Direct stochastic optical reconstruction microscopy with standard fluorescent probes. Nat Protoc. 2011;6:991-1009.

Van Oort RJ, Garbino A, Wang W, Dixit SS, Landstrom AP, Gaur N, De Almeida AC, Skapura DG, Rudy Y, Burns AR, Ackerman MJ, Wehrens XH. Disrupted junctional membrane complexes and hyperactive ryanodine receptors after acute

junctophilin knockdown in mice. Circulation. 2011 Mar 8;123(9):979-88. doi: 10.1161/CIRCULATIONAHA.110.006437. Epub 2011 Feb 21. PubMed PMID: 21339484; PubMed Central PMCID: PMC3056402.

Volkmann N. Methods for segmentation and interpretation of electron tomographic reconstructions. Methods Enzymol. 2010;483:31-46. doi: 10.1016/S0076-6879(10)83002-2. Review. PubMed PMID: 20888468.

Wagenknecht T, Grassucci R, Frank J, Saito A, Inui M, Fleischer S. Three-dimensional architecture of the calcium channel/foot structure of sarcoplasmic reticulum. Nature. 1989 Mar 9;338(6211):167-70. PubMed PMID: 2537473.

Wagenknecht T, Radermacher M, Grassucci R, Berkowitz J, Xin HB, Fleischer S. Locations of calmodulin and FK506-binding protein on the three-dimensional architecture of the skeletal muscle ryanodine receptor. J Biol Chem. 1997 Dec 19;272(51):32463-71. PubMed PMID: 9405457.

Wagner E, Lauterbach MA, Kohl T, Westphal V, Williams GS, Steinbrecher JH, Streich JH, Korff B, Tuan HT, Hagen B, Luther S, Hasenfuss G, Parlitz U, Jafri MS, Hell SW, Lederer WJ, Lehnart SE. Stimulated emission depletion live-cell super-resolution imaging shows proliferative remodeling of T-tubule membrane structures after myocardial infarction. Circ Res. 2012 Aug 3;111(4):402-14. doi: 10.1161/CIRCRESAHA.112.274530. Epub 2012 Jun 21. PubMed PMID: 22723297; PubMed Central PMCID: PMC4219578.

Walker SM, Schrodt GR, Edge MB. The density attached to the inside surface of the apposed sarcoplasmic reticular membrane in vertebrate cardiac and skeletal muscle fibres. J Anat. 1971;108:217-30.

Wang SQ, Song LS, Lakatta EG, Cheng H. Ca2+ signalling between single L-type Ca2+ channels and ryanodine receptors in heart cells. Nature. 2001;410:592-6.

Wang SQ, Stern MD, Rios E, Cheng H. The quantal nature of Ca2+ sparks and in situ operation of the ryanodine receptor array in cardiac cells. Proceedings of the National Academy of Sciences of the United States of America. 2004;101:3979-84.

Wang YG, Dedkova EN, Ji X, Blatter LA, Lipsius SL. Phenylephrine acts via IP3-dependent intracellular NO release to stimulate L-type Ca2+ current in cat atrial myocytes. J Physiol. 2005 Aug 15;567(Pt 1):143-57. Epub 2005 Jun 9. PubMed PMID: 15946966; PubMed Central PMCID: PMC1474159.

Warrier S, Ramamurthy G, Eckert RL, Nikolaev VO, Lohse MJ, Harvey RD. cAMP microdomains and L-type Ca2+ channel regulation in guinea-pig ventricular myocytes. J Physiol. 2007 May 1;580(Pt.3):765-76. Epub 2007 Feb 8. PubMed PMID: 17289786; PubMed Central PMCID: PMC2075464.

Wei S, Guo A, Chen B, Kutschke W, Xie YP, Zimmerman K, Weiss RM, Anderson ME, Cheng H, Song LS. T-tubule remodeling during transition from hypertrophy to heart failure. Circ Res. 2010 Aug 20;107(4):520-31. doi: 10.1161/CIRCRESAHA.109.212324. Epub 2010 Jun 24. PubMed PMID: 20576937; PubMed Central PMCID: PMC2927862.

Willig KI, Harke B, Medda R, Hell SW. STED microscopy with continuous wave beams. Nat Methods. 2007 Nov;4(11):915-8. Epub 2007 Oct 21. PubMed PMID: 17952088.

Witcher DR, Kovacs RJ, Schulman H, Cefali DC, Jones LR. Unique phosphorylation site on the cardiac ryanodine receptor regulates calcium channel activity. J Biol Chem. 1991 Jun 15;266(17):11144-52. PubMed PMID: 1645727.

Wolter S, Endesfelder U, van de Linde S, Heilemann M, Sauer M. Measuring localization performance of super-resolution algorithms on very active samples. Opt Express. 2011 Apr 11;19(8):7020-33. doi: 10.1364/OE.19.007020. PubMed PMID: 21503016.

Wolter S, Löschberger A, Holm T, Aufmkolk S, Dabauvalle MC, van de Linde S, Sauer M. rapidSTORM: accurate, fast open-source software for localization microscopy. Nat Methods. 2012 Nov;9(11):1040-1. doi: 10.1038/nmeth.2224. PubMed PMID: 23132113.

Wolter S, Schüttpelz M, Tscherepanow M, VAN DE Linde S, Heilemann M, Sauer M. Real-time computation of subdiffraction-resolution fluorescence images. J Microsc. 2010 Jan;237(1):12-22. doi: 10.1111/j.1365-2818.2009.03287.x. PubMed PMID: 20055915.

Wombacher R, Heidbreder M, van de Linde S, Sheetz MP, Heilemann M, Cornish VW, Sauer M. Live-cell super-resolution imaging with trimethoprim conjugates. Nat Methods. 2010 Sep;7(9):717-9. doi: 10.1038/nmeth.1489. Epub 2010 Aug 8. PubMed PMID: 20693998.

Wong J, Baddeley D, Bushong EA, Yu Z, Ellisman MH, Hoshijima M, Soeller C. Nanoscale distribution of ryanodine receptors and caveolin-3 in mouse ventricular myocytes: dilation of t-tubules near junctions. Biophys J. 2013 Jun 4;104(11):L22-4. doi: 10.1016/j.bpj.2013.02.059. PubMed PMID: 23746531; PubMed Central PMCID: PMC3672889.

Wu CY, Chen B, Jiang YP, Jia Z, Martin DW, Liu S, Entcheva E, Song LS, Lin RZ. Calpain-dependent cleavage of junctophilin-2 and T-tubule remodeling in a mouse model of reversible heart failure. J Am Heart Assoc. 2014 Jun 23;3(3):e000527. doi: 10.1161/JAHA.113.000527. PubMed PMID: 24958777; PubMed Central PMCID: PMC4309042.

Wu HD, Xu M, Li RC, Guo L, Lai YS, Xu SM, Li SF, Lü QL, Li LL, Zhang HB, Zhang YY, Zhang CM, Wang SQ. Ultrastructural remodelling of Ca(2+) signalling apparatus in failing heart cells. Cardiovasc Res. 2012 Sep 1;95(4):430-8. doi:

10.1093/cvr/cvs195. Epub 2012 Jun 15. PubMed PMID: 22707157; PubMed Central PMCID: PMC3422078.

Xiao B, Jiang MT, Zhao M, Yang D, Sutherland C, Lai FA, Walsh MP, Warltier DC, Cheng H, Chen SR. Characterization of a novel PKA phosphorylation site, serine-2030, reveals no PKA hyperphosphorylation of the cardiac ryanodine receptor in canine heart failure. Circ Res. 2005 Apr 29;96(8):847-55. Epub 2005 Mar 24. PubMed PMID: 15790957.

Xiao J, Tian X, Jones PP, Bolstad J, Kong H, Wang R, Zhang L, Duff HJ, Gillis AM, Fleischer S, Kotlikoff M, Copello JA, Chen SR. Removal of FKBP12.6 does not alter the conductance and activation of the cardiac ryanodine receptor or the susceptibility to stress-induced ventricular arrhythmias. J Biol Chem. 2007 Nov 30;282(48):34828-38. Epub 2007 Oct 5. PubMed PMID: 17921453; PubMed Central PMCID: PMC2760432.

Xiao RP, Valdivia HH, Bogdanov K, Valdivia C, Lakatta EG, Cheng H. The immunophilin FK506-binding protein modulates Ca2+ release channel closure in rat heart. J Physiol. 1997 Apr 15;500 (Pt 2):343-54. PubMed PMID: 9147322; PubMed Central PMCID: PMC1159388.

Xie W, Brochet DX, Wei S, Wang X, Cheng H. Deciphering ryanodine receptor array operation in cardiac myocytes. J Gen Physiol. 2010 Aug;136(2):129-33. doi: 10.1085/jgp.201010416. PubMed PMID: 20660655; PubMed Central PMCID: PMC2912071.

Xie YP, Chen B, Sanders P, Guo A, Li Y, Zimmerman K, Wang LC, Weiss RM, Grumbach IM, Anderson ME, Song LS. Sildenafil prevents and reverses transverse-tubule remodeling and Ca(2+) handling dysfunction in right ventricle failure induced by pulmonary artery hypertension. Hypertension. 2012 Feb;59(2):355-62. doi: 10.1161/HYPERTENSIONAHA.111.180968. Epub 2011 Dec 27. PubMed PMID: 22203744; PubMed Central PMCID: PMC3266850.

Xu L, Eu JP, Meissner G, Stamler JS. Activation of the cardiac calcium release channel (ryanodine receptor) by poly-S-nitrosylation. Science. 1998 Jan 9;279(5348):234-7. PubMed PMID: 9422697.

Xu M, Wu HD, Li RC, Zhang HB, Wang M, Tao J, Feng XH, Guo YB, Li SF, Lai ST, Zhou P, Li LL, Yang HQ, Luo GZ, Bai Y, Xi JJ, Gao W, Han QD, Zhang YY, Wang XJ, Meng X, Wang SQ. Mir-24 regulates junctophilin-2 expression in cardiomyocytes. Circ Res. 2012 Sep 14;111(7):837-41. doi: 10.1161/CIRCRESAHA.112.277418. Epub 2012 Aug 13. PubMed PMID: 22891046; PubMed Central PMCID: PMC3611051.

Xu M, Zhou P, Xu SM, Liu Y, Feng X, Bai SH, Bai Y, Hao XM, Han Q, Zhang Y, Wang SQ. Intermolecular failure of L-type Ca2+ channel and ryanodine receptor signaling in hypertrophy. PLoS Biol. 2007 Feb;5(2):e21. PubMed PMID: 17214508; PubMed Central PMCID: PMC1764437.

Yan J, Walker CG, O'sullivan ML, Bushong EA, Ellisman MH, Hoshijima M, et al. Visualization, Modeling, and Spatial Statistics of Mitochondrial Assembly in Adult Cardiomyocytes using Serial Block-Face Scanning Electron Microscopy

Yin CC, D'Cruz LG, Lai FA. Ryanodine receptor arrays: not just a pretty pattern? Trends Cell Biol. 2008;18:149-56.

Yin CC, Lai FA. Intrinsic lattice formation by the ryanodine receptor calcium-release channel. Nat Cell Biol. 2000 Sep;2(9):669-71. PubMed PMID: 10980710.

Young, R.J., Dingle, T., Robinson, K. & Pugh, P.J.A. (1993) An application of scanned focused ion beam milling to studies on the internal morphology of small arthropods. *J. Microsc.* **172**, 81–88.

Yu Z, Holst MJ, Hayashi T, Bajaj CL, Ellisman MH, McCammon JA, et al. Three-dimensional geometric modeling of membrane-bound organelles in ventricular myocytes: bridging the gap between microscopic imaging and mathematical simulation. Journal of structural biology. 2008;164:304-13.

Yu Z, Wang J, Gao Z, Xu M, Hoshijima M. New software developments for quality mesh generation and optimization from biomedical imaging data. Comput Methods Programs Biomed. 2014;113(1):226-40. doi: 10.1016/j.cmpb.2013.08.009. Epub 2013 Sep 4. PubMed PMID: 24252469; PubMed Central PMCID: PMC3836056.

Zalk R, Clarke OB, des Georges A, Grassucci RA, Reiken S, Mancia F, Hendrickson WA, Frank J, Marks AR. Structure of a mammalian ryanodine receptor. Nature. 2015 Jan 1;517(7532):44-9. doi: 10.1038/nature13950. Epub 2014 Dec 1. PubMed PMID: 25470061; PubMed Central PMCID: PMC4300236.

Zeuschner D, Geerts WJ, van Donselaar E, Humbel BM, Slot JW, Koster AJ, et al. Immuno-electron tomography of ER exit sites reveals the existence of free COPII-coated transport carriers. Nature cell biology. 2006;8:377-83.

Zhang C, Chen B, Guo A, Zhu Y, Miller JD, Gao S, Yuan C, Kutschke W, Zimmerman K, Weiss RM, Wehrens XH, Hong J, Johnson FL, Santana LF, Anderson ME, Song LS. Microtubule-mediated defects in junctophilin-2 trafficking contribute to myocyte transverse-tubule remodeling and Ca2+ handling dysfunction in heart failure. Circulation. 2014 Apr 29;129(17):1742-50. doi: 10.1161/CIRCULATIONAHA.113.008452. Epub 2014 Feb 11. PubMed PMID: 24519927; PubMed Central PMCID: PMC4006305.

Zhang HB, Li RC, Xu M, Xu SM, Lai YS, Wu HD, Xie XJ, Gao W, Ye H, Zhang YY, Meng X, Wang SQ. Ultrastructural uncoupling between T-tubules and sarcoplasmic reticulum in human heart failure. Cardiovasc Res. 2013 May 1;98(2):269-76. doi: 10.1093/cvr/cvt030. Epub 2013 Feb 11. PubMed PMID: 23405000.

Zipfel WR, Williams RM, Webb WW. Nonlinear magic: multiphoton microscopy in the biosciences. Nat Biotechnol. 2003 Nov;21(11):1369-77. Review. PubMed PMID: 14595365.

Zorzato F, Fujii J, Otsu K, Phillips M, Green NM, Lai FA, Meissner G, MacLennan DH. Molecular cloning of cDNA encoding human and rabbit forms of the Ca2+ release channel (ryanodine receptor) of skeletal muscle sarcoplasmic reticulum. J Biol Chem. 1990 Feb 5;265(4):2244-56. PubMed PMID: 2298749.